UNIVERSIDADE ESTADUAL PAULISTA "JÚLIO DE MESQUITA FILHO"
FACULDADE DE ENGENHARIA
CAMPUS DE ILHA SOLTEIRA

RENAN SANCHES GERONEL

DYNAMIC AND VIBRATION ANALYSIS OF A QUADROTOR
TYPE UAV WITH A PAYLOAD:
INSIGHTS FOR AERIAL MEDICAL PRODUCT TRANSPORTATION

ILHA SOLTEIRA
2023

RENAN SANCHES GERONEL

DYNAMIC AND VIBRATION ANALYSIS OF A QUADROTOR TYPE UAV WITH A PAYLOAD:
INSIGHTS FOR AERIAL MEDICAL PRODUCT TRANSPORTATION

A Thesis submitted to the Faculdade de Engenharia de Ilha Solteira - UNESP in partial fulfillment of the requirements for obtaining the Doctorate degree in Mechanical Engineering.
Knowledge area: Solid Mechanics

Advisor: Prof. Dr. Douglas Domingues Bueno
Co-Advisor: Profa. Dra. Ruxandra Mihaela Botez

ILHA SOLTEIRA

2023

FICHA CATALOGRÁFICA

Desenvolvido pelo Serviço Técnico de Biblioteca e Documentação

UNIVERSIDADE ESTADUAL PAULISTA

Câmpus de Ilha Solteira

CERTIFICADO DE APROVAÇÃO

TÍTULO DA TESE: Dynamic and Vibration analysis of a quadrotor type UAV with a payload: insights for aerial medical product transportation

AUTOR: RENAN SANCHES GERONEL
ORIENTADOR: DOUGLAS DOMINGUES BUENO
COORIENTADORA: RUXANDRA MIHAELA BOTEZ

Aprovado como parte das exigências para obtenção do Título de Doutor em Engenharia Mecânica, área: Mecânica dos Sólidos pela Comissão Examinadora:

Prof. Dr. DOUGLAS DOMINGUES BUENO (Participaçao Virtual)
Departamento de Matemática / Faculdade de Engenharia de Ilha Solteira

Prof. Dr. MARCIO ANTONIO BAZANI (Participaçao Virtual)
Departamento de Engenharia Mecânica / Unesp - Ilha Solteira

Prof. Dr. ALEXANDRE SANTOS BRANDÃO (Participaçao Virtual)
Departamento de Engenharia elétrica / Universidade Federal de Viçosa

Prof. Dr. TOBIAS SOUZA MORAIS (Participaçao Virtual)
Departamento de Engenharia Mecânica / Universidade Federal de Uberlâ

Profa. Dra. MAÍRA MARTINS DA SILVA (Participaçao Virtual)
Departamento de Engenharia Mecânica / Universidade de São Paulo

Ilha Solteira, 13 de fevereiro de 2023

To my parents.

Acknowledgments

First, I would like to thank God for everything He has done in my life.

To my mother Clarice and to my father Jair, that always encouraged me to keep studying and researching. To my sister Maiby, for all the support during the doctorate.

To Prof. Dr. Douglas D. Bueno, for more than three years of guidance and friendship. Douglas always gave more than the necessary attention and he was a great visionary regarding this work. I would like to thanks Douglas for being not only an excellent supervisor, but also a remarkable person. Thank you very much Douglas.

I would like to thanks to Dr. Ruxandra Mihaela Botez for receiving me at the Active Control, Avionics and Aeroservoelasticity Research Laboratory (LARCASE) in Montreal/Canada during my internship. I will always be grateful for this incredible experience. A special thanks to all LARCASE members, especially to my friends Hossein Negahban, Nicola Zonzini, Simon L-Martel, Musavir Bashir and Seyed Hashemi.

To my friends João Trentin, João Angelo Brogin, Frederico Ribeiro, Marcus Omori, Lais Visnadi, Lucas Garpelli, Kayc Lopes, Larissa Drews, Andreyson Jambersi, Rafael Mattei, Lucas Chaim and Jessé Paixão who were able to help me in the moments that I needed the most, thank you! To all professors and UNESP employees.

"Don't let the noise of others' opinions drown out your own inner voice."

Steve Jobs

Abstract

Unmanned Aerial Vehicles (UAVs) have gained rapid attention as a potential solution to overcome geographical and logistic challenges in different areas. In particular for medical and hospital products transportation, UAVs are used to assist health care services in the delivery of medical goods, including organs, vaccines and blood samples. However, some of these products are sensitive to vibration, which can decrease the therapeutic efficacy of the transported payload. Then, this thesis investigates the vibration characteristics of a payload carried by a quadrotor. A commercial UAV is used to evaluate the effect of the payload dynamics on the flight, by considering different attachment configurations. The results have shown an amplification of the quadrotor acceleration, highlighting the importance of controlling these vibrating effects. Regarding the dynamic models, a vertical vibrating payload is initially investigated, by assessing two different control strategies (quasi-open and closed loops). The combination of elastic attachment and suspended payload have been assessed. The Adaptive Sliding Mode Control have been designed to compensate the payload effects on the UAV dynamics. Therefore, oscillations caused by an attached mass, external disturbances and different dynamic configurations have become and important topic in UAV medical transportation. Low payload oscillations may guarantee a rapid spread and use of commercial UAVs for medical products delivery, with a high transportation reliability.

Keywords: Unmanned Aerial Vehicle. Medical and Hospital products Transportation. Payload vibration. Adaptive Sliding Mode Control

Resumo

Veículos Aéreos não Tripulados (VANTs) tem ganhado rápida atenção como uma solução promissora para superar desafios logísticos e geográficos em diferentes aplicações. Em particular, para o transporte de produtos da área médica e hospitalar, VANTs são utilizados para auxiliar os serviços de saúde na entrega de produtos médicos, incluindo órgãos, vacinas e amostras de sangue. Entretanto, alguns desses produtos são sensíveis a vibração ou mudanças de temperatura, o que pode acarretar na diminuição no efeito terapêutico da carga transportada. Com isso, esta tese investiga as características de vibração de uma carga sendo transportada por um VANT. Um VANT comercial é usado para investigar o impacto da dinâmica da carga útil, usando diferentes configurações de anexos. Os resultados mostraram uma amplificação da aceleração do quadcóptero, destacando a importância de controlar esses efeitos. Com relação aos modelos dinâmicos, uma carga com vibração vertical é inicialmente investigada, pela utilização de duas abordagens de controles diferentes (circuitos quase-aberto e fechado). A combinação de fixação elástica e carga útil suspensa foi avaliada. O controle de modo deslizante adaptativo foi projetado para compensar os efeitos da carga útil na dinâmica do VANT. Portanto, oscilações causadas pela carga acoplada, distúrbios externos e diferentes configurações dinâmicas tem se tornado um importante tópico no transporte de produtos médicos por VANTs. Baixas oscilações de carga útil podem garantir uma rápida disseminação e uso desses veículos aéreos comerciais para entrega de produtos médicos, com alta confiabilidade de transporte.

Palavras-chave: Veículos Aéreos não Tripulados. Transporte de produtos médicos e hospitalares. Vibração da carga. Controle de Modo Deslizante Adaptativo.

List of Figures

List of Tables

List of Acronyms

UAV   -   Unmanned Aerial Vehicle

RPVs   -   Remotely Piloted Vehicles

GPS   -   Global Position System

DOF   -   Degrees of Freedom

MEMS   -   Micro-Electromechanical Systems

PD   -   Proportional Derivative

PID   -   Proportional Integral Derivative

SMC   -   Sliding Mode Control

CoG   -   Center of Gravity

ASCM   -   Adaptive Sliding Mode Control

LQR   -   Linear-Quadratic Regulator

LD   -   Lactate Dehydrogenase

TRL   -   Technology Readiness Level

UGV   -   Unmanned Ground Vehicles

PSD   -   Power Spectral Density

FFT   -   Fast Fourier Transform

IAE   -   Integral of the Absolute magnitude of the Error

ITAE   -   Integral of Time multiplied by the Absolute Error

RMS   -   Root Mean Square

List of Symbols

X_B, Y_B, Z_B	-	Body-fixed reference system
X_I, Y_I, Z_I	-	Inertial reference system
v_x, v_y, v_z	-	linear velocities along x, y and z
$\omega_x, \omega_y, \omega_z$	-	angular velocities along x, y and z
x, y, z	-	linear position of the quadrotor
F_i	-	thrust forces of four propellers ($i = 1, 2, 3, 4$)
M_i	-	torques generated by four propellers
$\mathbf{M}_{q_B}$	-	matrix of inertia for the 6 DOF model (body-fixed frame)
$\mathbf{C}_{q_B}(\nu_{q_B})$	-	matrix of Coriolis for the 6 DOF model (body-fixed frame)
$\mathbf{g}_{q_B}$	-	vector of gravity effect for 6 DOF (body-fixed frame)
$\mathbf{M}_{q_I}$	-	matrix of inertia for the 6 DOF model (inertial frame)
$\mathbf{C}_{q_I}(\nu_{q_B})$	-	matrix of Coriolis for the 6 DOF model (inertial frame)
$\mathbf{g}_{q_I}$	-	vector of gravity effect for the 6 DOF model (inertial frame)
$\mathbf{I}_{n \times n}$	-	identity matrix with n rows and n columns
$\mathbf{J}_q$	-	transformation matrix
$\dot{\mathbf{J}}_q$	-	transformation matrix derivative with respect to time
m	-	mass of the quadrotor
I_x, I_y, I_z	-	moment of inertia of quadrotor along x, y and z
U_i	-	control input components
m_p	-	mass of the payload
k_p	-	attachment stiffness in the vertical direction
F_k	-	elastic force between the quadrotor and its payload
z_p	-	vertical direction of the payload
$\mathbf{M}_{qp}$	-	matrix of inertia for the 7 DOF model (body-fixed frame)
$\mathbf{C}_{qp}$	-	Coriolis matrix for the 7 DOF model (body-fixed frame)
$\mathbf{g}_{qp}$	-	gravitational vector for the 7 DOF model (body-fixed frame)
$\mathbf{M}_{qp_I}$	-	matrix of inertia for the 7 DOF model (inertial frame)
$\mathbf{C}_{qp_I}$	-	Coriolis matrix for the 7 DOF model (inertial frame)

$\mathbf{g}_{qp_I}$	-	gravitational vector for the 7 DOF model (inertial frame)
$\mathbf{K}_{qp_I}$	-	stiffness matrix for the 7 DOF model (inertial frame)
$\mathbf{F}_d$	-	gust vector
$\mathbf{J}_{qp}$	-	transformation matrix
$\dot{\mathbf{J}}_{qp}$	-	transformation matrix derivative with respect to time
I_x^p, I_y^p, I_z^p	-	moment of inertia of the payload along x, y and z
$\mathbf{0}_{n \times n}$	-	zero matrix with n rows and n columns
$\mathbf{u}_{qp}(t)$	-	input vector, represented in state-space form
$\mathbf{X}_{gp}$	-	gravitational vector, represented in state-space vector
$\mathbf{A}_{qp}$	-	dynamic matrix, represented in state-space vector
$\mathbf{u}_{qp}$	-	input matrix, represented in state-space vector
l	-	length between the rotor and the quadrotor center of gravity
λ	-	relation between torque and generated force
f_c	-	oscillation frequency of the payload mass
f_r	-	natural frequency of mass-spring
F	-	ratio between f and f_r
c_a, c_l	-	angular and linear coefficients of the frequency line
p_m	-	relation between payload and quadrotor masses
p_x, p_y, p_z	-	ratio between quadrotor and its payload's moment of inertia
r_x, r_y, r_z	-	radii of gyration
$x_{des}, y_{des}, z_{des}$	-	desired altitude and position of the quadrotor
$\dot{x}_{des}, \dot{y}_{des}, \dot{z}_{des}$	-	desired altitude and position derivatives with respect to time
$\ddot{x}_{des}, \ddot{y}_{des}, \ddot{z}_{des}$	-	second derivatives with respect to time
H	-	reference height of flight
p_n	-	dimensionless parameter
$\tilde{m}$	-	sum of the masses of quadrotor and its payload
U_x, U_y	-	virtual inputs of the controller
s_k	-	sliding surface
$\dot{s}_k$	-	time derivative of sliding surface
ΔI_k	-	parameters related to uncertainties of the payload dynamics
k_{pgk}, k_{dgk}	-	controller gains of the PD
L_j	-	turbulence scale length
w_{ws}	-	wind speed

$G_z(s)$	-	transfer function of shaping filter
V	-	velocity of the wind
s	-	Laplace variable
v_{ws}	-	velocity of the wind with respect to time
t	-	time
C_{dz}	-	drag coefficient
A_z	-	area projected by the UAV
$\boldsymbol{\tau}_I$	-	control input for the 11 DOF model (inertial reference)
P_i	-	phases of the proposed flight
F_{sj}	-	constraint forces between the quadrotor and its payload
l_b	-	physical distance between the quadrotor and its payload
$\mathbf{M}_I$	-	matrix of inertia for the 11 DOF model (inertial frame)
$\mathbf{C}_I$	-	Coriolis matrix for the 11 DOF model (inertial frame)
$\mathbf{K}_I$	-	stiffness matrix for the 11 DOF model (inertial frame)
x_p, y_p, z_p	-	linear position of the payload
ϕ_p, θ_p	-	angular position of the payload
r_{qp}	-	distance vector between the quadrotor and its payload
$\mathbf{M}_B$	-	matrix of inertia for the 11 DOF model (inertial frame)
$\mathbf{C}_B$	-	Coriolis matrix for the 11 DOF model (inertial frame)
$\mathbf{g}_B$	-	gravitational vector for the 11 DOF model (inertial frame)
$\mathbf{K}_B$	-	stiffness matrix for the 11 DOF model (inertial frame)
k_{px}, k_{py}, k_{pz}	-	stiffness proportional terms
V_k	-	Lyapunov candidate function
$\dot{V}_k$	-	derivative of Lyapunov candidate function

Greek Letters

$\boldsymbol{\nu}_{q_B}$	-	velocity vector for the 6 DOF model (body-fixed frame)
$\boldsymbol{\tau}_{q_B}$	-	control input vector for the 6 DOF model (body-fixed frame)
$\boldsymbol{\tau}_{q_I}$	-	control input vector for the 6 DOF model (inertial frame)
$\boldsymbol{\eta}_{q_I}$	-	generalized coordinate vector for the 6 DOF model (inertial frame)
$\boldsymbol{\tau}_{qp}$	-	control input vector for the 7 DOF model (body-fixed frame)
$\boldsymbol{\tau}_{qp_I}$	-	control input vector for the 7 DOF model (inertial frame)
$\boldsymbol{\eta}_{qp_I}$	-	generalized coordinate vector for 7 DOF (inertial frame)
$\boldsymbol{x}_{qp}$	-	state vector, represented in state-space form
ϕ, θ, ψ	-	roll, pitch and yaw angles of the quadrotor
$\dot{\phi}, \dot{\theta}, \dot{\psi}$	-	roll, pitch and yaw angles derivative with respect to time
τ_t	-	non-dimensional time
$\phi_{des}, \theta_{des}, \psi_{des}$	-	desired altitude angles
$\epsilon_k, \eta_k, \lambda_k$	-	gains of the SMC
$\Phi_j(\Omega)$	-	power spectral density
σ_j	-	turbulence intensity
η_{gj}	-	white Gaussian noise function
ρ	-	air density
$\boldsymbol{\eta}_I$	-	generalized coordinate vector for the 11 DOF model (inertial frame)
$\boldsymbol{\eta}_B$	-	generalized coordinate vector for the 11 DOF model (body-fixed frame)
$\hat{\alpha}_p$	-	positive coefficient for adaptive altitude control
$\hat{\beta}_\phi, \hat{\beta}_\theta, \hat{\beta}_\psi$	-	positive coefficients for adaptive attitude control

Contents

1 INTRODUCTION

This first chapter presents a brief motivation, the objectives, the main contributions, and the outline of this thesis. The state-of-art focused on medical product transportation is presented in Chapter 3.

1.1 MOTIVATION

Unmanned Aerial Vehicles (UAVs) are autonomous vehicles guided remotely, and they have the ability to carry a variety of payloads. Depending on the world region, several names have been used to describe this type of aircraft such as UAVs, UASs (Unmanned Aerial Systems), RPVs (Remotely Piloted Vehicles), including their popular name "drones" (VALAVANIS; VACHTSEVANOS, 2014). Search and rescue, medical product delivery (HII; COURTNEY; ROYALL, 2019; MALIK; ROY, 2011), mapping (PHAN; LIU, 2010), agricultural (KIM *et al.*, 2019; JU; SON, 2018) and surveillance (PURI, 2005) operations are promising examples in applications of aerial vehicles employed in the first years. The use of UAVs can increase operations efficiency by reducing the delivery time, need for personnel and costs, and their delivery systems can be selected according to their types, functionalities, operational characteristics, and mission objectives.

Most of the recent applications involving UAVs employees different attached devices, such as transducers, electronic equipments or components to carry different types of payload, such as medical goods, foods and others. In agriculture, for example cameras and sensors are used to measure the level of vegetation transpiration, hydric stress, and distribution over an area (DUFEK *et al.*, 2019). UAVs are also used for transporting cargoes like pesticides (MOGILI; DEEPAK, 2018) and to oil spill cleanup missions in the marine environment (KAVIRI; TAHSIRI; TAGHIRAD, 2021). In the medical field, UAVs have been employed mainly because the delivery time is crucial to organs and pharmaceutical goods (SCALEA *et al.*, 2019). However, these type of payload can be affected by the vibrating behavior generated by different attachment systems (GERONEL;

BUENO, 2021). In addition, the undesired vibration can reduce the UAVs performance, as well as its payload integrity and onboard electronic devices.

UAVs are recently considered to develop new health care services, including the transportation of medical goods, organs, and in the delivery of blood stocks and pharmacies to clinics and hospitals. However, there is a limited number of works investigating the behavior of the resulting dynamics involved in these applications. Scalea *et al.* (2019) have shown the payload response when a smart cooler is attached directly to a UAV's body. Wireless biosensors and barometric pressure, altitude, vibration and GPS sensors are placed alongside the organ (in the attached compartment) to measure its characteristics along the desired trajectory. Experimental tests are conducted to verify the feasibility of quadrotor transportation despite the potential damage to the organs tissues which can occur if they are subjected to vibrations. Oakey *et al.* (2021b) have compared the effects of vibrations caused by UAVs with traditional road transportation. Insulin is used, since its sensitivity to vibration can lead to the degradation and loss of its efficacy. Experimental tests have shown that the overall vibration levels caused by UAV flights are significantly higher than those caused by road transportation. However, the authors do not evaluate the dynamic characteristics of the attachment system exmployed to perform the flights.

The geometry, payload capacity, number of rotors, flight velocity are examples of parameters to take into account when defining a UAV-based transportation missions. On the other hand, the physical connection between the UAV and its payload is an interesting research topic to evaluate the resulting vibration behavior. Generally, authors have just considered a rigid link to investigate the dynamics of the attached payload (KLAUSEN; FOSSEN; JOHANSEN, 2015; KLAUSEN; FOSSEN; JOHANSEN, 2017). In this context, the present thesis introduce the modeling of different flexible attachment system configurations to assess the vibrating behavior of a quadrotor with a payload. A dynamic modeling of a 7 DOF quadrotor using elastic attachment is considered, restricted in the vertical direction. Then, the characteristics of a quadrotor with 11 degrees of freedom is now designed, including three linear and two angular motions of the payload. Different controller strategies, including Proportional Derivative, Sliding Mode Control and Adaptive Sliding Model Control are also used to attenuate the vibration between the quadrotor and its payload.

1.2 OBJECTIVES

The main objective of this work is to investigate the vibrating behavior of flexible attachment between the UAV and its payload. The specific objectives are summarized below:

- To investigate two dynamic models of a quadrotor with an attached payload, considering a quasi-open-loop and closed loop controls. The vibration characteristics are investigated considering a vertical translating payload and a combination of swing and elastic movements of a payload;

- To evaluate the performance of a designed Adaptive Sliding Mode Control (ASMC) to guide the UAV in a pre-defined trajectory and to reduce the vibration level during the flight. Adaptive coefficients are estimated according to the payload mass and desired trajectory;

- To provide insights on the use of UAVs in the medical field, including their vibration dynamics. Different implications of their use in medical tasks are also assessed, including their legislation, sensitivity to vibration and future opportunities.

1.3 MAIN CONTRIBUTIONS

The main contributions of this doctorate to the literature are:

- A comprehensive literature review exploring the use of UAVs and the vibration characteristics in the medical and hospital products transportation.

- An approach estimate the vibratory frequency of payload during the flight, considering a quasi-open-loop control.

- A 7 DOF dynamic model for a quadrotor with a payload, considering a flexible attachment to assess the vertical vibration in cruise flight. Performance Indices are employed to evaluate the relative trajectory oscillations in different phases of the flight.

- A 11 DOF dynamic model for a quadrotor with a suspended payload and the evaluation of Adaptive Sliding Mode Control performance to keep the aerial vehicle in a desired trajectory and to reduce the vibration during the flight.

Some of the results were published in the following journal articles:

- Geronel, Dowell and Bueno (2021): "Estimating the oscillation frequency of a payload mass on quadcopter in non-autonomous flight", **JVC/ Journal of Vibration and Control**, v. 29, p. 236-250, 2023.

- Geronel, Botez and Bueno (2022b): "On the Effect of Flexibility on the Dynamics of a Suspended Payload Carried by a Quadrotor", **Designs**, v. 6, p. 31, 2022.

- Geronel, Botez and Bueno (2022a) "Dynamic responses due to the Dryden gust of an autonomous quadrotor UAV carrying a payload", **The Aeronautical Journal**, v. 6, p. 31, 2022.

- Geronel *et al.* (2022) "An overview on the use of unmanned aerial vehicles for medical product transportation: flight dynamics and vibration issues", **Journal of the Brazilian Society of Mechanical Sciences and Engineering**, v. 44, p. 1-18, 2022.

and in the following conferences:

- Terenciani, Geronel and Bueno (2019): "Practical aspects behind the rotors forces to control a quadcopter", In: 25th International Congress of Mechanical Engineering, p. 1-9, 2019.

- Geronel and Bueno (2021): "Trajectory Tracking of a Quadcopter with an Attached Payload Mass under External Disturbances", In: 2021 14th IEEE International Conference on Industry Applications (INDUSCON), São Paulo, p. 1288-1295, 2021.

- Geronel, Botez and Bueno (2021): "Vibration Analysis of the Quadcopter Carrying a Payload", In: 26th International Congress of Mechanical Engineering, p. 1-9, 2021.

- Geronel, Bueno and Botez (2022): "Vibration Analysis of a Payload connected to Quadrotor-type UAV by SMA spring", In: AIAA SCITECH 2022 Forum, January 3-7, 2022, San Diego, CA & Virtual, p. 1-11, 2022.

- Geronel, Botez and Bueno (2022d): "The use of State Feedback control based on LMI to suppress oscillations of payload carried by UAV", In: International Symposium on Unmanned Systems and the Defense Industry 2022, p. 1-5, 2022.

- Geronel, Botez and Bueno (2022c): "The use of Polynomial Trajectory for Vibration Reduction of a Payload carried by a Quadrotor", In: Workshop PPGEM, 2022, Ilha Solteira. Workshop PPGEM 2022, p. 1-5, 2022.

- Geronel, Botez and Bueno (2023): "A vibration suppression for payloads attached to an UAV based on SMA springs", n: AIAA SciTech 2023 Forum, 2023, National Harbor. AIAA SCITECH 2023 Forum, p. 1-14, 2023.

1.4   OUTLINE

This thesis is structured into the following chapters:

- **Chapter 1 - INTRODUCTION**: covers the motivation, objectives, main contributions, and the general content of the thesis.

- **Chapter 2 - EXPERIMENTAL ANALYSIS OF PAYLOAD VIBRATION:** presents the investigation of the general vibration characteristics, in terms of the quadrotor and its payload accelerations.

- **Chapter 3 - A BRIEF STATE-OF-THE-ART REVIEW:** illustrates the main results from the literature to the use of UAVs in the medical field.

- **Chapter 4 - QUADROTOR WITH A VERTICAL VIBRATING PAYLOAD:** exhibits the dynamic model of a 7 DOF dynamic model. Two different control strategies have been studied to evaluate the payload vibration characteristics (quase-open loop and closed loop). Performance Indices are used to investigate the Proportional Derivative and Sliding Mode Control controllers in different phases of the flight.

- **Chapter 5 - FLEXIBILITY ANALYSIS ON THE DYNAMICS OF A SUSPENDED PAYLOAD:** introduces the dynamic model considering a flexible attachment system of a suspended payload using. 6 DOFs are considered to describe the quadrotor motion, and additional 5 DOFs are used to model the payload motion. The use of an Adaptive SMC is investigated to design a single control to guide the quadrotor along the desired trajectory and also to attenuate the vibrations during the flight.

- **Chapter 6 - FINAL REMARKS:** comprises the final conclusions, and the suggestions for future work.

2   EXPERIMENTAL ANALYSIS OF PAYLOAD VIBRATION

This chapter presents an investigation of the vibration characteristics, expressed in acceleration analysis of the quadrotor and its payload. Section 2.1 shows the experimental set-up and Section 2.2 shows that different flight tests have been carried out using a quadrotor with a payload. Different attachment configurations, such as no payload, fixed attachment, swing attachment and fixed with an additional mass are evaluate. In Section 2.3, the results have shown an amplification of the payload vibration in relation to the quadrotor, underscoring the importance of appropriate attachment design for medical material transportation.

2.1   EXPERIMENTAL SET-UP

If a mass is attached to the quadrotor, it is necessary to consider a combination of factors that affect the system. These factors are given by the difference in performance, decrease of battery life, higher drag forces, stronger non-linearities, and even instabilities of the subsystem. Depending on its size and the number of measurement tools and sensibility of a payload (such as some medicines and organs), an appropriate attachment system can be employed for each required transportation.

The payload vibration characteristics are evaluated by considering a commercial quadrotor (DJI Phantom 3 Standard) to perform the desired flights. The Phantom 3 weighs 1.3kg (including its battery), its diagonal length is 0.35m, and it has an internal accelerometer with a resolution of 0.001g. Figure 1 depicts the experimental set-up for a fixed payload configuration. Note, the payload is attached to the landing gear due to the original configuration of the UAV present a fixed camera (i.e., a non-removable device) under its main frame.

Figure 2 shows the schematic illustration of the quadrotor with its payload, highlighting the forces that presented in the attachment system. There are four fixation points,

Figure 1 – Experimental set-up for a fixed payload configuration.

Source: Prepared by the author.

for the attachment system represented on the connection between the quadrotor frame and payload; in each of these points, three elastic forces (F_{kj}, $j = x, y, z$) are represented. These forces are used to describe the flexibility on the attachment system.

Additional information, such as its trajectory and acceleration are provided by UAV's internal sensors of DJI. The payload is a smartphone (an iPhone XR, its weight is 194g and it contains an accelerometer with resolution of 0.01g). The smartphone is attached to the quadrotor frame to illustrate a payload and it is also used as an accelerometer to capture the vibrations in various directions. Figure 3 illustrates the quadrotor and the

Figure 2 – Schematic illustration of a quadrotor with a fixed payload configuration, and the elastic forces on the attachment system.
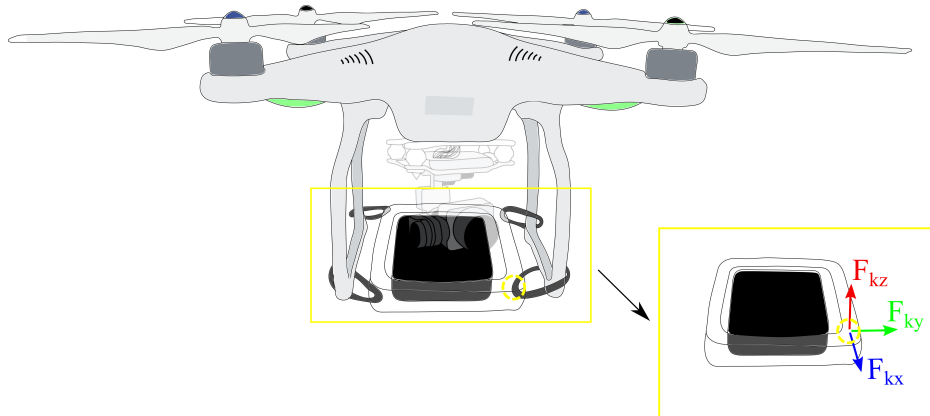
Source: Prepared by the author.

proposed attachment system using four different configurations. The three different axes of acceleration are indicated by small arrows on the payload.

Figure 3 – Schematic illustration of the quadrotor a) with no payload, b) with a fixed payload, c) with a swing payload, and d) with a fixed payload and additional mass.
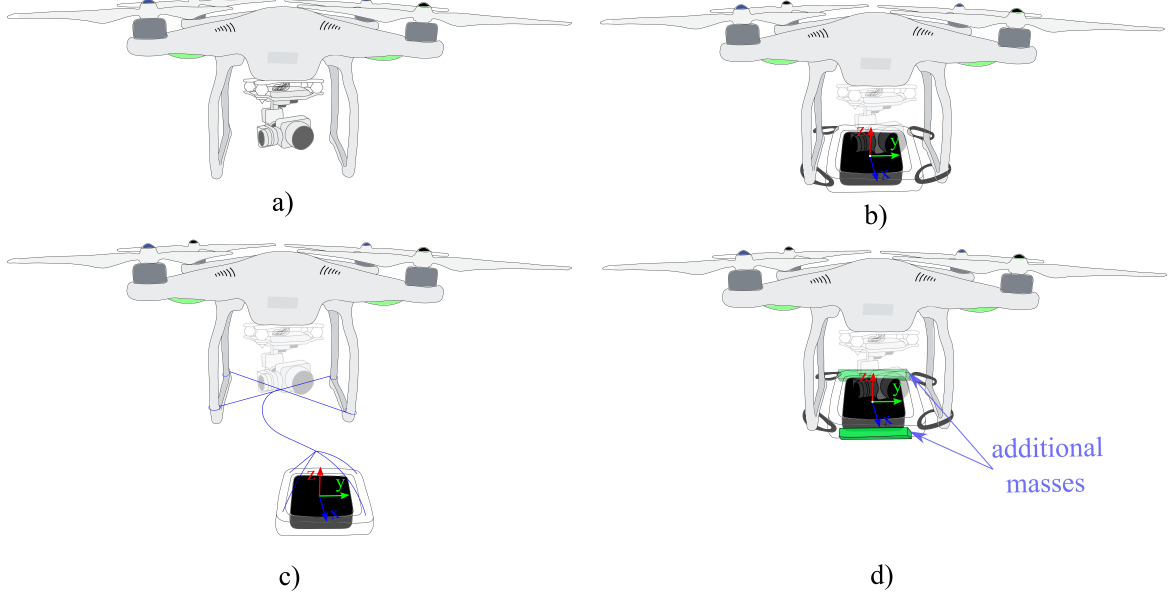
Source: Prepared by the author.

2.2   EXPERIMENTAL TESTS

A series of take-offs, landings, and cruise missions are performed to gather data concerning the vibration effects on both quadrotor and payload during a flight. The path followed by the quadrotor is composed of a take-off $(0 < \tau < 0.2)$, cruise $(0.2 \leq \tau < 0.7)$, and landing $(0.7 \leq \tau \leq 1)$, which are separated by two black dashed lines. The proposed trajectory is illustrated with a gray solid line, where H is the normalized altitude of the quadrotor $(z/H_{max}$, where z is the current altitude and H_{max} is the maximum altitude planned for the quadrotor flight), and τ is defined by the ratio of (t/t_f), where t is the current time and t_f the total flight time. Five flights were performed following the proposed trajectory, where each flight is represented by a different color in Figure 4.

The flight missions were performed in closed-loop, by using the way-point mode. This mode was used to create a specified flight path that the UAV is able to replicate. First, the pilot selected the points where the drone would fly by using the Phantom controller, and then by using these reference marks on the trajectory using DJI GO app, similar flights could be performed for all four conditions. Then, a comparison of the four configurations has been established based on the same references and flight trajectory.

Figure 4 – Quadrotor trajectory a) with no payload, b) with a fixed payload, c) with a swing payload, and d) with a fixed payload and additional mass, showing reference flight (solid gray line), flight 1 (dashed green line), flight 2 (dash-dotted black line), flight 3 (solid blue line), flight 4 (solid yellow line) and flight 5 (dashed red line).
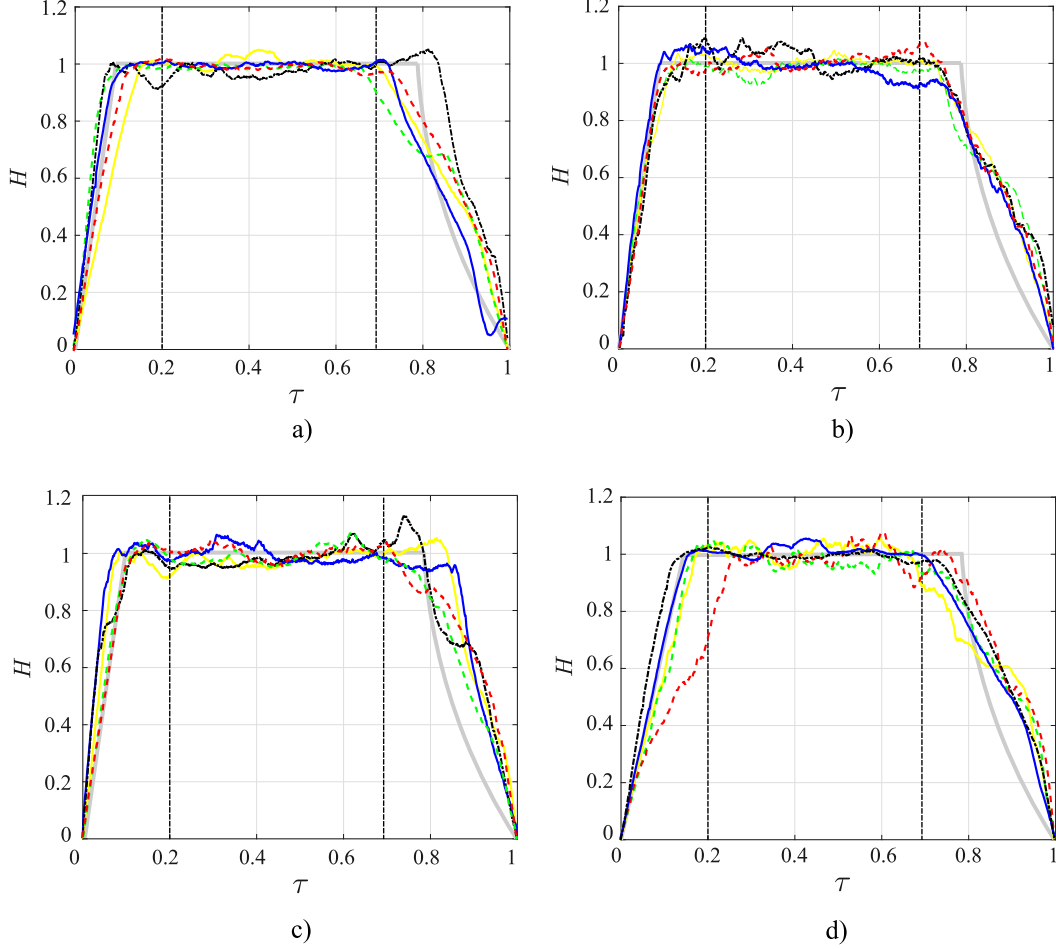
Source: Geronel *et al.* (2022)

The quadrotor flies at 5 meters maximum from the ground, and the transported payload represents approximately 15% of the quadrotor weight (configurations 2 and 3). The fourth configuration is composed of the initial mass of the smartphone plus any additional mass (represented by 150g), which corresponds to around 26% of the quadrotor's weight. The signals are measured separately on the quadrotor and payload. Based on the performed flights, a delay of few seconds was observed when the quadrotor and payload measurements are compared (due to the time to start recording the payload data). The signals are compared herein only in the time domain, focusing on their magnitudes analyses.

2.2.1   Attachment 1 (Baseline) - No Payload

In this first configuration, the quadrotor is free of any additional mass (due to the payload, attachments, and extra mass). To establish the zero point of comparison, lateral accelerations (on x and y axes) of configuration 1 are depicted in Figure 5.

Figure 5 – Acceleration of the quadrotor in a) x axis and b) y axis in the first configuration, showing flight 1 (dashed green line), flight 2 (dash-dotted black line), flight 3 (solid blue line), flight 4 (solid yellow line) and flight 5 (dashed red line).

Source: Geronel *et al.* (2022)

Concerning on Figure 6, the quadrotor exhibits its highest level of acceleration amplitude in its first and third phases, since these phases are related to the rapid increase or decrease of velocity, respectively.

When the quadrotor changes its velocity in a short period of time, its dynamics can be directly affected. Understanding the impact of the change of velocity on each flight phase enhances the chance to design a reliable isolation compartment guaranteeing an attenuation of vibration; this new design should cover the situations of greatest vibration amplitudes.

Additionally, during first phase, the peaks are more concentrated in a shorter period of time, and during the landing (3rd phase) the acceleration amplitudes are more distributed over the time interval. This behavior is due to the ease to raise the quadrotor than to land at a specific point. Figure 6 exhibits the vertical acceleration of the quadrotor with

Figure 6 – Vertical acceleration of the quadrotor in the first configuration (no payload), showing flight 1 (dashed green line), flight 2 (dash-dotted black line), flight 3 (solid blue line), flight 4 (solid yellow line) and flight 5 (dashed red line).

Source: Geronel et al. (2022)

no payload attached.

Figure 5 shows that the accelerations in both directions (x, y) are depicted around 0, thus indicating there is no significant interference of any additional weight. Similarly, in the vertical acceleration (Figure 6), the highest peaks are found in the phases where there is a change of velocity (first and third phases), and in the cruise phase, the acceleration remains constant around $-g$.

2.2.2 Attachment 2 - Fixed Payload

Figure 4 shows that the flight trajectory remains the same for all four configurations. In the second configuration, the payload is attached directly to the quadrotor body (as seen in Figure 3) and no significant displacement is related to the connection between the quadrotor and its payload. Figure 7 depicts the acceleration of the quadrotor in lateral directions for a number of five flights.

In contrast to the first configuration (Figure 5), the acceleration is influenced by the attachment of the payload, as illustrated in Figure 7. The acceleration remains around zero in either the x or y axes; however, it does oscillate more significantly than the case with no payload. The vertical acceleration presents a more significant impact than the

Figure 7 – Acceleration of the quadrotor in a) x axis and b) y axis in the second configuration, showing flight 1 (dashed green line), flight 2 (dash-dotted black line), flight 3 (solid blue line), flight 4 (solid yellow line) and flight 5 (dashed red line).
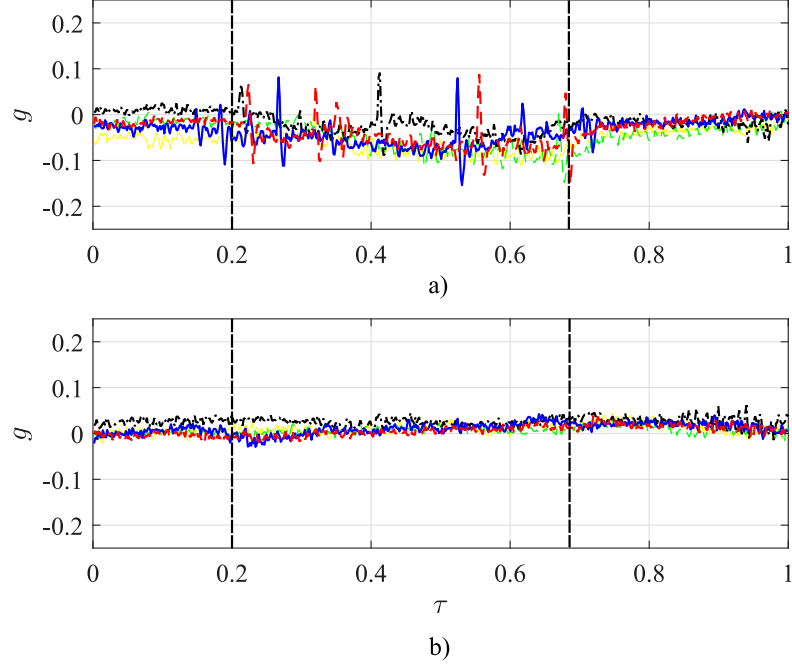
Source: Geronel *et al.* (2022)

Figure 8 – Vertical acceleration of the quadrotor in the second configuration, showing flight 1 (dashed green line), flight 2 (dash-dotted black line), flight 3 (solid blue line), flight 4 (solid yellow line) and flight 5 (dashed red line).
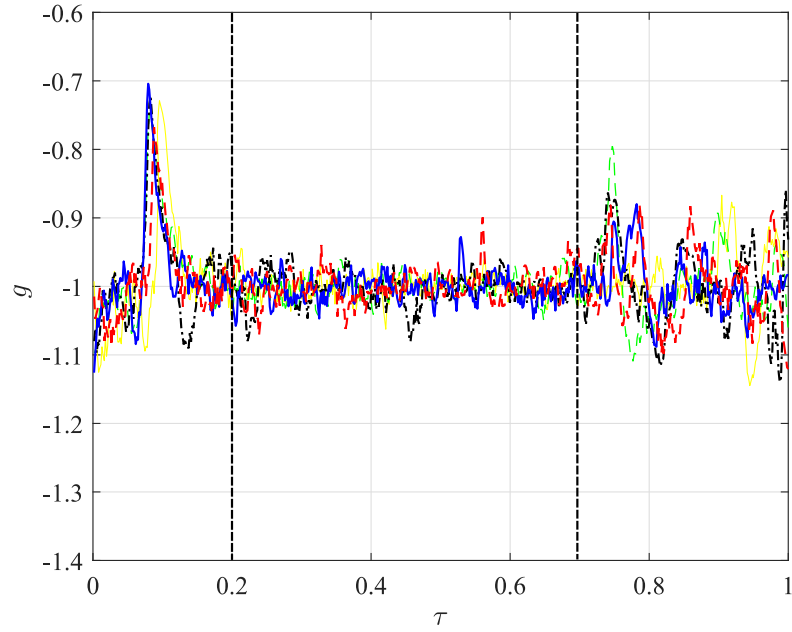
Source: Geronel *et al.* (2022)

accelerations on x and y axes, showing its highest amplitudes. In the time ranges of [0-0.20] and [0.7-1.0], which cover the take-off and landing phases, respectively, the vertical acceleration exhibits higher amplitudes than in the cruise phase. Figure 8 represents the vertical acceleration of the quadrotor in the second configuration

After evaluating the quadrotor acceleration time variation, the payload characteristics must be observed. The lateral accelerations of the payload are shown in Figure 9, and Figure 10 represents the vertical direction, respectively.

Figure 9 – Acceleration of the payload in a) x axis and b) y axis in the second configuration, showing flight 1 (dashed green line), flight 2 (dash-dotted black line), flight 3 (solid blue line), flight 4 (solid yellow line) and flight 5 (dashed red line).
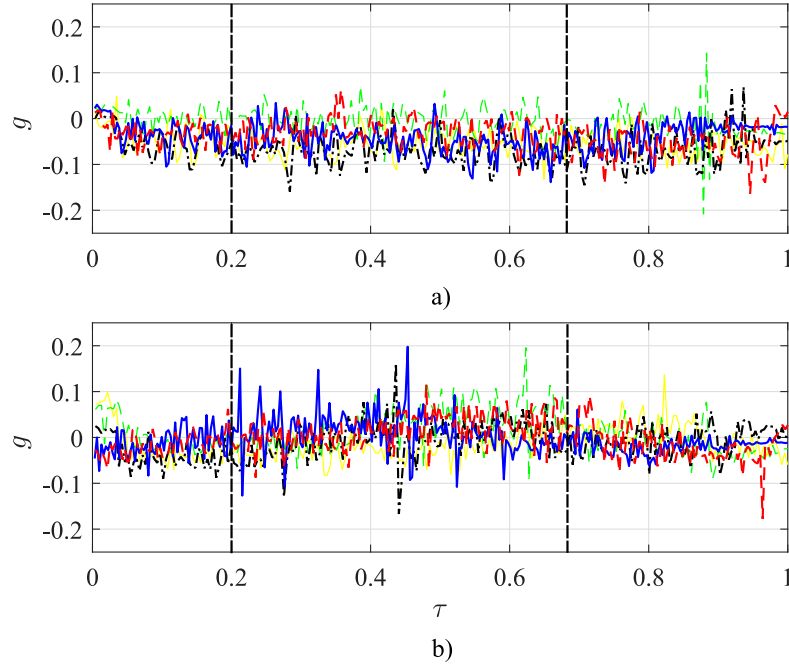
Source: Geronel *et al.* (2022)

Figures 7 and 9 and Figures 8 and 10 show that the acceleration exhibits an amplification of the acceleration on the payload, that is caused mainly by the vibration components of the quadrotor as well as by the external disturbances that the quadrotor is subjected over a flight. Especially during the first and third phases, the accelerations indicate a higher effect due to the sudden accelerations for take-off and the decrease of propeller velocity during the landing phase. Additionally, an extra mass is added to the payload to investigate the differences with the current configuration. Further details regarding the fourth configuration can be found in Section 2.2.4, which includes the influence of the additional mass.

Figure 10 – Vertical acceleration of the payload in the second configuration, showing flight 1 (dashed green line), flight 2 (dash-dotted black line), flight 3 (solid blue line), flight 4 (solid yellow line) and flight 5 (dashed red line).
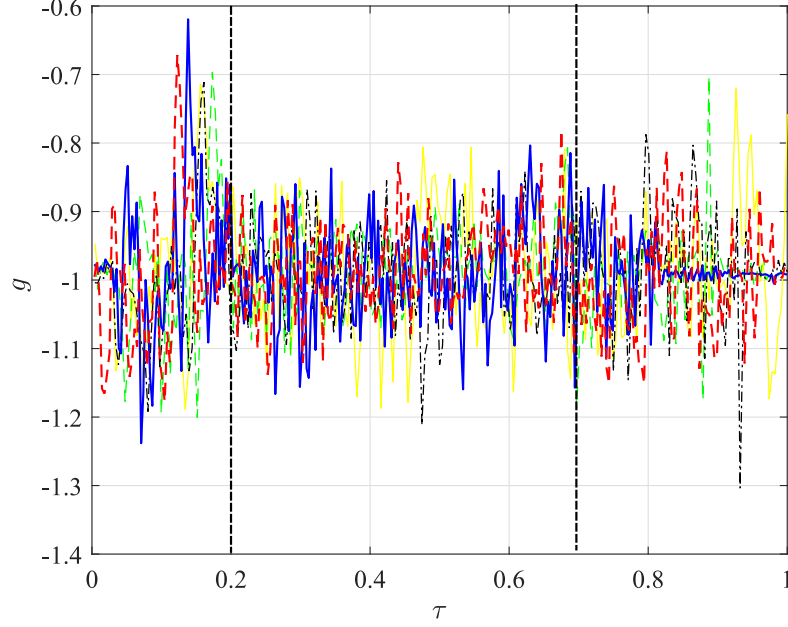
Source: Geronel et al. (2022)

2.2.3 Attachment 3 - Swing Payload

In this configuration, the payload motions affect the quadrotor motion more significantly than the payloads calculated in the other configurations, as seen in the quadrotor time-varying acceleration in Figure 11.

The payload is free to move in all directions (including laterally and vertically). These constant changes have notable impact on the quadrotor performance, by causing higher and constant level of vibrations in the system. Figure 11 depicts the quadrotor acceleration in two directions over five flights for the swing configuration. Similarly, to the lateral direction, in the vertical direction, the acceleration exhibits a greater and more distributed peaks over the trajectory with respect to the first and second configurations. A higher level of vibration is seen over the entire flight in Figure 12.

The impact of the vertical acceleration is more substantial than the one in the lateral one due to the changes in velocities. The payload acceleration is measured using a three-axial accelerometer, as shown in Figures 13 and 14.

Likewise, the payload acceleration is more significant than that of the quadrotor. In comparison to the first configuration (with no influence of any payload), the acceleration of the quadrotor and its payload both exhibit higher peaks over a larger time period in

Figure 11 – Acceleration of the quadrotor in a) *x* axis and b) *y* axis, by using the swing payload configuration, showing flight 1 (dashed green line), flight 2 (dash-dotted black line), flight 3 (solid blue line), flight 4 (solid yellow line) and flight 5 (dashed red line).
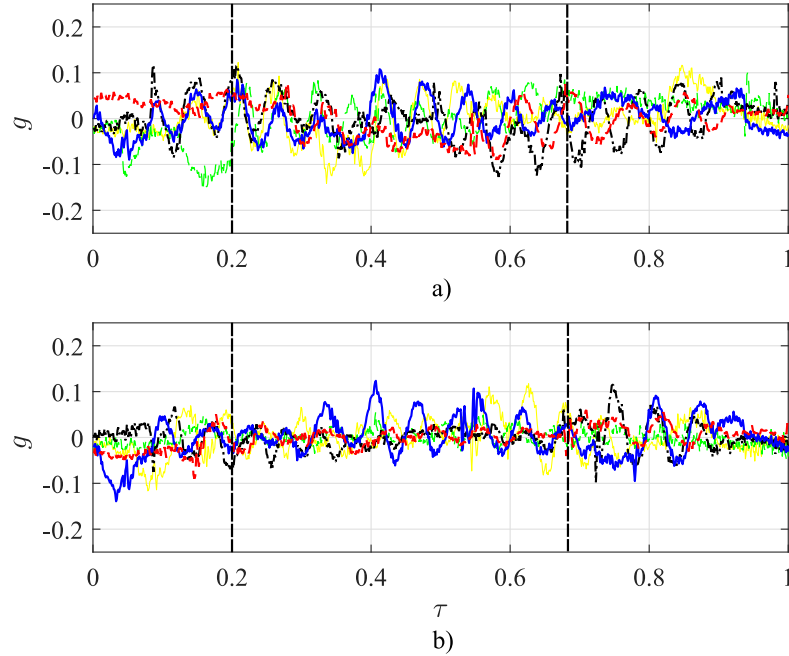
Source: Geronel *et al.* (2022)

Figure 12 – Vertical acceleration of the quadrotor for the swing payload configuration, showing flight 1 (dashed green line), flight 2 (dash-dotted black line), flight 3 (solid blue line), flight 4 (solid yellow line) and flight 5 (dashed red line).
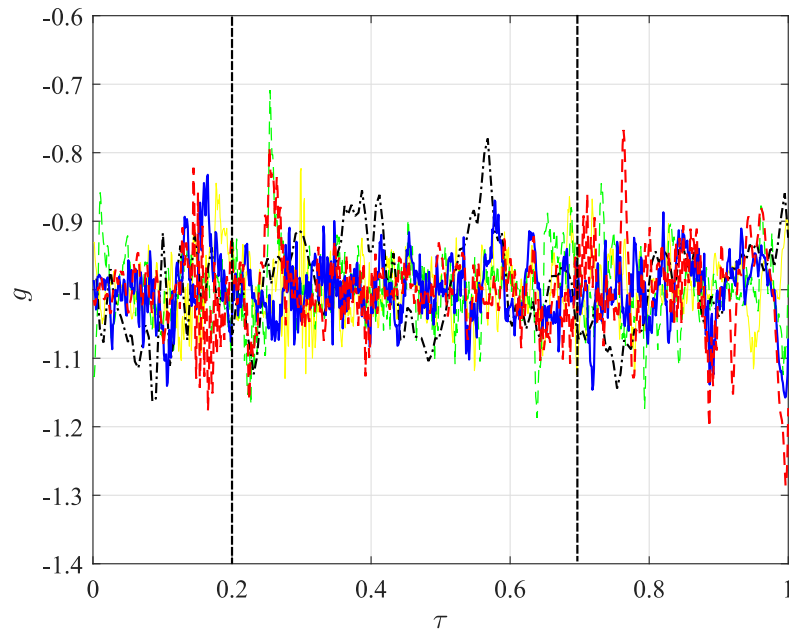
Source: Geronel *et al.* (2022)

Figure 13 – Acceleration of the payload in a) x axis and b) y axis, by using the swing payload configuration, showing flight 1 (dashed green line), flight 2 (dash-dotted black line), flight 3 (solid blue line), flight 4 (solid yellow line) and flight 5 (dashed red line).

a)

b)
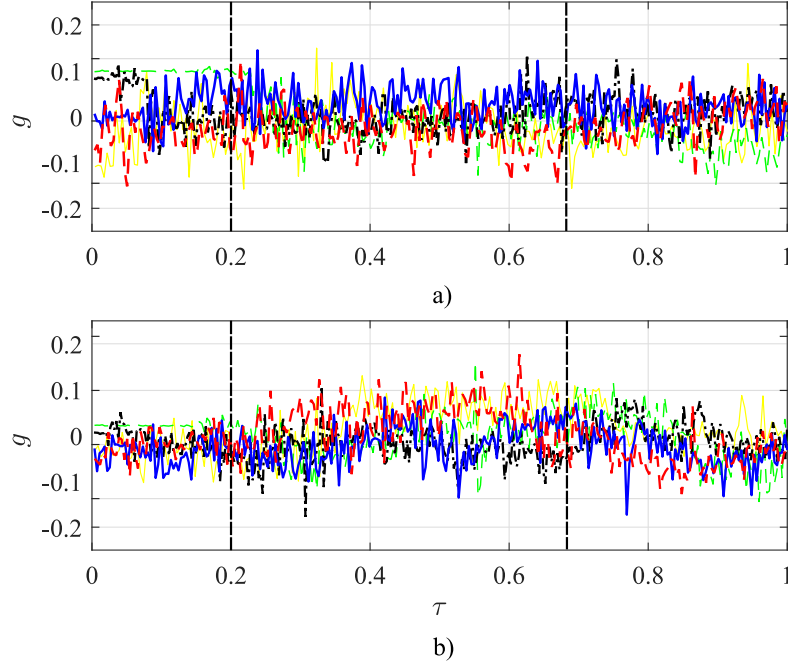
Source: Geronel *et al.* (2022)

Figure 14 – Vertical acceleration of the payload for the swing payload configuration.
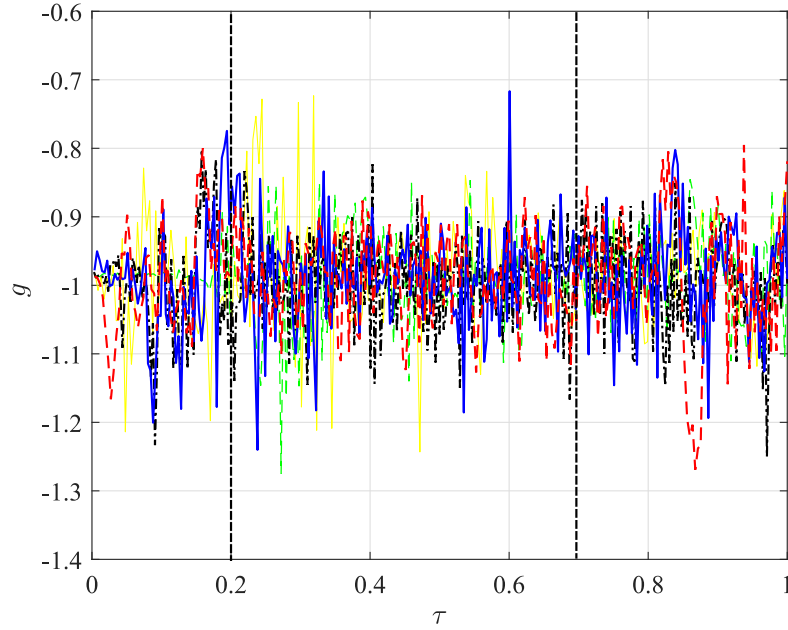
Source: Geronel *et al.* (2022)

the third (swing) configuration, as the payload creates a stronger dynamics behavior that affects the system.

2.2.4   Attachment 4 - Fixed with additional mass

Similarly to the second case, a series of flights (as seen in Figure 4) were performed to understand the effect of the vibration on a quadrotor using an additional mass on the transported payload (Figure 3). The purpose of adding an extra mass (150g) is to analyze how it affects the UAVs and its payload, in comparison to those obtained in the second case. Figure 15 depicts the acceleration of the quadrotor in the x and y axes for a number of five flights in the fourth configuration.

Figure 15 – Acceleration of the quadrotor in a) x axis and b) y axis in the fourth configuration, showing flight 1 (dashed green line), flight 2 (dash-dotted black line), flight 3 (solid blue line), flight 4 (solid yellow line) and flight 5 (dashed red line).
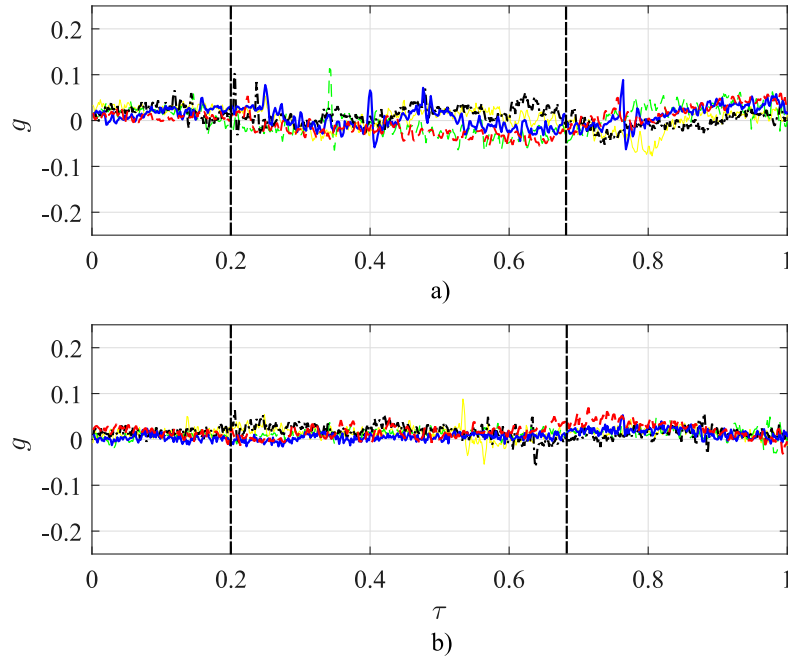
Source: Geronel *et al.* (2022)

Compared to the quadrotor (configuration 1), there is an increase in the acceleration amplitude during the flight in this configuration. In the presence of a heavier payload, the dynamics changed, and some of its effects might be related to the trajectory and acceleration. Figure 16 shows the vertical acceleration of the quadrotor, by emphasizing significant peaks during the first and third phases (take-off and landing).

The acceleration is defined by the rate of speed change, and the faster this change is done, the greater its impact is on the analyzed system. The stiffness forces (F_{ki}) represent the constraint reactions on the attachment points between the quadrotor and its payload. In case when the quadrotor is subjected to large amplitudes over a long time, the payload is directly affected by these forces. The three-axial time-varying acceleration

Figure 16 – Vertical acceleration of the quadrotor in the fourth configuration, showing flight 1 (dashed green line), flight 2 (dash-dotted black line), flight 3 (solid blue line), flight 4 (solid yellow line) and flight 5 (dashed red line).
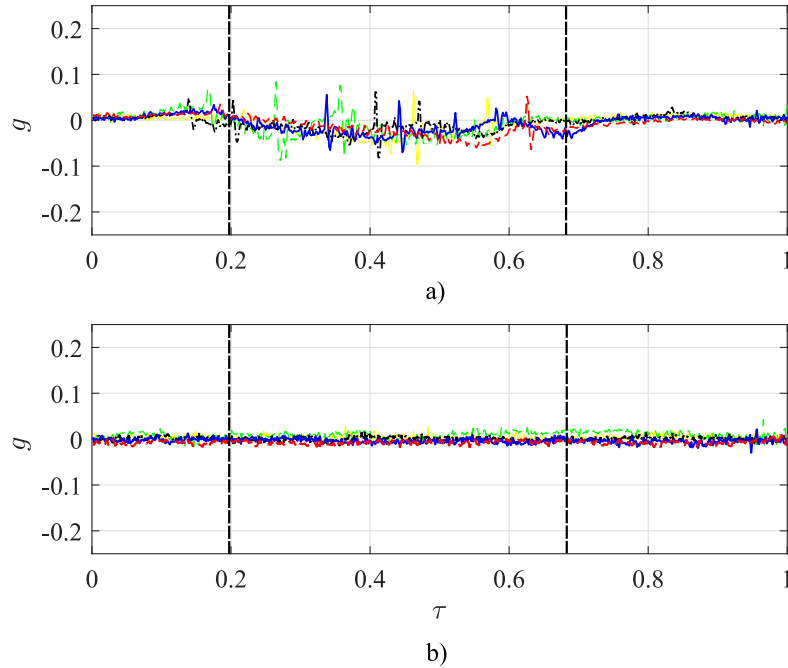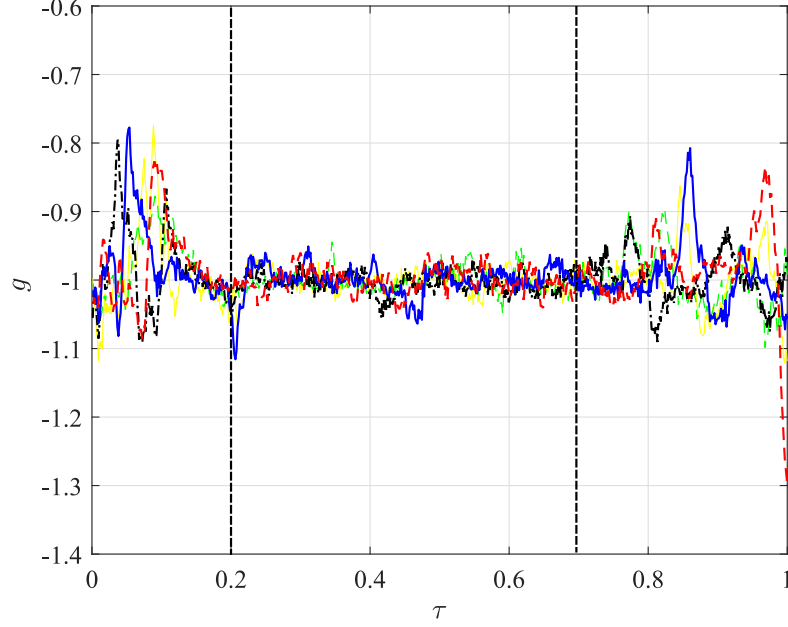

Source: Geronel *et al.* (2022)

of the payload is shown in Figures 17 and 18.

Figure 17 – Acceleration of the payload in a) x axis and b) y axis in fourth configuration, showing flight 1 (dashed green line), flight 2 (dash-dotted black line), flight 3 (solid blue line), flight 4 (solid yellow line) and flight 5 (dashed red line).
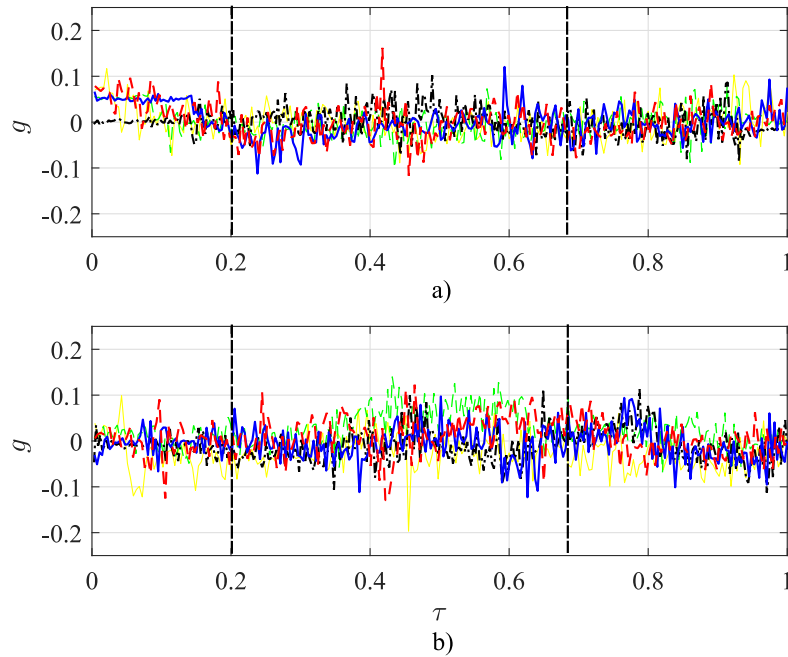
Source: Geronel *et al.* (2022)

Figure 18 – Vertical acceleration of the payload for the fourth configuration in fourth configuration, showing flight 1 (dashed green line), flight 2 (dash-dotted black line), flight 3 (solid blue line), flight 4 (solid yellow line) and flight 5 (dashed red line).
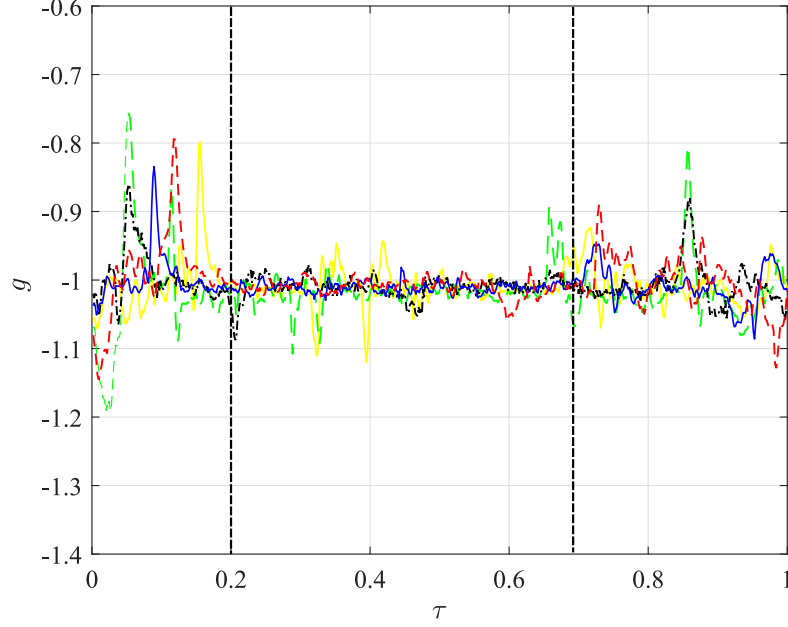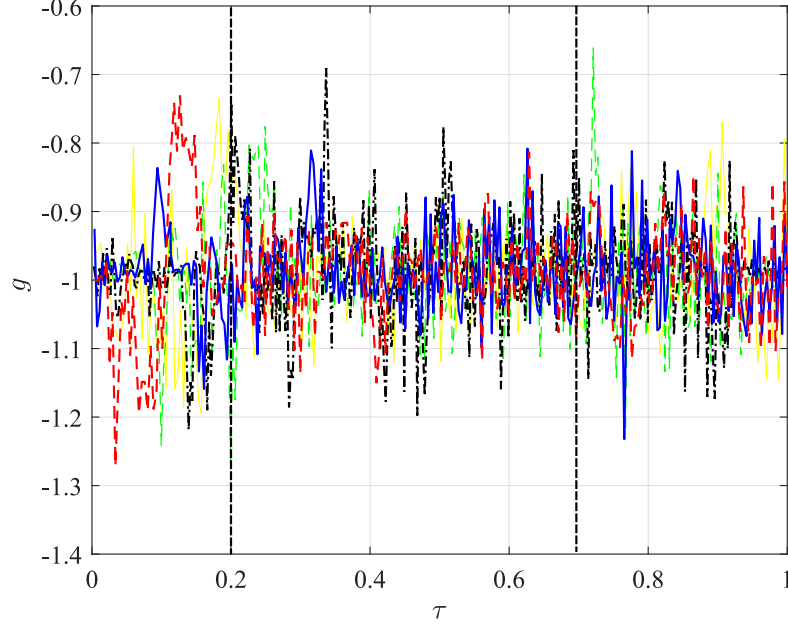

Source: Geronel *et al.* (2022)

Compared to the second configuration, there is a slightly difference in terms of amplitude. Depending on the transported weight, the motors must produce more effort to perform the flight, while the level of vibration would be increased. The fourth case is accomplished to evaluate the addition of mass effect on the payload trajectory oscillation. These analyses provide basic information regarding the influence of mass variation, and further investigations can be done to improve this understanding.

2.3 COMPARISON OF RMS VALUES

The acceleration of the quadrotor and payload presents different characteristics according to the proposed attachment. To evaluate the influence of the acceleration from the quadrotor to the payload, consider the Root Mean Square (RMS) technique, defined as:

$$P_{P,Qi} = \sqrt{\frac{1}{N}(x_1^2 + x_2^2 + ... + x_N^2)} \tag{1}$$

where $P_{P,Qi}$ are the RMS values related to the payload (P_{Pi}) and quadrotor(P_{Qi}) for each flight, respectively. They are calculated (Eq. (1)) by using the acceleration data expressed

in terms of the variable x_j, where index j $(j = 1, 2, ..., N)$ represents each data point in the time history (composed of N data points) and $x_j = (a_j^{(i)} - \bar{a}^{(i)})$. The term $a_j^{(i)}$ corresponds to the current acceleration data and $\bar{a}^{(i)}$ is the mean value of the acceleration along the entire time history for the specific flight.

The average RMS is therefore used to define its mean value by considering all flights, where for a quadrotor is expressed as $P_Q = \sum_{i=1}^{N_F}(P_{Qi}/N_F)$, where N_F is the total number of flights ($N_F = 5$ for each configuration). Additionally, for the payload is calculated by the following expression $P_P = \sum_{i=1}^{N_F}(P_{Pi}/N_F)$. Table 1 shows the average RMS values of the three-axial accelerations for each mission. Figure 19 shows the average of RMS ($P_{P,Q}$) acceleration for each mission in their different directions.

Table 1 – The average of the RMS values for each mission.

Direction	$P_{P,Qi}$	x	y	z
Config. 1	P_Q	0.2065	0.0057	0.0347
	P_P	-	-	-
Config. 2	P_Q	0.0266	0.0153	0.0467
	P_P	0.0354	0.0406	0.0772
Config. 3	P_Q	0.0439	0.0303	0.0583
	P_P	0.0589	0.0688	0.0802
Config. 4	P_Q	0.0261	0.0125	0.0391
	P_P	0.0399	0.0387	0.0735

Source: Geronel *et al.* (2022)

As presented in Figure 19, the effect of the payload modifies the dynamics of the quadrotor, in addition to enhancing the vibration level on the transported payload itself. Regardless the analyzed direction and configuration, the average of the RMS is higher in comparison to the one of the first configuration (absence of payload). Additionally, the ratio of the Root Mean Square is defined by:

$$P_{Ri} = 100[(P_{Pi}/P_{Qi}) - 1] \tag{2}$$

where $i = 2, 3, 4$, referring to the corresponding configurations, where 2 is the fixed configuration, 3 is the swing payload, and 4 is the additional mass on the payload.

Table 2 – The ratio of RMS (P_{Ri}) for each mission.

Direction	x	y	z
P_{R2}	33.08%	165.36%	65.31%
P_{R3}	34.17%	127.06%	37.56%
P_{R4}	52.87%	209.60%	87.98%

Source: Geronel *et al.* (2022)

Figure 19 – The average RMS for each mission, where the payload effect ■, and the quadrotor ■.
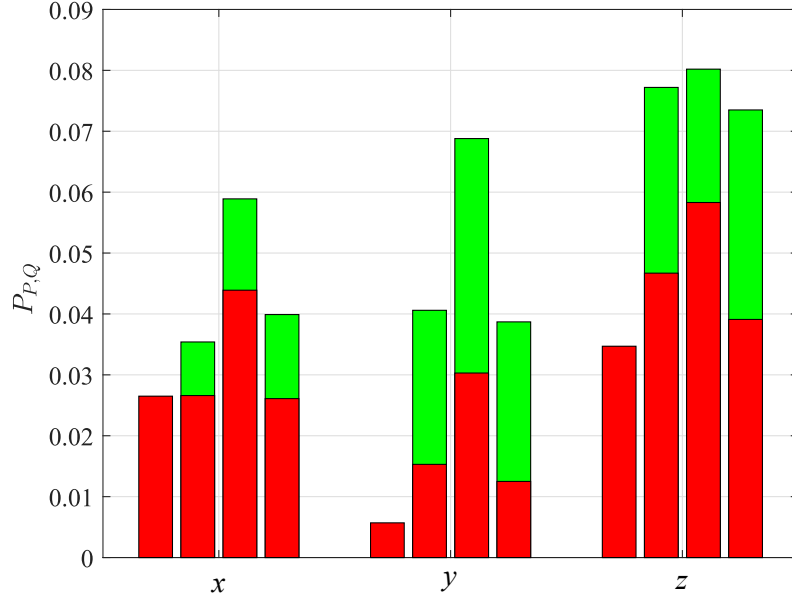
Source: Geronel *et al.* (2022)

There is an increase in the RMS values for the accelerations in all directions when the payload and the quadrotor motions are compared, as seen in Tables 1-2. The acceleration of the y direction gave the highest percentage of the P_{Ri}, however, based on its absolute value, the vertical acceleration axis contributes more significantly to the vibration of the system than the acceleration on the other axes. Figure 20 shows the spectral response of the configurations 1 and 2, while Figure 20 depicts configurations 1 and 3.

Additionally, the presence of an additional mass alters the dynamics of a UAV, and consequently the natural frequency associated to the resulting system. As shown in previous sections (Section 2.2.1 - Section 2.2.3 and Figure 19), the energy associated with the presence of the payload is higher in comparison to the payload absence, and peaks have been created due to the additional mass.

The natural frequency of a fixed payload is calculated using the attachment stiffness and the payload mass, while for a suspended payload configuration, the natural frequency is inversely proportional to the square root of the cable length. The results show that both the attached swing and fixed payload induces dominant peaks at specific frequencies, which change the vibration characteristics over the frequency.

Figure 20 – Vibration energy of the proposed attachments, showing the absence of the payload (Config. 1 - solid blue line), and the presence of fixed payload (Config. 2 - dashed red line).
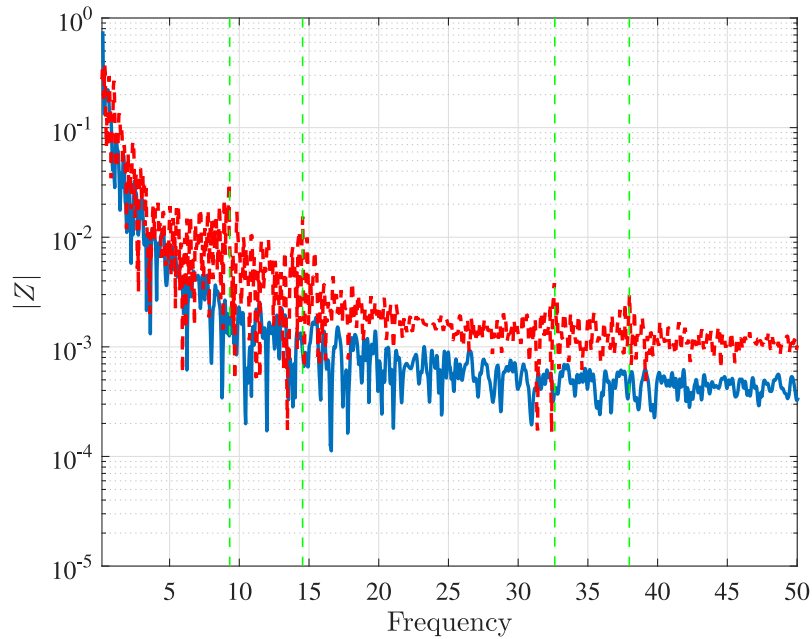
Source: Geronel *et al.* (2022)

Figure 21 – Vibration energy of the proposed attachments, showing the absence of the payload (Config. 1 - solid blue line), and the presence of suspended payload (Config. 3 - dashed red line).
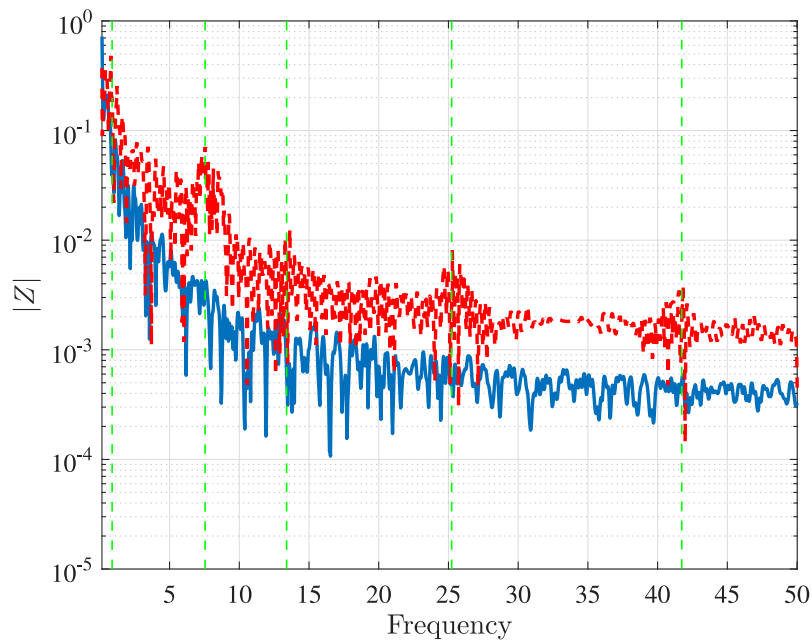
Source: Geronel *et al.* (2022)

2.4   FINAL REMARKS

This chapter presented experimental tests for four attachment's configurations (no payload, fixed, fixed with additional mass and swing payload). These proposed attachments are used to evaluate the level of vibration on the payload during a common flight path. This path has been obtained including three phases (take-off, cruise and landing), and a related result is obtained for each proposed configuration. The acceleration was measured along the three main axes, and the acceleration on the x and y axes were around 0, while in the vertical direction (z), the acceleration was around $-g$.

The results have shown an amplification of acceleration levels of the payload in relation to the quadrotor for all the considered configurations. This increase was verified in all directions (x, y, z), ranging from about 30% to more than 200%. Understanding the time-varying amplitude and how each phase influences on the acceleration characteristics may be necessary to design an efficient system of transportation, and then successfully mitigating its negative effects on medical cargoes.

The use of UAVs in medical transportation will be widely spread worldwide and will ensure a more accessible distribution of supplies despite geographical and economical challenges. The development of new UAVs attachments and the expected increases in UAV performance guarantee higher payload capacity, in terms of larger dimensions (size and increased weight). Consequently, to the possibility of transporting them over longer times and distances. Therefore, designing and attaching a safe compartment to transport the payload is crucial for the medical transportation.

3 A BRIEF STATE-OF-THE-ART REVIEW

Unmanned Aerial Vehicles have been extensively used in different areas, including agriculture, surveillance, military operations, and products delivery tasks. More recently, UAVs have been used into new specialized fields, such as medical products transportation mainly to overcome some of the current challenges. The UAVs used to transport medical products allows one to address critical missions, such as those ones involved in natural disaster surveillance, rapid delivery on rough terrains, and it contributes to time and costs reductions.

This chapter exhibits a brief state-of-art review focus on discussing vibration characteristics of a payload carried by UAVs. Section 3.1 introduces the main aspects of using UAVs for transporting products. Section 3.2 presents recent works that assess the effect of vibrations on UAVs, whereas Section 3.3 addresses the main challenges of the UAV integration in the heath care system, including the current legislation, effects of vibration and temperature on the payload and introduces insights on future possibilities for their use to transport medical and hospital products.

3.1 COMMERCIAL USE OF UAVs

Given the constant development of UAV applications, the need to regulate their use has become crucial, as the air space is regulated by civil and international aviation authorities. Regulators need to ensure that both large and small UAVs can and do communicate with each other as well as with air traffic control authorities in order to guarantee safe operations and determine certified flight zones. Flight regulations determine the criteria for no-fly zones, the conditions under which UAVs can fly (operator's line of sight, minimal distance over people), and prioritize sectors with the aim to overcome the country's challenges (geographical and/or economical). Several countries have issued national aviation rules, that are categorized according to the aircraft purpose, altitude,

weight and dimensions, flight envelope along with general safety restrictions.

Generally, certification rules present several similarities regardless of the country, and some procedures must be followed to use a UAV all over the world. Certain UAVs need to fly below 122 meters, remain in the pilot's sightline, respect the privacy of private places, stay away from public events or emergencies, as well as keep a safe distance from airports. In addition, there is a minimum age to pilot a UAV, and a special online registration may be required depending on UAV specifications. Companies and organizations began to adopt aerial vehicle technology for their business needs over eight years ago. According to the type of payload and the distance to be traveled, some attachments have been designed to protect and maintain the quality of payloads. Figure 22 shows the main types of attachments used in quadrotor transportation.

The swing payload method is often adopted for heavy transportation, by requiring multiple UAVs to execute the task properly. Fixed payload attachments are commonly utilized for commercial transportation, especially for light payload and fragile goods. With these two payload methods and the recent advances in UAVs, many companies are adopting and integrating drone technology for their business needs. Table 3 lists some of these companies, and the UAV's main parameters.
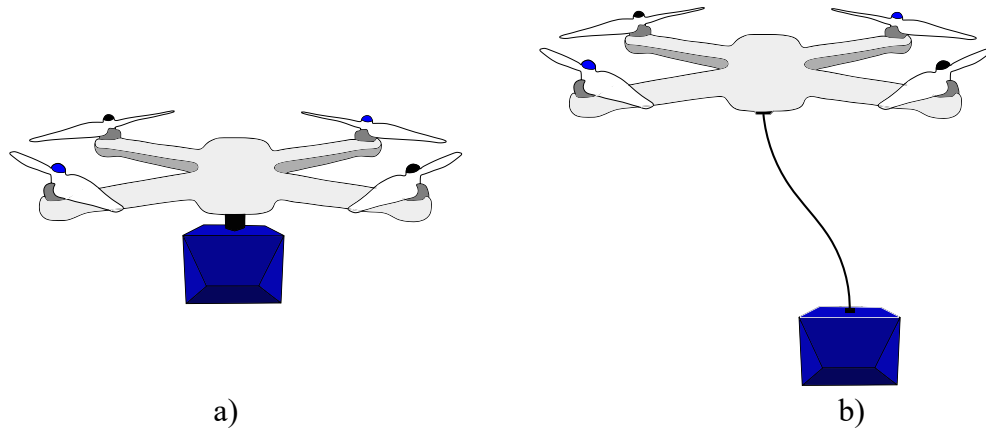
Figure 22 – Schematic illustration of quadrotor carrying a payload: a) fixed payload and b) swing payload.

Source: Geronel *et al.* (2022)

Table 3 – Companies that use UAVs as part of their business

Company	Origin	Payload	Range	Speed	Attachment
Airbus Skyways	Europe	5.00kg	30km	70km/h	Fixed
Amazon Prime Air	United States	2.25kg	16km	80km/h	Fixed
Dhl Express	Germany	4.00kg	65km	130km/h	Fixed
Drone Delivery Canada	Canada	4.50kg	30km	70km/h	Fixed
Jd.com	China	10.0kg	10km	100km/h	Fixed
Matternet	United States	2.25kg	20km	70km/h	Fixed
Wingcopter	Germany	6.00kg	40km	100km/h	Fixed

Source: Geronel *et al.* (2022)

3.2 UAV VIBRATION CHARACTERISTICS

Advances in technology and costs reduction have led to increasing the use of Unmanned Aerial Vehicles over the years, and the ability to carry different payload, such as sensors, cameras, monitoring equipment and medicines has spread their use in different fields. The size and dimension of the payload, environmental disturbances, vibration and maneuvers can negatively influence the UAV performance (RADKOWSKI; SZULIM, 2014). In some specific tasks (fragile products transportation), such as medical goods, electronic devices, or certain foods, it is especially important to keep the payload free of excessive perturbations that the aerial vehicle is subjected over a flight (CORNELIUS *et al.*, 2015). These perturbation forces can lead to detrimental consequences to the transported payload (even requiring its disposal, in extreme situations).

Since a UAV system is composed of numerous power transmission systems (rotor and motor types), several structural parts and components, unwanted vibrations can be generated and then influencing the whole system. For instance, Radkowski and Szulim (2014) investigate the vibrations that appear due to flight maneuvers. The appearance of angular velocities, over a UAV maneuvers, might negatively impact on the UAV and its components performance, by creating adverse vibration forces. Experimental tests are performed to confirm the occurrence of vibrations and evaluate the efficiency of restored forces added to the system in order to reduce these phenomena. Micro-Electromechanical Systems (MEMS) sensors are usually used in the UAVs to estimate their position and attitude angles variations in real time. However, the negative vibration impact can lead to a lower accuracy of the measurements provided by the sensors on the UAV. Kedadouche *et al.* (2018) have shown that in the absence of any specific absorber, it is verified that all UAV content frequencies were practically transmitted to the autopilot. Then, an isolator prototype is designed to attenuate the undesired force, thus resulting in 80% of efficiency

in terms of vibration sources attenuation. Since the UAVs are currently transporting different payloads, the source of vibration related to the attachment of sub-systems to the main body of the UAV, have been conquering significant importance in the literature.

The addition of an attached payload has a significant influence on UAVs dynamics, since it might change its flight characteristics, besides creating new uncertainties to the controller design (GERONEL; BUENO, 2021). Given this context, different techniques and controllers related to the payload vibration have recently been investigated, such as an active vibration absorption (CARBAJA *et al.*, 2022), polynomial trajectories (ALKOMY; SHAN, 2021), and adaptive controllers (WU; XIE; LI, 2021). Zhou *et al.* (2016) have assessed two controllers (Proportional Derivative and Sliding Mode Control) to investigate the mass uncertainties on the quadrotor dynamics. In the presence of large uncertainties, the PD failed to successfully control the tracking trajectory and quadrotor stability, while the SMC presented better robustness against disturbances. Pounds, Bersak and Dollar (2012) investigate the presence of a payload on UAVs and helicopters. Proportional Integral and Derivative (PID) control is chosen to assess the UAV stability subjected to parameter variations, such as payload changes and offset payloads (not centered to the vehicle CoG).

Overall, the payload dynamics are also treated as a disturbance force, and a rigid attachment is frequently considered to obtain the mathematical formulation. In particular, this free motion is a critical problem for the flight safety and performance, as well as to the payload integrity. Klausen, Fossen and Johansen (2015) design a nonlinear controller based on the BackStepping technique to ensure the trajectory tracking regardless of the payload motion. First, the payload is modeled as a pendulum, and a rigid attachment is assumed between the UAV and its payload. Then, the BackStepping control is used to generate a reference trajectory, while the Input-Shape Filtering is chosen to minimize the payload residual oscillation. The proposed controller perfectly cancel the impact of payload movements as well as present a better tracking of the desired trajectory. Klausen, Fossen and Johansen (2017) combine the Backstepping technique with the swing damping to attenuate the suspended payload oscillations and external disturbances. The proposed controller is evaluated by simulations and experiments, showing a great reduction of angular displacement.

Kusznir and Smoczek (2020) have investigated the use of Sliding Mode Control for suppressing the vibrations of a cable-suspended payload. A Feedback Controller is used to design the altitude and attitude controllers, while the SMC is adopted to reduce the payload vibration caused by horizontal motion. The SMC parameters are calculated by

combining adaptive pole displacement with the vertical component of the thrust as a time-varying parameter. To evaluate the controller performance, several uncertainties are tested, revealing that SMC reduced maximum swing angle by 56% and significantly decreased the residual system vibrations. Sanchez *et al.* (2021) design two nonlinear controllers for stabilizing a suspended payload carried by a quadrotor. The control laws utilize the direct relationship between the payload oscillation and aircraft horizontal movement. Therefore, the proposed controller law could simultaneously guarantee both the desired trajectory optimization and payload oscillation reduction. Numerical experiments and experimental tests have shown that the proposed controller efficiently suppressed the swing angles during the quadrotor flight.

External disturbances can also negatively affect the UAV and its payload performance, by increasing the undesired vibration. In this present thesis, the controller analysis have been studied to investigate not only the flight performance, as traditionally found in the literature, but also to verify the relative trajectory oscillation influence over the quadrotor dynamics under external disturbances (GERONEL; BOTEZ; BUENO, 2022a). Fast Fourier Transform and Performance Indices are employed to evaluate these undesired vibrations characteristics in different phases of the flight. This approach is also used to characterize the vibration influence when the UAV and its payload are subjected to continuous wind effects (in this case, modeled as Dryden). The objective of this study is to evaluate how the payload behaves in different flight phases and under critical situations.

Wu, Xie and Li (2021) propose a disturbance attenuation control to enhance the quadrotor stabilization under external disturbances. This approach introduces an adaptive parameter for the position control to estimate the payload mass and thus to improve the robustness of the system. The estimated payload mass was then combined with the state feedback control with the aim to enhance the trajectory tracking performance and disturbances rejection. Simulation results have demonstrated better responses than those obtained with the traditional Sliding Mode Control, when considering unknown mass and air disturbances. Wang, Mu and Zhang (2017) study the use of an Adaptive Sliding Mode Control to evaluate the performance of a UAV flight under disturbances and unknown mass. The ASMC aims to maintain the controller robustness regardless these negative impact. The proposed strategy allows the UAV safely to pick up and deliver payloads of unknown mass, even in the presence of disturbances during the flight. In comparison to the traditional LQR, the proposed strategy gives a better control performance especially during the mass change and release phases.

Concerning the suspended-payload dynamics, the interconnected system (UAV and its

payload) is commonly modeled by Udwadia-Kalaba equations (BEHZAD; MAJDEDDIN; IMAN, 2019; HUANG *et al.*, 2016); however in this thesis a new integration is developed by using constraint forces representation (GERONEL; BOTEZ; BUENO, 2022b). Additionally, the flexibility has been frequently studied in crane dynamics (SHIANG; CANNON; GORMAN, 2000; FATEHI; EGHTESAD; AMJADIFARD, 2014); however it is a very recent topic in UAV applications. The payload vibration analysis have been gaining increasing popularity, since it is a common configuration adopted by commercial UAV companies in medical transportation field.

In addition, the phenomenon of vibration has been studied using different approaches in medical field, as it is one of the most critical concerns in the design of modern UAVs. It is known that depending on its amplitude and frequency, vibration can cause various impacts on helicopters, quadrotors, and other aerial systems. In helicopters, a few numbers of components cause most of the notable vibration, including rotors, main gearbox and fuselage. If the vibration amplitude is large or time exposure is long, a decrease of equipment reliability, components fatigue life, and passenger comfort may occur. For UAVs, depending on the number and velocity of the rotor and their configuration, the vibration can be transmitted differently to suspended payloads (VERMA *et al.*, 2020). Several types of vibrations typically encountered by UAVs during their flight trajectory is depicted in Figure 23.

Figure 23 – Vibration in Unmanned Aerial Vehicles.
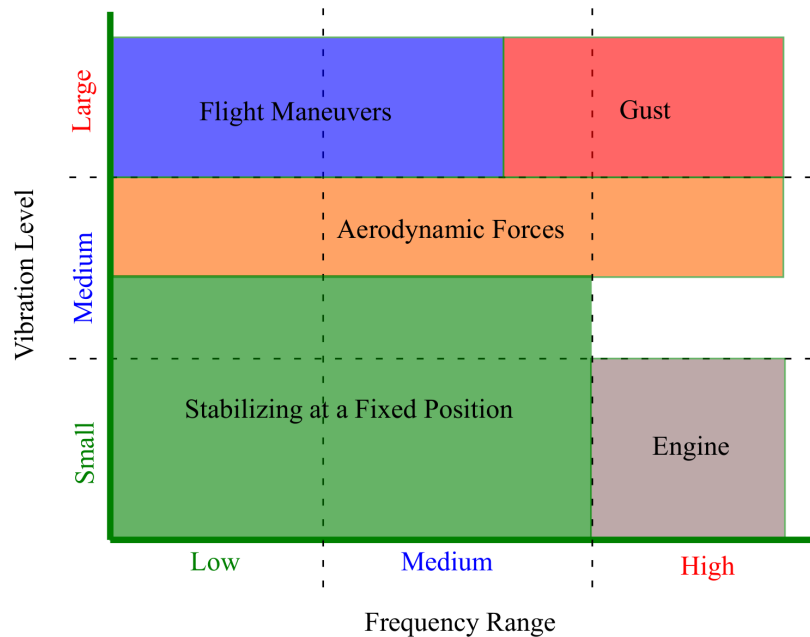
Source: Adapted from Verma *et al.* (2020)

Therefore, these oscillations caused by an attached mass, external disturbances

and different dynamic configurations have become an important topic in UAV medical transportation. On the other hand, this operation generates lots of questions regarding the potential flight effects on the medical goods stability. Oakey *et al.* (2021a) have investigated the vibration characteristics within UAV flight, by showing its influence on the medical insulin quality, and comparing then with road transportation. Two types of UAVs and a series of accelerometers (fitted on their fuselage and in their packing) are used to evaluate the vibration transmission over a proposed flight. Overall, the vibration levels from the UAV are higher than those for road transportation. Therefore, establishing the frequency dependent sensitivity of medicine vibration is an important initial procedure to employing a UAV (and its correct payload attachment) for medical transportation tasks.

3.3 UAVs IN THE MEDICAL FIELD

Spurred by the need to overcome geographical and economical challenges, UAVs began to be used in medical material transportation, including medicine (HAIDARI *et al.*, 2016)-(HII; COURTNEY; ROYALL, 2019), and its applications such as organs (HAMPSON, 2019), blood products (AMUKELE *et al.*, 2017a) and other medical supplies (CLAESSON *et al.*, 2016) transportation. Currently, UAVs represent an interesting solution to be used in the medical field mainly due to several benefits in terms of delivery time, reduced carbon footprint, a more dynamic response between hospitals and patients, as well as to increase the capacities to overcome some logistic and geographic challenges (such as remote areas and poor infrastructures).

This significant advance in medical transportation presents a potential solution to logistic challenges (avoiding traffic delays, accommodating a lack of infrastructure and/or emergency situations), while offering lower costs and easier access to remote areas and also ensures a quick transportation of medical products over short distances. It is estimated that the delivery cost of using UAVs is around 80% lower than what of a conventional service (AURAMBOUT; GKOUMAS; CIUFFO, 2019). At least 20% of the world's population lack any kind of medicine, thus the use of drones can offer access to those who need it the most. Since poor road and challenging terrain accesses are found all over the world, the UAV deliveries becomes one of the most promising technologies to overcome these difficulties.

The overall feasibility, risks, potential demand, and the main advantages of using UAVs to deliver medical products have been explored in (THIELS *et al.*, 2015). While some medical goods are not available in every hospital due to their costs and short

shelf life (since they are not needed in daily use), they can be crucial for saving lives specific occurrences, such as mass accidents or natural disasters. The UAV rapid delivery, low operating cost and its ability to travel over closed roads make UAVs particularly important for these specific tasks. Therefore, some conditions must be tested, since they can appear in UAVs transportation, such as vibrations, rapid changes in pressure, humidity, and temperature.

Based on the growing approval of regulations worldwide, the leading UAVs manufacturers are conducting experiments to enable use UAVs in healthcare delivery such as medicine, blood, vaccines and organs. Ambulance drones also be used as portable defibrillators. A flight of three minutes carrying medical supplies was marked by the Flirtey company as the first UAV delivery to a health clinic in Wise (LING; DRAGHIC, 2019). Vayu aims to develop UAVs to transport medical supplies in developing countries. The Vayu UAVs works mainly in Madagascar, with the capacity to carry 2kg with the range of 60km (KREY, 2018). Nowadays, Zipline represents the most promising alternative of aerial delivery in Rwanda, by delivering blood samples from central distribution to surrounding smaller hospitals (ACKERMAN; STRICKLAND, 2018). The Zipline presents UAVs that can carry 1.5 along 70km, and with the velocity of 100km/h. The Wingcopter 178 has the capacity of carrying up to 6kg and it flew from Ireland to the Aran Islands to deliver insulin from the medical providers to patients (KEEFFE; JOHNSON; MARAKA, 2020). Additionally, several partnerships between start-ups and UAVs logistics networks have been signed, such as UPS and Matternet (CICHOSZ, 2019), Swoop aero and Wingcopter (GOVINDARAJAN; SRIDHARAN, 2020), Swiss Post and Matternet (MION, 2019), and Volansi and Merck (JOHNSON *et al.*, 2021). With the advance of healthcare systems, many hospitals services have expanded into new regions, making the logistic and transportation requirements of medical goods becoming an ever-growing challenge. Table 4 presents one of the first companies wich employed UAVs in medical transportation.

These companies are gaining positive acceptance by governments in different countries, which allows them to expand quickly their operations. Besides transporting blood samples, Zipline also offers alternative to transport chemotherapy medication to tumor patients in their own home. This transportation predicts a $169 of costs reduction per patient, 18% higher medication adherence and 28% in decrease of transportation costs. More recently, Zipline delivered its first vaccine to Africa. Wingcopter is one of the first companies to work in South Pacific Island, Tanzania, Malawi, and Scotland to deliver medical products, including laboratory samples, medicines, and vaccines. Other examples

Table 4 – First companies that used UAVs to transport medical and hospital products

Company	Location	Year	UAV Type	Item Type
Flirtey	Virginia	July 2015	Six-rotor	Med. Supply
Vayu	Madagascar	July 2016	Fixed-Wing	Blood
Zipline	Rwanda	Oct. 2016	Fixed-Wing	Blood
Swiss Post/Matternet	Switzerland	March 2017	Quadrotor	Blood
Swoop Aero/Wingcopter	Vanuatu	Dec. 2018	Quadrotor	Vaccines
Wingcopter	Ireland	Sept. 2019	VTOL	Insulin
UPS and Matternet	North Carolina	Dec. 2019	Quadrotor	Specimens
Volansi and Merck	Bahamas	July 2020	VTOL	Medicines

Source: Prepared by the author.

include Volansi, that aims to transport cold-chain medicines, such as aerosol sprays (for asthma's treatment), eye drops (for glaucoma), diabetes medications, and COVID-19 vaccines, and Matternet, in collaboration with UPS, to deliver several types of medical products in different worldwide countries, such as Japan, Germany, United States, and Switzerland (SIGARI; BIBERTHALER, 2021).

The inclusion of a new process or product into a existing health care system can be challenging and complex. Countries and companies must work together to evaluate the feasibility to integrating the UAVs in the current health system, assessing what processes have to change, how they impact on the workflow and how this type of transportation improve the health outcomes. Therefore, the use of UAVs aims to achieve fast and safe transportation and a more dynamic coordination between providers and patients, by improving the overall access to health care systems. Despite these advantages, there are several current challenges related to vibration sensitive, regulatory issues, safety concerns and air traffic congestion that must be individually evaluated based on the region needs.

3.3.1 Legislation

The opening market of aerial vehicles to be used by civil people has started a new area of aviation (VOORDE *et al.*, 2017). Although UAVs can be employed to deliver different types of products, their presence inside civil areas lead to the need of regulating their operation (JR; PARKER; VIGNESH, 2018). In general, the operators of heavier UAVs require some pre-requisites before flying, such as appropriate licenses, flight height limitation, and restriction to certain areas. Thus, these legal aspects present a direct impact on the development of new aerial vehicles to be used on a broader scale.

Usually safety is the major challenge with advance of UAVs services. Note that

citizens can be potentially affected by the UAVs, by losing their part of privacy, since UAVs often present a camera attached to its body-frame (ALWATEER; LOKE, 2020). In addition, regulations must be used to safely split up recreational purposes, commercial UAVs, permitted and prohibited areas in urban and non-urban areas (GATTESCHI *et al.*, 2015). Thus, current challenges include the coexistence of UAVs for recreational and commercial (crewed models) purposes in common airspace, and how the UAVs can be integrated with conventional ground logistics to achieve a more sustainable and efficient distribution of medical products. In a near future, license plates for UAVs can become a reality, analogous to registration for vehicles, by using physical or electronic radio tagging (SCHNEIDER, 2017).

Different countries worldwide have issued their national legislation to establish specific rules of using UAVs based on some criteria, such as the vehicle' size, weight, flight altitude, purpose of use, and autonomy (TSIAMIS; EFTHYMIOU; TSAGARAKIS, 2019). These legislation aim to manage the widespread employment of UAVs, by limiting their access in specific places with the aims to provide safety and privacy to population (CLARKE, 2014). The first use of UAVs in medical application was reported in 2010 in Haiti to investigate the damage scale caused by an earthquake (KONERT; SMEREKA; SZARPAK, 2019). However, it took five more years to have the first published report of a medicine being transported by UAV (in 2015, USA) (LING; DRAGHIC, 2019).

Fifteen countries have been selected to investigate their current legislation about UAVs. They are (alphabetic order): Australia, Belgium, Brazil, Canada, Chile, China, Germany, Italy, Israel, Japan, Mexico, Portugal, Spain, United Kingdom and United States. This discussion is focused on the UAVs size, weight, flight altitude as restrictions regarding legal documents and charges. The analyzed criteria are defined by C1=flying distance restriction, C2=weight classification, C3=flight permission, C4=registration, C5=safety insurance, C6=piloting certificate, C7= minimum age for pilot, and C8=weather condition. Table 5 lists some of the criteria used to define the current legislation for unmanned aerial vehicles worldwide.

Based on Table 5, only two countries had the maximum of the analyzed criteria (8), 3 had 7 criteria, 2 had 6 criteria, 6 countries had 5 criteria and 2 present only 4 criteria. In addition, all the countries classify UAVs based on their weight and altitude restriction, only Japan and Israel do not mention any minimum age, and Belgium and Canada specify any weather condition. The minimum age required to pilot them differs in each country, e.g. Germany, Belgium, Australia and US establish 16 years, whereas Brazil, China, Italy and Spain establish 18. On the other hand, there are countries that divide the ages and

Table 5 – Analyzed criteria to define the national legislation in different countries

Country	C1	C2	C3	C4	C5	C6	C7	C8	Total
Australia	√	√	√			√	√		5
Belgium	√	√	√	√	√	√	√	√	8
Brazil	√	√	√	√		√	√		6
Canada	√	√	√	√	√	√	√	√	8
Chile	√	√		√		√	√		5
China	√	√	√	√	√	√	√		7
Germany	√	√	√		√	√	√		6
Israel	√	√	√		√	√			5
Italy	√	√		√		√	√		5
Japan	√	√	√	√					4
Mexico	√	√	√			√	√		5
Portugal	√	√	√		√		√		5
Spain	√	√	√	√	√	√	√		7
United Kingdom	√	√	√	√	√	√	√		7
United States	√	√		√			√		4
Sum	15	15	12	10	8	12	13	2	

Source: Prepared by the author.

other criteria for specific activities. For instance, Canada establishes some rules to fly a UAV, such as: in case between 14-16 years, the pilot get the basic license and it is forbidden to fly over inhabited areas, however over 16, pilot can get advanced licenses and they allow one to fly over inhabited areas (over 30 meters). Additional requirements include the UAV registration, altitude limitation of 122 meters, 5.6 km of distance from airports, far from other aicrafts and the application of penalties, which include fines and jail time.

Other countries, such as India, regulate the national rules according to the Directorate General of Civil Aviation (GCA). GCA presents manuals and procedures to several tasks, including a specific procedure and training manual for medical applications. India establishes a required minimum of 16 years old to pilot UAVs up to 250g, and over 18 to pilot UAVs over 250g. The pilot is also required to get license and its UAV registration. It is also forbidden to fly over crowed places and close to airports. On the other hand, United Kingdom establishes 18 years as the required minimum age to pilot a UAV and an insurance coverage needs to be paid by the candidate. In addition, the UAVs must fly at least 50m over an inhabited area and 5km away from airports. In Turkey, the pilots are classified into three categories: 12 years old to pilot a UAV up to 4kg, 15 years old required for UAVs weighting up to 25kg and 18 years to UAVs ranging from 25 to 150kg. Likewise United Kingdom, the pilots need to get licenses and insurance coverage,

and these vehicles must fly 50 meters over an inhabited area and 5km away from airports (BETÉ *et al.*, 2021).

3.3.2 Sensitivity to vibration and changes in temperature

The rapid advance of aerial vehicle technology and decreasing of costs have lead to an increased use of UAVs in the medical field. However, different medical products are sensitive to vibration, which can compromise the product integrity during the transportation. Vaccines, antimalarials and blood products are a few example of sensitive medicines to spikes in temperature, humidity and vibration. For instance, antivenom injection based on antibodies can be damaged if they are dropped by UAVs. Complications can be caused to the patients if the stability of active molecules has been compromised (ROYALL; COURTNEY, 2019a). In this sense, several studies have been done to predicting safe flight time and range, monitoring the on-board conditions and testing the medicine quality during and post flight missions.

Amukele *et al.* (2017a) evaluate the use of UAVs to deliver red blood cells. This recent transport method is constantly evaluated to investigate the adverse effects on the payload integrity due to changes in air pressure and temperature as well as sudden accelerations and deceleration during the flight. Blood is well known as a sensitive medical product, which can hemolyze through external forces and vibrations, losing its properties. Samples of blood have been placed in a cooler, which is attached to the UAV, to assess stability of blood products over a 25 minutes of flight. Amukele *et al.* (2017b) have assessed the feasibility of the transported supplies, such as biological samples, over long flights at an ambient temperature of 32°C and low humidity in outdoor conditions. Similarly, a UAV with an attached cooling device was designed to isolate the medical payload from environmental disturbances and a foam-lined barrier was placed on the bottom of the fuselage to attenuate the transference of vibration to the payload. The experiments concluded that the transportation of laboratory samples by small UAVs over a long flight did not affect the stability of 90% of its medication drugs. However, some components, such as glucose and potassium, which were time and temperature-sensitive, required good pre-planning and stringent environmental controls to ensure reliable results.

Faramondi *et al.* (2020) use a conventional commercial quadrotor for experimental analysis, and a compartment is attached to the bottom of its frame to carry the payload at the desired temperature. Six tests are performed to analyze the quality of the blood before and after transportation; one of these tests shows a slight degradation in enzymatic

activity. Similarly, the risk of deterioration in blood quality, caused by external forces and vibration during a quadrotor flight is also addressed. This deterioration is known as hemolyze, in which the blood cannot be used for transfusion. To evaluate the properties of the blood, an enzyme (LD - Lactate Dehydrogenase) from a regular blood sample is compared to that samples transported by the UAV. These comparisons are performed in laboratory and indicate a significant deviation in LD levels.

Johannessen *et al.* (2021) investigate the effects of turbulence on medical product transported by a UAV. A shaker is used to simulate turbulence forces, with frequency ranging from 5 to 200 Hz, to test the stability of blood samples under high vibration amplitudes. The shaker settings are based on data collected by flights of a DJI Matrice 600 UAV. Most of blood samples demonstrated little vulnerability to turbulence, but the authors noted that the plasma samples may be significantly influenced by different vibration intensities. Yakushiji *et al.* (2021) investigate the feasibility of UAVs to transport blood samples anywhere in Japan, including remote islands. Electronic watch and vibration loggers have been chosen to assess the changes in temperature and vibration during the uncrewed helicopter's flight. There is no substantial deviation of the required temperature over the flight. However, the vibration amplitudes are greater than those of an automobile.

Beck *et al.* (2020) study the potential risks, rewards, impacts of transporting adrenaline auto-injector by drones. Anaphylaxis is a rapid and serious systemic allergic reaction triggered by food, medication or insect stings. Adrenaline is a very effective medication for anaphylaxis treatment with the advantage of auto-injector type. Since Anaphylaxis can become deadly in less than 15 minutes without correct treatment, the drone delivery becomes an interesting alternative to emergency service. First, the medical good is subjected to independently 30 minutes of vibration (ranging from 5 to 13.13 Hz) and at different temperatures (4-65 °). Then, a commercial drone is used to assess the adrenaline stability over different phases of a flight. Both the indoor and outdoor texts have shown there is no significant changes in adrenaline concentration or composition, allowing to use safely the drones for this kind of medicine.

In healthcare, the delivery time of several medical products, especially organs, blood and life-saving medicines is crucial. In the United States, approximately 20% of the available kidneys are discarded because of the inability to organize their transplantation within the required time limitation. Scalea *et al.* (2018) have investigated the use of a commercial drone for kidney transportation over short distances. A kidney is shipped in a cylindrical plastic container, and further attached vertically to the body of a drone.

The temperatures, pressure changes, and levels of vibration are evaluated to verify any possible damages or decrease of kidney quality resulting from drone flight. A number of landings, take-offs, and high-acceleration missions are carried out to evaluate how they can affect the parameters experienced by the payload, such as pressures, vibrations and temperatures that can damage fragile human tissues.

Hii, Courtney and Royall (2019) address the impact on the quality of medicines when they are transported by a quadrotor . During a conventional flight, vibration frequencies caused by UAVs components range from 0.1 to 3.4 Hz, which can affect the transported payloads. Moreover, when insulin is exposed to high temperatures and vibration, this perishable life-saving medicine can easily deteriorate, causing its irreversible aggregation, which leads to its inactivation. Following pharmaceutical procedures, temperature and vibration tests were performed to investigate the impact of their parameters on insulin quality during UAV flights. In the laboratory, using controlled conditions, insulin was evaluated for different temperatures (-20 to 40°C) and frequencies (0 to 40 Hz), and results have shown that the quality was preserved. However, the insulin must be transported by different commercial drones in specific environmental conditions to gather additional evidence of its post-transport safety.

Kozioł and Sobczyk (2022) have shown the efficiency of UAVs for biological samples transportation. The analyzed samples demonstrate positive results in short flights, however, other ones such as glucose and potassium have presented changes due to the temperature difference. Royall and Courtney (2019b) address that antivenom injections based on antibodies are also sensitive pharmaceuticals products. Complications to the patient's conditions can be observed if the active molecules stability has been compromised. Vaccines and antimalarial products are also sensitive to spikes in temperature, humidity and vibration, which require special treatment and controlled flight procedures. Table 6 presents the vibration level and temperature range used to investigate the medicine's stability.

Table 6 – Vibration level and temperature range evaluated in the literature

Reference	Item Type	Frequency	Temperature
Amukele *et al.* (2017a)	Blood samples	Not Mentioned	0 - 29.5 °C
Johannessen *et al.* (2021)	Blood samples	5 - 200 Hz	Not Mentioned
Yakushiji *et al.* (2021)	Blood samples	0 - 60 Hz	2 - 10 °C
Beck *et al.* (2020)	Adrenaline	5-13.3 Hz	10.7 - 60 °C
Scalea *et al.* (2018)	Human organ	0.5 - 2 g	Not Mentioned
Hii, Courtney and Royall (2019)	Insulin	0-40 Hz	-20 - 40 °C

Source: Prepared by the author.

3.3.3 Future Opportunities

Unmanned aerial vehicles are seen as a promising alternative to the medical delivery, since the UAV employment can reduce time, decrease costs, improve the work quality and especially save human lives. However, several technological shortcomings are currently studied to integrate UAVs into health care systems, including the battery life, flight endurance and current legislation. Typical UAVs can normally carry an average payload up to 2 kg and fly over 1 hour, which constraints their use when a high payload capacity is required and over longer distances. Beyond these operational limitations, the current national legislation allows one the UAVs to fly only over specific areas, which restrict their operations worldwide. The constant technological development aims to integrate the UAVs into health care system, improving their functionally and surpassing current limitations regarding infrastructure and high costs of service.

The integration of UAVs into health care system continue to highlight their main advantages, such as the delivery of blood products, insulin, organs and other biological samples, the ability to assist mass disasters, and also to guarantee a more dynamic alternative for emergency medicine in remote areas. Different applications have been studied and some of them are already in initial stages of operational tests worldwide. Minimizing the time of different and greater quantities of medical products over long distances is even more advantageous in comparison to the conventional road transportation. Considering the balance between weak and strong points, there are different aspects involved for improving and increasing the possibilities.

The use of multiple UAVs in formation is an alternative to deliver the equivalent of product in comparison single ground vehicle. A collaborative system of multi trucks and UAVs can then emerge as an alternative to medical delivery in remote areas and closed communities. Multiple UAVs can be carried by each truck to perform delivery in parallel, thereby improving the distribution efficiency. Lin *et al.* (2022) summarize the main advantages of this type of cooperation: the truck can storage and transport different items (even those that requires controlled temperature) and the truck can be used as alternative spots for charging or replacing the UAVs batteries, which can extend the flight duration.

The battery consumption of UAVs is another critical shortcoming that limits their flight over long distances. However, the integration of solar panels on UAVs represents a potential solution to overcome this challenge. Besides its potential for increasing substantially the flight endurance, solar energy is a renewable energy, i.e. not pollutant,

relatively unlimited and less costly. Hrovatin and Zemva (2021) perform several aerial mapping mission to investigate the energy efficiency of a UAV. Flexible solar modules are then used to cover part of the UAV wings resulting in an important increase of the flight endurance by up to 21.25%.

The increased development of innovative smart city involves strategies to fully integrate the information and communication technologies regarding UAVs and logistic supply chain. The adoption of UAVs to automate inventory management can be seen as the key element to improve this task. Inventory management presents several advantages such as a high time-consuming, high costs operation with low turnouts, and it can lead to worker's injuries due to the weight of goods and height of racks. Then, UAVs and unmanned ground vehicles (UGV) can be incorporated for a fully automated inventory management system, where UGV is responsible to select the appropriate package and the UAV to transport to the final destination (GUPTA *et al.*, 2021). Therefore, an efficient warehouse system leads to timely dispatch of medical products, which may optimize efficiently the logistic supply chain.

The payload capacity, weather conditions, flight distance are also attributes that define the type of UAV suitable for each desired application. Dampers and foam layers can also be required onboard because there are medical products sensitive to spike of temperature, vibration and changes in pressure. The development of isolated compartments and more efficient UAVs allows to safely transport medical products over long distances. Standard procedures of packaging, loading and unloading can also be evaluated to ensure that the medicines quality and integrity are maintained throughout the supply chain path mainly because the medical products must be protected against breakage and adulteration. In addition, practical applications can require to regularly calibrate different sensors (such as temperature monitoring, vibration, pressure) involved in the operations.

UAVs represent a promising technology to improve the patient survival, life quality, in particular for those in areas with low infrastructure, remote areas or low-income countries. Partnerships among governments, academic and private sectors have been formed allowing the evaluation of specific needs of each region. In comparison to conventional ground transportation, lower costs, higher speed, and dynamism, make the UAVs a feasible solution to optimize the medical field supply chain. The constant development of UAV designs will lead to new technologies with reduced costs, longer-life batteries, and increased maximum capacity, allowing the use of UAVs expands considerably in medical applications.

3.4   Final Remarks

The delivery of medical and hospital products have been realized exclusively by road transportation, mainly by trucks and cars. However, with the rapid advance in technology related to the aeronautical field, unmanned aerial vehicles have been employed in different tasks, and they provide numerous advantages to the healthcare logistics, such as relative reduced costs. On the other hand, these are important challenges to overcome, such as those involving flight duration and safety, the effects of turbulence on the flight and others.

In particular, the vibration analysis is an important topic for different applications involving products transportation by UAVs. Especially in medical and hospital products transportation, the presence of vibrations can impact negatively the payloads. Despite several advantages of using UAVs as potential solution to overcome geographical and economical challenges, vaccines, antimalarial and blood products are a few examples of sensitive medicines to spikes in temperature, humidity and vibration. Thus, an increasing number of works in the literature has investigated the feasibility of using commercial UAVs to transport this type of products. Therefore, an efficient transportation system can guarantee an improvement of pharmaceutical products delivery and a lower rate of organs and medicines that have to be disposed.

4 QUADROTOR WITH A VERTICAL VIBRATING PAYLOAD

This chapter 4.1 presents a modeling of a 7 DOF dynamic model for a quadrotor using elastic attachment. The payload can vibrate only in the vertical direction due to the structural characteristics and the model is an interesting approach to investigate the dynamics of a cruise flight. Then, the payload vibration analysis is presented in Sections 4.2 and 4.3, respectively for two strategies of control. The first strategy is named quasi-open-loop control, and the second one is a closed loop control.

4.1 DYNAMIC MODEL

This section presents a new 7 DOF dynamic model for a quadrotor considering flexible attachment in the vertical direction. In this case, the payload only translates vertically, since the lateral stiffness are considered much higher than the vertical component, and it is assumed that they can be neglected.

4.1.1 Mathematical model of a quadrotor

Conventional dynamic modeling of a quadrotor can be found in the literature, as shown by (FOSSEN, 1994; KIM; KANG; PARK, 2009; SHEN; FAN; WANG, 2018) and others. Usually, the quadrotor is assumed to have a rigid body and symmetrical about the body-frame, and the origin of a rigid-frame coordinate system coincides with the center of gravity (CoG) of the quadrotor. The quadrotor is composed of four rotors fixed in a cross configuration, the propellers are assumed rigid and the thrust forces are proportional to the square of propeller velocity. The aerodynamics effects are neglected for this modeling, such as previously introduced by (CASTILLO-ZAMORA *et al.*, 2018; ZHENG; XIONG; LUO, 2014) Figure 24 shows the coordinates system, in which $(X_B, \ Y_B, \ Z_B)$ is the

body-fixed reference and $(X_I,\ Y_I,\ Z_I)$ is the inertial reference [1] coordinate system.

Figure 24 – Schematic illustration of a quadrotor, showing the body-fixed and inertial coordinates systems, where inertial reference (solid black line), body-fixed reference (solid red line) and forces created by each rotor (F_i).
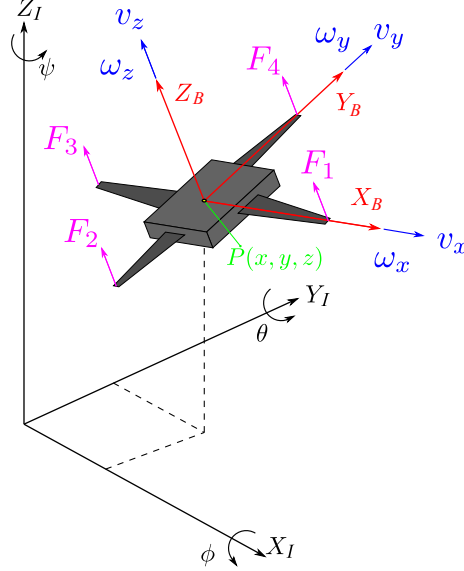
Source: Geronel, Dowell and Bueno (2021).

The quadrotor position $P(x,y,z)$ and orientation (ϕ,θ,ψ) are described relative to inertial reference frame, while its linear (v_x,v_y,v_z) and angular $(\omega_x,\omega_y,\omega_z)$ velocities are written in body-fixed frame. In the presence of power applied to each rotor of the quadrotor, it can generate thrusts and torques, which are respectively denoted by F_i and M_i, $i=1,...,4$. The four motors of the quadrotor rotate with angular velocity to generate a vertical force, that is defined by a constant multiplied by the squared propeller rotation velocity, i.e. $F_i = k_t \Omega_i^2$. The combination of these four individual forces results in thrust, defined by $F_{ti} = \sum_{i=1}^{4} F_i$. The torques are expressed by the corresponding forces multiplied by a distance between the motor and CoG (l), leading to $\tau_i = l \sum_{i=1}^{4} F_i$.

The angular velocity of left, back, right and front propellers are denoted by Ω_1, Ω_2, Ω_3 and Ω_4, respectively. Therefore, roll, pitch and yaw angles are represented by ϕ, θ and ψ, respectively. The roll motion is obtained by the difference between Ω_2 and Ω_4. Similarly, the difference between Ω_1 and Ω_3 generates the pitch motion. The yaw motion ψ is obtained if the algebraic sum of moments produced by the four rotors is not zero, i.e., when there is the difference in angular velocities between two opposite pairs of rotors. Figure 25 shows the angular velocities and forces on each motor, whereas Table 7 shows the combination of the rotors velocities and their respective direction of motion.

---

[1]Due to the dimensions of typical UAVs, the accelerations of a point on the surface of the Earth can be neglected and the ground-fixed reference frame is considered to be inertial, as noted by Kim, Kang and Park (2009).

Figure 25 – Forces (F_i) and angular velocities (Ω_i) created by a quadrotor.
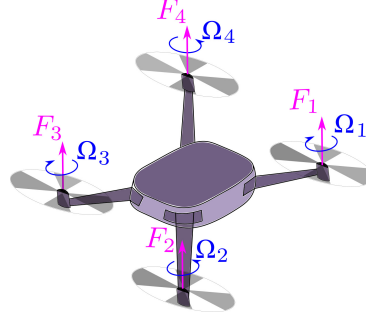
Source: Prepared by the author.

Table 7 – Directions of motion due to the rotor velocities, where ↑ denotes a relative increment and ↓ a relative decrement of each respective rotor velocity. – indicates that the rotor velocity is kept constant.

Direction of motion	Rotor 1	Rotor 2	Rotor 3	Rotor 4
Upward	↑	↑	↑	↑
Roll (ϕ)	–	↑	–	↓
Pitch (θ)	↓	–	↑	–
Yaw (ψ)	↓	↑	↓	↑

Source: Geronel, Dowell and Bueno (2021).

The equation of motion for a dynamic system can be calculated using two widely known methods: Newton-Euler and Euler-Lagrange. Newton-Euler method is chosen, since the matrices are easier and more intuitive to be represented throughout the new UAV configurations. The equation of motion can be derived with respect to the body-fixed frame or with respect to the inertial reference frame. The dynamic equation of motion in the body-fixed reference is given by (KIM; KANG; PARK, 2009) as $\mathbf{M}_{q_B}\dot{\boldsymbol{\nu}}_{q_B} + \mathbf{C}_{q_B}(\boldsymbol{\nu}_{q_B})\boldsymbol{\nu}_{q_B} + \mathbf{g}_{q_B} = \boldsymbol{\tau}_{q_B}$, where $\mathbf{M}_{q_B}$ is the matrix of inertia, $\mathbf{C}_{q_B}(\boldsymbol{\nu}_{q_B})$ is the matrix of Coriolis, $\boldsymbol{\tau}_{q_B}$ is the control input vector, and $\mathbf{g}_{q_B} = mg\{-s\theta \quad c\theta s\phi \quad c\theta c\phi \quad 0 \quad 0 \quad 0\}^T$ is the vector of gravity effect and $\boldsymbol{\nu}_{q_B} = \{v_x \quad v_y \quad v_z \quad \omega_x \quad \omega_y \quad \omega_z\}^T$ is the velocity vector. The equation of motion can be also written in the inertial reference as

$$\mathbf{M}_{q_I}\ddot{\boldsymbol{\eta}}_{q_I} + \mathbf{C}_{q_I}\dot{\boldsymbol{\eta}}_{q_I} + \mathbf{g}_{q_I} = \boldsymbol{\tau}_{q_I} \tag{3}$$

where g is the acceleration due to gravity and the generalized coordinates vector is defined by $\boldsymbol{\eta}_{q_I} = \{x \quad y \quad z \quad \phi \quad \theta \quad \psi\}^T$. For notation simplicity, their main matrices are represented

in the body-fixed frame, yielding the following Eqs. (4)

$$
\begin{aligned}
\mathbf{M}_{q_I} &= \mathbf{I}_{6\times6} \\
\mathbf{C}_{q_I} &= \mathbf{J}_q \mathbf{M}_{q_B}^{-1} \mathbf{C}_{q_B} \mathbf{J}_q^{-1} - \dot{\mathbf{J}}_q \mathbf{J}_q^{-1} \\
\mathbf{g}_{q_I} &= \mathbf{J}_q \mathbf{M}_{q_B}^{-1} \mathbf{g}_{q_B} \\
\boldsymbol{\tau}_{q_I} &= \mathbf{J}_q \mathbf{M}_{q_B}^{-1} \boldsymbol{\tau}_{q_B}
\end{aligned}
\tag{4}
$$

where $\mathbf{I}_{6\times6}$ is a 6×6 Identity matrix. The matrix of inertia is defined as $\mathbf{M}_{q_B} = diag(m, m, m, I_x, I_y, I_z)$, where m is the quadrotor mass and I_j is the moments of inertia along x, y and z axes. The Coriolis matrix is expresses as

$$
\mathbf{C}_{q_{B1}} = \begin{bmatrix} m\mathbf{C}_{q_{B1}} & \mathbf{0}_{3\times3} \\ \mathbf{0}_{3\times3} & \mathbf{C}_{q_{B2}} \end{bmatrix}
\tag{5}
$$

where

$$
\mathbf{C}_{q_{B1}} = \begin{bmatrix} 0 & -\omega_z & \omega_y \\ \omega_z & 0 & -\omega_x \\ -\omega_y & \omega_x & 0 \end{bmatrix}, \qquad
\mathbf{C}_{q_{B2}} = \begin{bmatrix} 0 & 0 & I_{zy}\omega_y \\ I_{xz}\omega_z & 0 & 0 \\ 0 & I_{yx}\omega_x & 0 \end{bmatrix}
\tag{6}
$$

where the moments of inertia of the Coriolis matrix are defined as $I_{zy} = (I_z - I_y)$, $I_{xz} = (I_x - I_z)$ and $I_{yx} = (I_y - I_x)$, and $diag(.)$ indicates a diagonal matrix. The transformation matrix, between the inertial and body-fixed reference frames ($\dot{\boldsymbol{\eta}}_{q_I} = \mathbf{J}_q \boldsymbol{\nu}_{q_B}$), is represented with the following Eq. (7)

$$
\mathbf{J}_q = \begin{bmatrix} \mathbf{J}_{q_1} & \mathbf{0}_{3\times3} \\ \mathbf{0}_{3\times3} & \mathbf{J}_{q_2} \end{bmatrix}
\tag{7}
$$

where $\mathbf{J}_{q_1}$ is obtained through the multiplication of three consecutive matrices $\mathbf{R}_{z,\psi}$, $\mathbf{R}_{y,\theta}$ and $\mathbf{R}_{x,\phi}$, i.e. $\mathbf{J}_{q_1} = \mathbf{R}_{z,\psi} \mathbf{R}_{y,\theta} \mathbf{R}_{x,\phi}$. These matrices are respectively defined as follows

$$
\mathbf{R}_{z,\psi} = \begin{bmatrix} c\psi & s\psi & 0 \\ -s\psi & c\psi & 0 \\ 0 & 0 & 1 \end{bmatrix}, \qquad
\mathbf{R}_{y,\theta} = \begin{bmatrix} c\theta & 0 & -s\theta \\ 0 & 1 & 0 \\ s\theta & 0 & c\theta \end{bmatrix}, \qquad
\mathbf{R}_{x,\phi} = \begin{bmatrix} 1 & 0 & 0 \\ 0 & c\phi & s\phi \\ 0 & -s\phi & c\phi \end{bmatrix}
\tag{8}
$$

The relation between the Euler's derivative angles in the inertial reference frame and quadrotors's angular velocity expressed in the body-fixed frame is used to compute the second transformation matrix (matrix of Euler), and it is expressed by

$$
\begin{Bmatrix} \dot{\phi} \\ \dot{\theta} \\ \dot{\psi} \end{Bmatrix} = \begin{bmatrix} 1 & s\phi t\theta & c\phi t\theta \\ 0 & c\phi & -s\phi \\ 0 & s\phi/c\theta & c\phi/c\theta \end{bmatrix} \begin{Bmatrix} \omega_x \\ \omega_y \\ \omega_z \end{Bmatrix}
\tag{9}
$$

The multiplication of matrices in Eq. (8) and the matrix in Eq. (9) lead to the transformation matrices $\mathbf{J}_{q_1}$ and $\mathbf{J}_{q_2}$, and they are defined by

$$\mathbf{J}_{q_1} = \begin{bmatrix} c\psi c\theta & s\phi s\theta c\psi - c\phi s\psi & c\phi s\theta c\psi + s\psi s\phi \\ s\psi c\theta & s\phi s\theta s\psi + c\phi c\psi & c\phi s\theta s\psi - s\phi c\psi \\ -s\theta & s\phi c\theta & c\phi c\theta \end{bmatrix}, \qquad \mathbf{J}_{q_2} = \begin{bmatrix} 1 & s\phi t\theta & c\phi t\theta \\ 0 & c\phi & -s\phi \\ 0 & s\phi/c\theta & c\phi/c\theta \end{bmatrix} \quad (10)$$

where $s(.)$, $c(.)$ and $t(.)$ indicate respectively the sine, cosine and tangent functions, and $\dot{\mathbf{J}}_q$ represents the transformation matrix derivative with respect to time. The control input vector is given by $\boldsymbol{\tau}_{q_B} = \{0\ \ 0\ \ U_1\ \ U_2\ \ U_3\ \ U_4\}^T$.

4.1.2 Dynamic model of a quadrotor with an attached mass

In contrast to the conventional model, a payload is attached directly to the quadrotor body. Figure 26 depicts the coupled system, in which the payload is attached to the quadrotor, such that the quadrotor dynamics is transmitted directly to its payload. The container is represented by the green box, whereas the transported mass is placed inside it. The introduced dynamic model is used to investigate the effects of vibrations on the payload.

Figure 26 – Schematic illustration of a quadrotor with a mass m and its payload with a mass m_p (green box attached to the aerial vehicle). The zoomed view indicates the attachment system k_p.
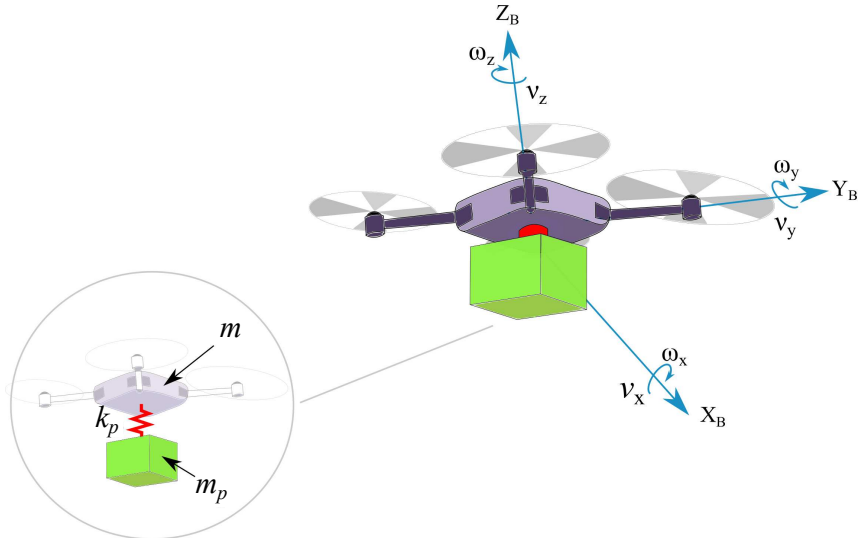
Source: Prepared by the author.

Note the stiffness coefficients are placed to correspond to the vertical DOFs of the quadrotor and its payload, and it is assumed that the lateral displacement of m_p is such that $x_p = x$ and $y_p = y$ due to k_{xp} and $k_{yp} >> k_{zp}$. Then, the velocities and accelerations of

m_p in both x and y directions are considered equal to the quadrotor. An unidirectional spring-mass system can be used to represent the resulting equivalent system, as depicted in Figure 27.

Figure 27 – Representation of a mass-spring.
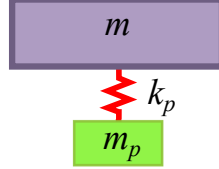
Source: Prepared by the author.

where m_p is the mass of the payload, and k_p represents the attachment stiffness oriented in the vertical direction (connecting the states z and z_p). In comparison to the equation of motion with no payload (Eq. (3)), an additional elastic force is created ($\mathbf{F}_k$), yielding

$$\mathbf{F}_k = \begin{bmatrix} k_p & -k_p \\ -k_p & k_p \end{bmatrix} \begin{Bmatrix} z \\ z_p \end{Bmatrix} \tag{11}$$

where this elastic force vector ($\mathbf{F}_k$) can be represented by a stiffness matrix multiplied by the generalized coordinate vector ($\mathbf{K}_{qp_I}\boldsymbol{\eta}_{qp_I}$). The equation of motion of the resulting coupled system is then presented in Eq. (12)

$$\mathbf{M}_{qp_I}\ddot{\boldsymbol{\eta}}_{qp_I} + \mathbf{C}_{qp_I}\dot{\boldsymbol{\eta}}_{qp_I} + \mathbf{g}_{qp_I} + \mathbf{K}_{qp_I}\boldsymbol{\eta}_{qp_I} = \boldsymbol{\tau}_{qp_I} + \mathbf{F}_d \tag{12}$$

where $\mathbf{M}_{qp_I}$ is the matrix of inertia, $\mathbf{C}_{qp_I}$ represents the Coriolis matrix, $\mathbf{g}_{qp_I}$ is the gravitational vector, $\mathbf{K}_{qp_I}$ is the stiffness matrix, $\boldsymbol{\tau}_{qp_I}$ denotes the control input, and $\mathbf{F}_d$ is the gust vector. Regarding Eq (12), all matrices present a (7×7) dimension, whereas the dimension of vectors corresponds to (7×1). Similarly to Eq. (4), the main matrices of Eq. (12) can be rewritten by

$$\begin{aligned} \mathbf{M}_{qp_I} &= \mathbf{I}_{7\times7} \\ \mathbf{C}_{qp_I} &= \mathbf{J}_{qp}\mathbf{M}_{qp_B}^{-1}\mathbf{C}_{qp_B}\mathbf{J}_{qp}^{-1} - \dot{\mathbf{J}}_{qp}\mathbf{J}_{qp}^{-1} \\ \mathbf{g}_{qp_I} &= \mathbf{J}_{qp}\mathbf{M}_{qp_B}^{-1}\mathbf{g}_{qp_B} \\ \mathbf{K}_{qp_I} &= \mathbf{J}_{qp}\mathbf{M}_{qp_B}^{-1}\mathbf{K}_{qp_B} \\ \boldsymbol{\tau}_{qp_I} &= \mathbf{J}_{qp}\mathbf{M}_{qp_B}^{-1}\boldsymbol{\tau}_{qp_B} \end{aligned} \tag{13}$$

where $\mathbf{M}_{qp_B} = diag(m+m_p, m+m_p, m, I_x + I_x^p, I_y + I_y^p, I_z + I_z^p, m_p)$, while the Coriolis matrix

is represented as

$$\mathbf{C}_{qp_B} = \begin{bmatrix} \mathbf{C}_{qp_{B1}} & \mathbf{0}_{3\times3} & \mathbf{C}_{qp_{B0}}^T \\ \mathbf{0}_{3\times3} & \mathbf{C}_{qp_{B2}} & \mathbf{0}_{3\times1} \\ \mathbf{C}_{qp_{B0}} & \mathbf{0}_{3\times1} & 0 \end{bmatrix} \tag{14}$$

where

$$\mathbf{C}_{qp_{B1}} = \begin{bmatrix} 0 & -(m+m_p)\omega_z & m\omega_y \\ (m+m_p)\omega_z & 0 & -m\omega_x \\ -m\omega_y & m\omega_x & 0 \end{bmatrix}, \qquad \mathbf{C}_{qp_{B2}} = \begin{bmatrix} 0 & 0 & I_1\omega_y \\ I_2\omega_z & 0 & 0 \\ 0 & I_3\omega_x & 0 \end{bmatrix} \tag{15}$$

where $\mathbf{C}_{qp_{B0}} = \{-m_p\omega_y \quad m_p\omega_x \quad 0\}$, I_1, I_2 and I_3 are the moments of inertia along the x, y, z axes respectively, and they are defined as $I_1 = (I_{zy} + I_{zy}^p)$, $I_2 = (I_{xz} + I_{xz}^p)$ and $I_3 = (I_{yx} + I_{yx}^p)$, respectively, where I_j is related to the quadrotor and I_j^p refers to the coupled system moments of inertia ($j = x, y, z$). In addition, the gravitational vector is given by $\mathbf{g}_{qp_B} = \{\mathbf{g}_{q_B} \quad m_p g c\theta c\phi\}^T$, whereas the 7 DOF generalized coordinate displacement vector is given by $\boldsymbol{\eta}_{qp_I} = \{\boldsymbol{\eta}_{q_I} \quad z_p\}^T$. The 7 DOF transformation matrix $\mathbf{J}_{qp}$ is defined as

$$\mathbf{J}_{qp} = \begin{bmatrix} \mathbf{J}_q & \mathbf{0}_{6\times1} \\ \mathbf{j}_n & c\theta c\phi \end{bmatrix} \tag{16}$$

where $\mathbf{j}_n = \{-s\theta \quad c\theta s\phi \quad 0 \quad 0 \quad 0 \quad 0\}$, and the control input is represented by $\boldsymbol{\tau}_{qp_B} = \{\boldsymbol{\tau}_{q_B}^T \quad 0\}^T$. The unidirectional mass-spring assumed to represent the elastic attachment (Eq. (11)) allows to write the stiffness matrix $\mathbf{K}_{qp_B}$ with the following Eq. (17)

$$\mathbf{K}_{qp_B} = \begin{bmatrix} \mathbf{0}_{7\times2} & \mathbf{k}_p & \mathbf{0}_{7\times3} & -\mathbf{k}_p \end{bmatrix}^T \tag{17}$$

where $\mathbf{k}_p = \{0 \quad 0 \quad k_p \quad 0 \quad 0 \quad 0 \quad -k_p\}^T$ and $\mathbf{0}_{a\times b}$ are zero matrices with a rows and b columns. The second order differential equation of motion (Eq. (12)) is represented in state-space form is given by

$$\dot{\boldsymbol{x}}_{qp}(t) = \mathbf{A}_{qp}\boldsymbol{x}_{qp}(t) + \mathbf{B}_{qp}\mathbf{u}_{qp}(t) + \mathbf{X}_{qp} \tag{18}$$

where $\boldsymbol{x}_{qp} = \left\{ \dot{\boldsymbol{\eta}}_{qp_I}^T \quad \boldsymbol{\eta}_{qp_I}^T \right\}^T$ is the state vector, $\mathbf{u}_{qp}(t) = \left\{ \boldsymbol{\tau}_{qp_I}^T \quad \mathbf{0}_{7\times1} \right\}^T$ is the input vector, and $\mathbf{X}_{gp} = \left\{ -(\mathbf{M}_{qp_I}^{-1}\mathbf{g}_{qp_I})^T \quad \mathbf{0}_{7\times1} \right\}^T$ is the gravitational vector. The dynamic ($\mathbf{A}_{qp}$) and input ($\mathbf{B}_{qp}$) matrices are represented as follows

$$\mathbf{A}_{qp} = \begin{bmatrix} -\mathbf{M}_{qp_I}^{-1}\mathbf{C}_{qp_I} & -\mathbf{M}_{qp_I}^{-1}\mathbf{K}_{qp_I} \\ \mathbf{I}_{7\times7} & \mathbf{0}_{7\times7} \end{bmatrix} \qquad\qquad \mathbf{B}_{qp} = \begin{bmatrix} \mathbf{M}_{qp_I}^{-1} \\ \mathbf{0}_{7\times7} \end{bmatrix} \tag{19}$$

4.2 NON-AUTONOMOUS FLIGHT

Non-autonomous flight corresponds to the quadrotor control from pilot inputs. This is usually done by using a hand-held device that allows the pilot to maneuver the quadrotor. The pilot considers a visual line or a visual system to know the position of the aerial vehicle, and this qualitative characteristics is named quasi-open-loop control strategy. Then a controller is defined based on pre-determined forces to create the input control. The forces are defined for each particular trajectory based on the combination of the rotors angular velocities.

This communication between the pilot and control device allows the quadrotor flight to be achieved by a different combination of its four angular velocities. The combination of angular velocities can be associated with the control input, and then rewritten in forces notation, as $\boldsymbol{\tau} = \{0 \ 0 \ U_1 \ U_2 \ U_3 \ U_4 \ 0\}^T$, such as:

$$\begin{Bmatrix} U_1 \\ U_2 \\ U_3 \\ U_4 \end{Bmatrix} = \begin{bmatrix} 1 & 1 & 1 & 1 \\ 0 & -l & 0 & l \\ -l & 0 & l & 0 \\ -\lambda & \lambda & -\lambda & \lambda \end{bmatrix} \begin{Bmatrix} \bar{F}_1 \\ \bar{F}_2 \\ \bar{F}_3 \\ \bar{F}_4 \end{Bmatrix} \tag{20}$$

where l is the length between the rotor and the quadrotor center of gravity and λ is the relation between torque and generated force. The pilot inputs is introduced by defining the values of F_i over time, according to each phase of flight. However, in non-dimensional form each i-th force is proportional to the quadrotor total weight, i.e., $F_i = (m + m_p)g\bar{F}_i$, which implies in practice to define each force per unit of weight $\bar{F}_i$. These non-dimensional forces $\bar{F}_i$ $(i = 1, ..., 4)$ are defined by considering the arrangements shown in Table 7.

In addition, the above equation is rewritten in terms of the angle γ_c if the x axis corresponds to the camera placed below the aerial vehicle, as commonly considered by typical commercial UAVs. Then, the following equation is obtained.

$$\begin{Bmatrix} U_1 \\ U_2 \\ U_3 \\ U_4 \end{Bmatrix} = \begin{bmatrix} 1 & 1 & 1 & 1 \\ ls\gamma_c & -ls\gamma_c & -ls\gamma_c & ls\gamma_c \\ -lc\gamma_c & -lc\gamma_c & lc\gamma_c & lc\gamma_c \\ -\lambda & \lambda & -\lambda & \lambda \end{bmatrix} \begin{Bmatrix} \bar{F}_1 \\ \bar{F}_2 \\ \bar{F}_3 \\ \bar{F}_4 \end{Bmatrix} \tag{21}$$

where γ_c indicates the angle between the quadrotor's arms and the coordinate system.

Non-dimensional Equation of Motion

The equation of motion (Eq. (13)) can be conveniently rewritten in a non dimensional form. The approach introduced herein allows one to establish the oscillation frequency f_c of the payload mass during the flight. The first step of the approach is to consider the reference frequency $f_r = \frac{k_p(m+m_p)}{2\pi m m_p}$, which corresponds to the natural frequency of an equivalent mass-spring structural system associated to the quadrotor and its payload. The results from this simple and convenient equation can be compared to each other. In addition, let p_m be a mass ratio $p_m = m_p/m$ and $p_{()} = I_{()}^p/I_{()}$ for x, y or z, introducing the non-dimensional time $\tau_t = t f_r$, the non-dimensional state space representation is given by

$$\dot{\mathbf{x}}_n(\tau_t) = \mathbf{A}_n \mathbf{x}_n(\tau_t) + \mathbf{B}_n \mathbf{u}_n(\tau_t) + \mathbf{X}_n \tag{22}$$

where

$$\mathbf{A}_n = \begin{bmatrix} -(1/f_r)\mathbf{M}_n^{-1}\mathbf{C}_n & -(1/f_r)^2\mathbf{M}_n^{-1}\mathbf{K}_n \\ \mathbf{I}_{7\times7} & \mathbf{0}_{7\times7} \end{bmatrix} \tag{23}$$

and similar to Eq. (13), the matrices are defined as

$$\mathbf{M}_{n_B} = diag(1 + p_m,\ 1 + p_m,\ 1,\ r_x^2(1 + p_x),\ r_y^2(1 + p_y),\ r_z^2(1 + p_z),\ p_m) \tag{24}$$

$$\mathbf{C}_{n_B} = \begin{bmatrix} 0 & -(1+p_m)\omega_z & \omega_y & 0 & 0 & 0 & p_m\omega_y \\ (1+p_m)\omega_z & 0 & -\omega_x & 0 & 0 & 0 & -p_m\omega_x \\ -\omega_y & \omega_x & 0 & 0 & 0 & 0 & 0 \\ 0 & 0 & 0 & 0 & 0 & r_{zy}\omega_y & 0 \\ 0 & 0 & 0 & r_{xz}\omega_z & 0 & 0 & 0 \\ 0 & 0 & 0 & 0 & r_{yx}\omega_x & 0 & 0 \\ -p_m\omega_y & p_m\omega_x & 0 & 0 & 0 & 0 & 0 \end{bmatrix} \tag{25}$$

where $r_{yx} = r_y^2(1+p_y) - r_x^2(1+p_x)$, $r_{zy} = r_z^2(1+p_z) - r_y^2(1+p_y)$ and $r_{xz} = r_x^2(1+p_x) - r_z^2(1+p_z)$. If $p_x = p_y = p_z \equiv p_I$, then

$$\begin{aligned} r_{yx} &= (r_y^2 - r_x^2)(1 + p_I) \\ r_{zy} &= (r_z^2 - r_y^2)(1 + p_I) \\ r_{xz} &= (r_x^2 - r_z^2)(1 + p_I) \end{aligned} \tag{26}$$

where r_x, r_y and r_z are the radii of gyration, $\mathbf{B}_n = p_n \mathbf{B}_{qp_I}$, $\mathbf{u}_n(\tau_t) \equiv \mathbf{u}_{qp_I}(t)$, $\mathbf{X}_n = p_n \mathbf{X}_{qp_I}$, $\mathbf{x}_n = \{\boldsymbol{\eta}_n'^T \quad \boldsymbol{\eta}_n^T\}^T$, and $p_n = 1/(Hf_r^2)$, where H is a reference height of flight. The non-dimensional displacement vector is $\boldsymbol{\eta}_n = \boldsymbol{\eta}_{qp}/H$ and the time derivative $\frac{d()}{dt}$ is replaced by $\frac{d()}{d\tau_t}$, which allows one to write $\boldsymbol{\eta}_n' = p_n f_r \dot{\boldsymbol{\eta}}_{qp_I}$ and $\boldsymbol{\eta}_n'' = p_n \ddot{\boldsymbol{\eta}}_{qp_I}$. The term $\mathbf{K}_{n_B}$ is given by

$$\mathbf{K}_{n_B} = [\mathbf{0}_{7\times2} \ \ \mathbf{k}_n \ \ \mathbf{0}_{7\times3} \ -\mathbf{k}_n] \tag{27}$$

where $\mathbf{k}_n = \{0 \ \ 0 \ \ k_n \ \ 0 \ \ 0 \ \ 0 \ -k_n\}^T$ and

$$k_n = \frac{p_m f_r^2}{4(1 + p_m)\pi^2} \tag{28}$$

4.2.1   Oscillation Frequency of a Payload Mass

In a mission of transporting a payload mass in a UAV it is desired that each particular aerial vehicle carries a range of masses, i.e., not limiting transport to just a specific mass. On the other hand, the combination of each payload mass m_p and the fixed stiffness k_p implies different oscillation frequencies during the flight. Based on the non-dimensional dynamics introduced in Section 4.2, it is possible to determine the vibrating frequency f of a transported mass fixed on the quadrotor. Let F be the ratio between frequencies f and f_r, the non-dimensional analysis allows one to demonstrate that F can be described by a linear function in terms of the mass ratio, i.e., $F = (c_a p_m + c_l)$. The vibrating frequency is then given by

$$f = (c_a p_m + c_l) f_r \tag{29}$$

The linear function F in terms of p_m is defined using both angular and linear coefficients, c_a and c_l, respectively. The non-dimensional equations introduced in Section 4.2 allows one to determine an approximate frequency f_{ap} considering $c_a = -0.42$ and $c_l = 0.95$, i.e., $f \approx f_{ap} = (-0.42 p_m + 0.95) f_r$. This is a convenient estimate for practical applications in engineering that allows one to determine the frequency of oscillation from the mass of the quadrotor, the payload and the stiffness of fixation without the need of using the complete equation of motion.

The oscillation frequency of the payload mass is investigated considering different trajectories of the quadrotor. The first case exhibits one level of hovering during the flight, meanwhile the second one shows three different levels. The non-dimensionalization allows one to evaluate a general aerial vehicle, making the results independent of a set of physical and geometrical properties. Figure 28 shows the quadrotor non-dimensional

altitude z/H (in Z_I direction) over time τ_t.

Figure 28 – Quadrotor (solid blue line) and payload mass (dashed black line) normalized altitudes for the first flight.
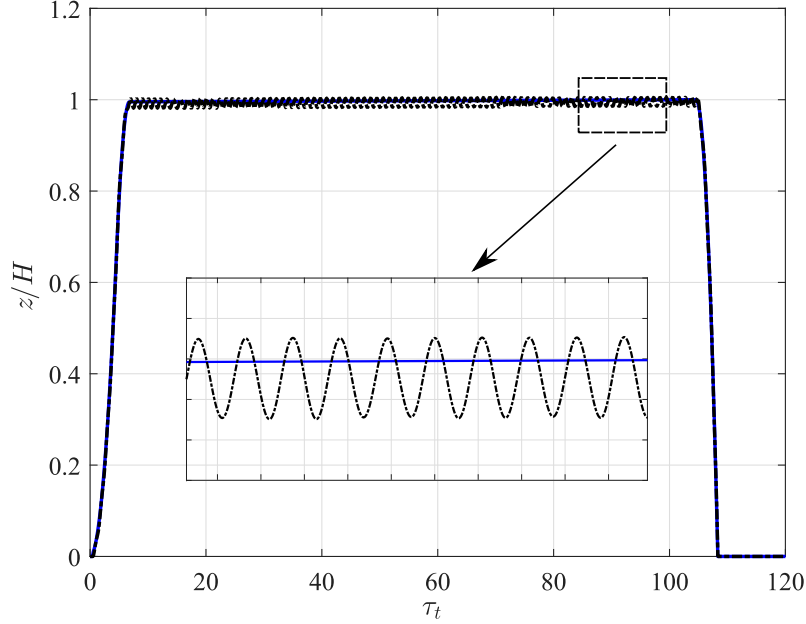
Source: Geronel, Dowell and Bueno (2021).

This first flight exhibits three stages, i.e., take-off, cruise and landing. In the first stage all rotors rotate at the same velocity to get a vertical flight by considering $\bar{F}_i = 0.3(1+p_m)$, $i = 1, ..., 4$. Note that the vertical upward trajectory is obtained when each rotors generates $\bar{F}_i > (m+m_p)g/4$. For the second stage is considered $\bar{F}_1 = \frac{4.95}{4}(1+p_m)$, $\bar{F}_2 = \bar{F}_4 = \frac{5}{4}(1+p_m)$, $\bar{F}_3 = \frac{5.02}{4}(1+p_m)$ and, on the other hand, $\bar{F}_i = 0.2(1+p_m)$ for landing ($i = 1, ..., 4$). This figure shows the quadrotor altitude z/H (continuous line) and z_p/H, which corresponds to the non-dimensional payload mass oscillation (dashed line).

Figure 29 shows the non-dimensional oscillation frequency F for different values of p_m. These results are obtained by integrating Eq. (22) in the time domain, for each particular p_m, using the Runge-Kutta algorithm with time step 2×10^{-4} seconds. The Fourier transform is applied to compute the states in the frequency domain. It is evaluated $m_p \leq \frac{1}{2}m$, and the stiffness k_p are computed to keep fixed the same frequency for all range of p_m. It is separately evaluated three different frequencies, $f_r = 5$ Hz, $f_r = 10$ Hz or $f_r = 20$ Hz, and Figure 30 shows the stiffness for each condition evaluated. In particular for Figure 29 is considered $p_x = p_y = p_z = 0.01$. The solid line in these figures are computed by $f_{ap} = (-0.42p_m + 0.95)f_r$ and the maximum errors observed is lower than 1% in Hertz if $p_m \leq 20\%$, i.e., the payload oscillation frequency can accurately be computed using the proposed approximation if $m_p \leq m/5$. If $p_m > 20\%$ the error arises, but is less than 3.5%

Figure 29 – Non-dimensional oscillation frequency of the payload mass during the flight, where f_r = 5.0 Hz (symbol △), f_r = 10 Hz (symbol ○), f_r = 20 Hz (symbol +) and the approximated oscillation frequency f_{ap} (solid black line) considering $I_{()}^c/I_{()}$ = 0.01.
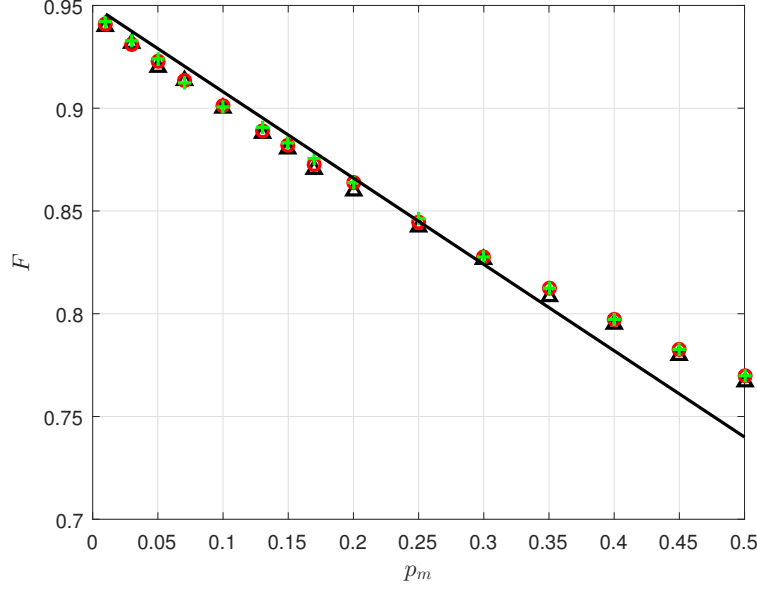
Source: Geronel, Dowell and Bueno (2021).

in the range investigated.

Figure 30 – Normalized stiffness of mass-spring, where f_r = 5.0 Hz (symbol △), f_r = 10 Hz (symbol ○) and f_r = 20 Hz (symbol +).
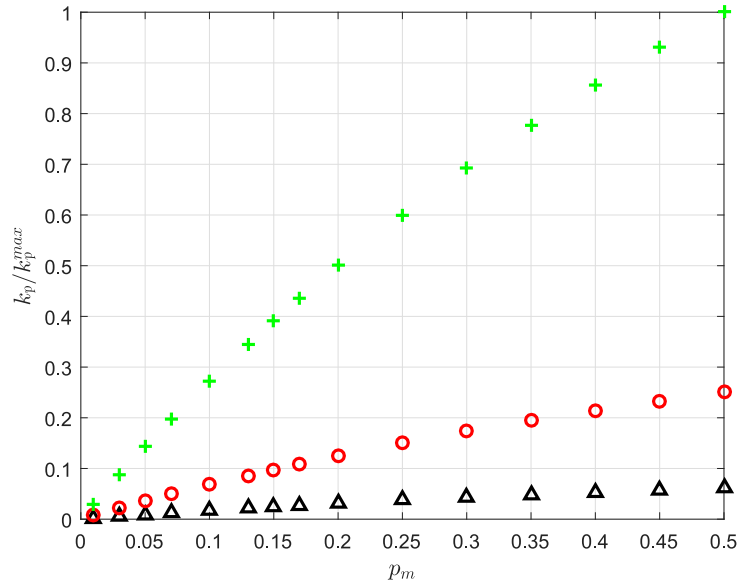
Source: Geronel, Dowell and Bueno (2021).

Figure 31 shows the trajectory of the second flight. The same ratio of inertia is used as in the first flight. It is noted that there is no substantial differences of the oscillation frequency if the total time of flight is considered to compute the spectral

response or, alternatively, a particular time frame for any phase of flight. Figure 32 shows the oscillation frequencies computed through the numerical simulations and by using the proposed expression for its approximation (f_{ap}). It is verified that flights with more transitions of altitude imply oscillation frequencies more different than f_{ap}, in comparison with the case shown in the first case. The relative error between computed and approximated frequencies is smaller than 3% if $p_m \leq 0.2$. On the other hand, it can achieve 7.5% for higher p_m. However, for practical engineering applications the use of the proposed equation for f_{ap} is a convenient alternative to the time integration computational process.

Figure 31 – Quadrotor (solid blue line) and payload mass (dashed black line) normalized altitudes for the second flight.
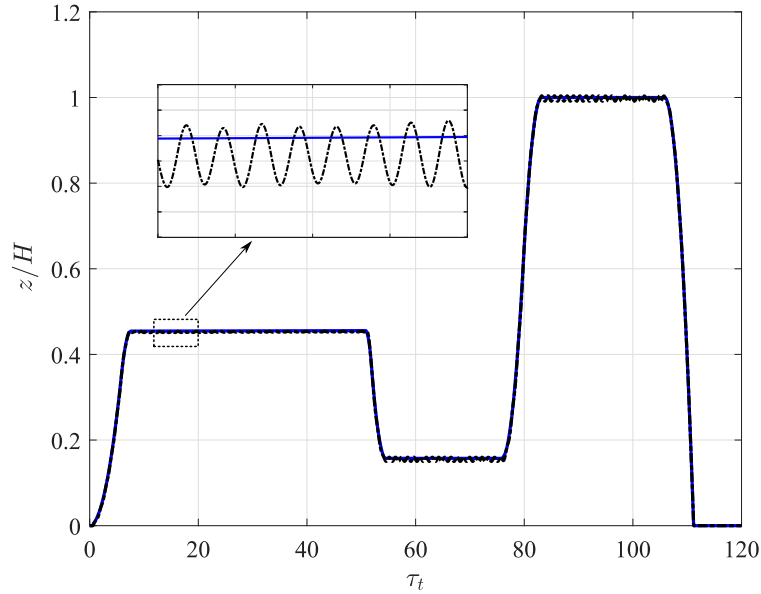
Source: Geronel, Dowell and Bueno (2021).

Note when comparing Figures 28 and 31, there is a difference in the non-dimensional oscillation frequency. The difference is caused by change of altitude, where the relative trajectory is increased, and consequently the payload oscillation frequency values. Different flights, including more transitions of altitude can be found in (GERONEL; DOWELL; BUENO, 2021). The proposed expression aims to compute the approximate oscillation frequency that provides results with relative errors lower than 5% if the payload m_p is limited to 20% of the quadrotor mass m. Therefore, the equation of oscillation frequency (Eq. (29)) can be used in practical applications to estimate the payload oscillation frequency of different flights, when values of stiffness and mass of the payload are known.

Figure 32 – Non-dimensional oscillation frequency of the payload mass during the flight using $p_i = 0.01$, where $f_r = 5.0\ Hz$ (symbol △), $f_r = 10\ Hz$ (symbol ○), $f_r = 20\ Hz$ (symbol +) and oscillation frequency (solid black line).
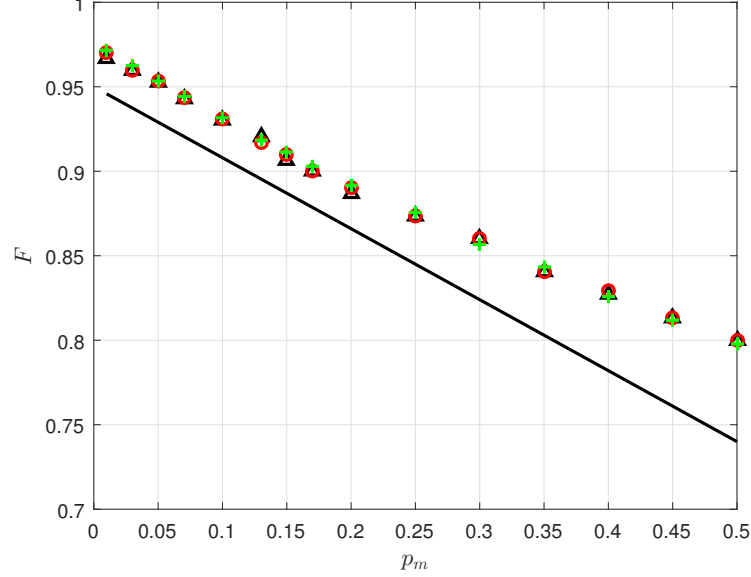
Source: Geronel, Dowell and Bueno (2021).

4.3 AUTONOMOUS FLIGHT

In contrast to the quasi-open loop control, the closed loop control is designed based on the desired trajectory. Additionally, to evaluate the payload vibration in commercial quadrotors, the design of the proposed controllers do not consider the total effect of the new dynamic system. The proposed controllers consider four inputs to the dynamic model, such as the vertical altitude z, roll ϕ, pitch θ, and yaw ψ angles. The development and comparison of two controllers: Proportional Derivative and Sliding Mode Control is presented in this Section. These controllers are chosen due to their easy implementation, robustness and commonly adoption in commercial UAVs.

This development aims to achieve not only the UAV trajectory tracking stabilization, but also to guarantee an attenuation of the relative displacements between the quadrotor and its attached system subjected to external disturbances. The controller acts directly on the quadrotor and indirectly on the payload, since any effect that the quadrotor is subjected to, undergoes to its payload. These controllers are selected for this study because they are the most used for commercial quadrotors, as shown in (CASTILLO-ZAMORA *et al.*, 2018).

As noted in the modeling sections, the translational and rotational dynamics of the quadrotor are decoupled. This dynamic structure allows to design a two cascaded loops,

Figure 33 – Control strategy for the quadrotor.
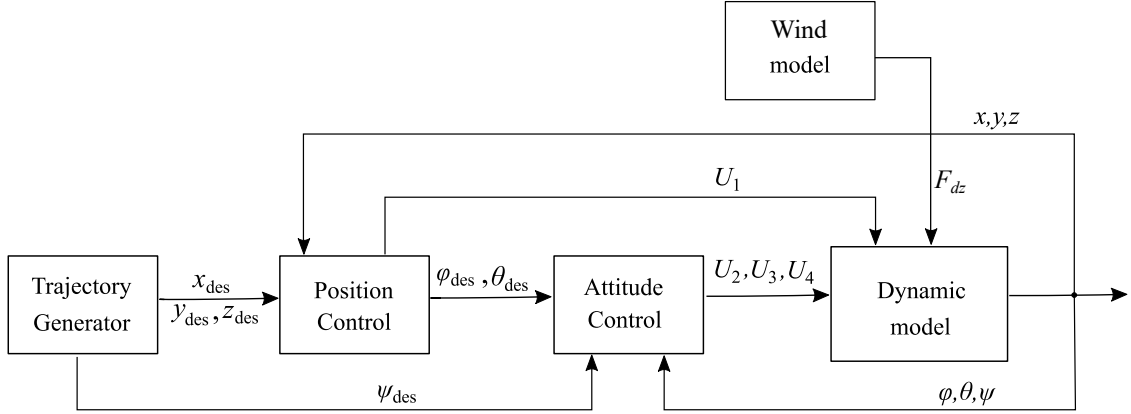
divided into position and attitude. The outer loop is related to the Position Controller by giving the input U_1 to the dynamic model, and by providing the set of points $(\phi_{des}, \theta_{des})$ for the inner loop. The inner loop is related to the Attitude Controller, which provides the inputs U_2, U_3 and U_4 to the dynamic model.

In contrast to conventional quadrotors, the position controller U_1 requires the combination of the vertical motion equations from the quadrotor with those of the payload output, since the U_1 must be able to lift the total mass. As an under actuated system, the compensation for U_1 is then used for the whole controller, since the inputs and outputs for both loops are directly linked. For instance, the pair $(\phi_{des}, \theta_{des})$ depends on the U_1 to be calculated and at the same time is responsible to generate the other inputs U_2 and U_3. Figure 33 represents the cascade control strategy.

The wind model is developed using the Dryden gust methodology applied only in the vertical direction for the quadrotor and its payload, such that the Dryden disturbance is a force defined as F_{dz}, as seen in Eq. (42) - Section 4.3.2.

4.3.1 Proportional Derivative Control

The Proportional Derivative control design is described in this sub-section. Since the proposed attachment adopted, any disturbance (gust, vibration) that affects the quadrotor may also direct affect the payload, i.e. the motion of the payload z_p is directly related to z. The modified control law in the z direction is defined by the total thrust of motors

$$U_1 = \tilde{m}(g + r_z)/c\phi c\theta \tag{30}$$

where r_z can be written as $r_z = k_{pgz}(z_{des} - z) + k_{dgz}(\dot{z}_{des} - \dot{z})$. In addition, z_{des} and z are the desired and current altitudes, $\dot{z}_{des}$ and $\dot{z}$ are their time derivatives, and k_{pgz} and k_{dgz} are the proportional and derivative gains of the controller, respectively. As widely seen in literature, $\tilde{m}$ is defined only for the quadrotor mass (SUBUDHI; EZHILARASI, 2018). However, with the presence of an attached payload, the extra weight added to the quadrotor must affect the flight altitude. To compensate for the extra weight added to the system, $\tilde{m}$ is defined by $m + m_p$.

In the inner loop, two phases are required to properly control the quadrotor. Firstly, the total thrust needs to be calculated by use of Eq. (30). Secondly, to ensure the motion of the quadrotor in the (x, y) planes, the desired roll and pitch angles $(\phi_{des}, \theta_{des})$ are generated through their expressions, as given in (LIMA, 2015)

$$\phi_{des} = sin^{-1}(s\psi U_x - c\psi U_y) \qquad\qquad \theta_{des} = sin^{-1}[(U_x - s\psi s\phi)/(c\psi c\phi)] \tag{31}$$

where the virtual inputs U_x and U_y are defined as follows:

$$U_x = (r_x\tilde{m})/U_1 \qquad\qquad U_y = (r_y\tilde{m})/U_1 \tag{32}$$

Similar to r_z, in the x and y planes, $r_x = k_{pgx}(x_{des} - x) + k_{dgx}(\dot{x}_{des} - \dot{x})$ and $r_y = k_{pgy}(y_{des} - y) + k_{dgy}(\dot{y}_{des} - \dot{y})$. Moreover, as the inner loop is fully controllable, the torques are applied at roll, pitch and yaw angles (ϕ, θ, ψ). After linearizing and applying the necessary simplifications, the rotational equations can be defined as: $U_2 = (I_{xx} + \Delta I_{xx})\ddot{\phi}$, $U_3 = (I_{yy} + \Delta I_{yy})\ddot{\theta}$, and $U_4 = (I_{zz} + \Delta I_{zz})\ddot{\psi}$. Thus, the inputs of the simplified rotational proposed controller are defined as follows

$$\begin{aligned} U_2 &= k_{pg\phi}(\phi_{des} - \phi) + k_{dg\phi}(\dot{\phi}_{des} - \dot{\phi}) \\ U_3 &= k_{pg\theta}(\theta_{des} - \theta) + k_{dg\theta}(\dot{\theta}_{des} - \dot{\theta}) \\ U_4 &= k_{pg\psi}(\psi_{des} - \psi) + k_{dg\psi}(\dot{\psi}_{des} - \dot{\psi}) \end{aligned} \tag{33}$$

where k_{pgw} and k_{dgw} are the proportional and derivative gains defined for the inner loop, where $(w = \phi, \theta, \psi)$.

4.3.2 Sliding Mode Control

This sub-section presents the design of a Sliding Mode Control strategy. The combination between the position and the velocity tracking errors of state variables allows for the development of a second order Sliding Mode Control. The proposed controller system is divided into two sub-systems: i) a fully-actuated sub-system ($\ddot{z}$ and $\ddot{\psi}$) and ii)

an under actuated subsystem ($\ddot{x}$, $\ddot{y}$, $\ddot{\phi}$ and $\ddot{\theta}$). The fully actuated controller ensures the convergence of the current variables $[z, \psi]$ to the desired ones $[z_{des}, \psi_{des}]$. For the vertical motion variable z, a sliding surface equation determines the dynamics of the system by using (UTKIN, 2013)

$$s_z = \lambda_z(z_{des} - z) + (\dot{z}_{des} - \dot{z}) \tag{34}$$

where λ_z is a tuning parameter associated with the closed loop bandwidth. Furthermore, the derivative of s_z is calculated with respect to time such as $\dot{s}_z = \lambda_z(\dot{z}_{des} - \dot{z}) + (\ddot{z}_{des} - \ddot{z})$.

In fact, the time derivative s_z can also be defined by using a discontinuous state function to enforce the proposed controller on the surface, such that $\dot{s}_k = -\epsilon_k sat(s_k) - \eta_k s_k$, where ϵ_k and η_k are the sliding surface exponential approach coefficients, $w = x, y, z, \phi\theta, \psi$ and sat(.) indicates the saturated function. By combining the time derivative ($\dot{s}_z$), the state function ($\dot{s}_k$) and the equations of motion in the z and z_p directions (Reinoso et $al.$ (2016)) the corresponding control law input is defined as

$$U_1 = \frac{\tilde{m}}{c\theta c\phi}(\epsilon_z sat(s_z) + \eta_z s_z + \lambda_z(\dot{e}_z) + \ddot{z}_{des} + g) \tag{35}$$

where $\dot{e}_z$ is the difference between the desired and the calculated state variables ($\dot{z}_d$ - $\dot{z}$), and $sat(s_k)$ is the saturated function used to alleviate the effect of chattering on the actuators, as shown in (REINOSO et $al.$, 2016)

$$sat(s_k) = \frac{s_k}{|s_k| + \gamma} \tag{36}$$

where γ is the parameter used to define the transition bandwidth (which can reduce the chattering effect on the actuators). Likewise to the Proportional Derivative, in the inner loop, two phases are required to control the quadrotor. First, the total thrust must be calculated with the Eq. (35). Second, to enable the motion of the quadrotor in the (x, y) plane, the desired roll and pitch angles (ϕ_{des}, θ_{des}) are generated through two virtual inputs. These inputs are two dependent position states (x, y) for the SMC, and each position state requires virtual inputs to obtain the under-actuated controller parameters. Therefore, the desired angles of roll and pitch for designing the attitude control are obtained with Eq. (37) (ZHENG; XIONG; LUO, 2014)

$$\phi_{des} = sin^{-1}(u_x s\psi - u_y c\psi) \qquad\qquad \theta_{des} = sin^{-1}\left(\frac{u_x c\psi + u_y s\psi}{c\psi}\right) \tag{37}$$

where u_x and u_y are defined by $u_x = \frac{\tilde{m}}{U_1}(\ddot{x}_{des} + \lambda_x \dot{e}_x + e_x)$ and $u_y = \frac{\tilde{m}}{U_1}(\ddot{y}_{des} + \lambda_y \dot{e}_y + e_y)$, where λ_x, λ_y are positive real constants. Similarly, U_2, U_3 and U_4 are obtained following

the same steps as the ones mentioned previously for U_1, yielding the next Eq. (38)

$$U_2 = \frac{I_{xx} + \Delta I_{xx}}{l}(\ddot{\phi}_{des} + \lambda_\phi \dot{e}_\phi + \eta_\phi s_\phi + \epsilon_\phi sat(s_\phi)) - [(I_{yy} + \Delta I_{yy}) - (I_{zz} + \Delta I_{zz})]l\dot{\theta}\dot{\psi}$$

$$U_3 = \frac{I_{yy} + \Delta I_{yy}}{l}(\ddot{\theta}_{des} + \lambda_\theta \dot{e}_\theta + \eta_\theta s_\theta + \epsilon_\theta sat(s_\theta)) - [(I_{zz} + \Delta I_{zz}) - (I_{xx} + \Delta I_{xx})]l\dot{\phi}\dot{\psi}$$

$$U_4 = (I_{zz} + \Delta I_{zz})(\ddot{\psi}_{des} + \lambda_\psi(\dot{e}_\psi) + \eta_\psi s_\psi + \epsilon_\psi sat(s_\psi)) - [(I_{xx} + \Delta I_{xx})$$
$$-(I_{yy} + \Delta I_{yy})]\dot{\theta}\dot{\phi}$$

$$(38)$$

where λ_ϕ, λ_θ, λ_ψ, ϵ_ϕ, ϵ_θ, ϵ_ψ, η_ϕ, η_θ and η_ψ are also positive real constant parameters, and ΔI_{xx}, ΔI_{yy} and ΔI_{zz} are parameters related to the uncertainties dues to the payload dynamics added to the quadrotor dynamics. In practical situations, the configuration of the cargo (that can be placed horizontally or vertically) can influence differently its contribution on the global moment of inertia and consequently to the stiffness characteristics. However, to simplify the control equations, a nominal parameter is considered to represent the average payload´s moment of inertia (ΔI_{ww}).

These equations of motion can also be rewritten as $\ddot{k} = f_k + g_k U_j + \Delta f_k$, (such that $k = x, y, z, \phi, \theta, \psi, z_p$ and $i = 1, 2, 3, 4$). For instance, the second-order derivative of roll $\ddot{\phi}$ is expressed with the following expression $\ddot{\phi} = [(\dot{\theta}\dot{\psi}(I_{yy} - I_{zz}))/I_{xx}] + [1/I_{xx}]U_2 + [-(\dot{\theta}\dot{\psi}(I_{yy} - I_{zz}) + U_2)\Delta I_{xx}/[I_{xx}(I_{xx} + \Delta I_{xx})] + \dot{\theta}\dot{\psi}(\Delta I_{yy} - \Delta I_{zz})(I_{xx} + \Delta I_{xx})]$.

Dryden Continuous Gust

Turbulence, also called wind gust, is described as a brief change of wind velocity caused by atmospheric pressure and temperature. Therefore, a realistic model is required to evaluate its effects on a UAV (ZHANG *et al.*, 2016), and the Dryden and Von Kármán are two of the most common models used to study the wind effects on UAVs. The expression of the Dryden Power Spectral Density (PSD) defining the turbulence velocity in the vertical direction is represented by

$$\Phi_z(\Omega_d) = \sigma_z^2 \frac{L_z}{\pi} \frac{1 + 3(L_z\Omega_d)^2}{(1 + (L_z\Omega_d)^2)^2} \tag{39}$$

Fundamentally, a Power Spectral Density (PSD) function is parameterized using the turbulence scale length (L_z) and standard deviations (or turbulence intensities), defined as σ_z. For lower-altitudes than 60m, these parameters are given by $L_z = h$ and $\sigma_z = 0.1 w_{ws}$, where w_{ws} denotes the mean wind speed and h is the flying altitude of the quadrotor. Then, in order to generate the wind gust velocity, a white noise signal is filtered through a shaping function, as shown in Figure 34. The relationship between the Power Spectral

Figure 34 – Process for generating Dryden wind velocity model.
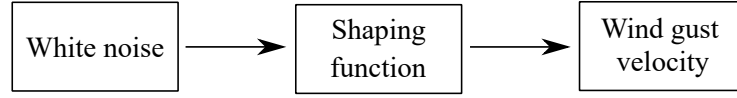
Source: Geronel, Botez and Bueno (2022a).

Density (PSD) and the transfer function is given by (LV; YANG; CHAI, 2019)

$$\Phi_j(\Omega_d) = |G(j\omega)^2| = G^*(j\omega)G(j\omega) \qquad (40)$$

where $*$ indicates the complex conjugate of the transfer function. The transfer function of the shaping filter can be obtained by decomposing the PSD, as seen in Eq. (40), and in (ABOUDONIA; RASHAD; EL-BADAWY, 2015)

$$G_z(s) = \frac{v_{z_d}(s)}{\eta_{gz}(s)} = \sigma_z \sqrt{\frac{L_z}{\pi V}} \frac{1 + \frac{\sqrt{3}L_z}{V}s}{(1 + \frac{L_z}{V}s)^2} \qquad (41)$$

where η_{gz} denotes the white Gaussian noise in the frequency domain. V is the wind velocity and s is the Laplace variable (which can be replaced by $j\omega$ in order to solve the Eq. (41)). Therefore, after finding the wind velocity v_{z_d} and converting it into time, the wind gust velocity in the inertial reference can be represented as $v_{wz} = \bar{v}_{wz} + v_{z_d}$, where $\bar{v}_{wz}$ denotes the mean wind velocity in the z direction. Finally, the Dryden disturbance F_{dz}, that acts on the UAV during a flight, is defined as

$$F_{dz} = -\frac{1}{2}\rho C_{dz}A_z(\dot{z} - v_{wz})^2 sgn(\dot{z} - v_{wz}) \qquad (42)$$

where ρ is the air density, C_{dz} is the drag coefficient, $sgn(.)$ denotes the sign function, A_z is the area projected by the UAV and $\dot{z}$ is the velocity along the z axis, respectively. The same steps are required to design the Dryden disturbance force that acts on the payload, switching only the velocity of the payload $\dot{z}_p$ instead of $\dot{z}$.

4.3.3 Controllers Performance Analysis on Relative Displacement

The dynamic parameters of the quadrotor with an attached payload are presented in Table 8 in terms of their physical and geometrical properties. The initial yaw angle is considered as $\psi = 0.5rad$, while the other desired initial states $(x, y, z, \phi, \theta, \psi)$ are defined as equal to zero. The controller gains of both controllers (PD and SMC) are listed in Table 9. The PD gains are initially selected according to their values previously employed in (LIMA, 2015), and the SMC gains are chosen based on the pole placement method. The defining step of the controller gains is very important to obtain a successful controller

design. These following results are obtained by integrating Eq. (12) in time domain, using Matlab software. The Fourth Order Runge-Kutta algorithm was employed with time step 2×10^{-4} seconds.

Table 8 – Parameters of the quadrotor model.

Parameter	Value	Unit	Parameter	Value	Unit
m	2.2	kg	I_x	0.0167	kgm^2
l	0.1725	m	I_y	0.0167	kgm^2
g	9.81	m/s^2	I_z	0.0231	kgm^2

Source: Geronel, Botez and Bueno (2022a).

Table 9 – Controller gains computed for the PD and SMC.

Method	Parameters	Value	Parameters	Value
PD	k_{pgx}, k_{pgy}, k_{pgz}	1.50, 1.60, 1.50	k_{dgx}, k_{dgy}, k_{dgz}	1.80, 1.80, 2.00
	$k_{pg\phi}$, $k_{pg\theta}$, $k_{pg\psi}$	0.40, 0.70, 1.00	$k_{dg\phi}$, $k_{dg\theta}$, $k_{dg\psi}$	0.10, 0.05, 0.05
SMC	ϵ_z, η_z, γ	1.80, 0.40, 0.20	ϵ_ϕ, ϵ_θ, ϵ_ψ,	1.50, 1.10, 1.10
	λ_x, λ_y, λ_z	3.00, 3.20, 3.20	λ_ϕ, λ_θ, λ_ψ	1.50, 1.50, 1.50
	η_ϕ, η_θ, η_ψ	0.04, 0.04, 0.04		

Source: Geronel, Botez and Bueno (2022a).

The flight trajectory used to evaluate the relative trajectory oscillation is shown in Figure 35, and this trajectory is built for three phases: transient P_1, cruise P_2, and landing P_3. The first phase occurs between the beginning of a flight and the time when the quadrotor reaches the desired altitude (in the absence of transient effects). The second phase represents the cruise path, where the quadrotor flies horizontally at the same altitude, while the third phase covers the descent until the quadrotor lands on the ground [1].

The controller acts directly on the quadrotor motion, by orientating its flight on a pre-defined trajectory. Due to the physical relationship between the quadrotor and its payload, the controller is responsible for suppressing partially residual oscillations. Figure 35 depicts the proposed trajectory, showing the quadrotor and its payload oscillations over three phases of the flight.

The relative trajectory oscillation is defined by the difference between the vertical displacement of the payload and the vertical displacement of the quadrotor, denoted by $z - z_p$. In the beginning of the flight, when a transient effect occurs, the oscillations can be differently attenuated by using both controllers (SMC and PD). Figure 36 shows

---

[1]for the proposed dynamic model, the distance between the payload and quadrotor is neglected

Figure 35 – Trajectory of the quadrotor in the z direction, showing the desired trajectory (solid red line), the quadrotor path (solid blue line) and the payload displacement (dashed black line).
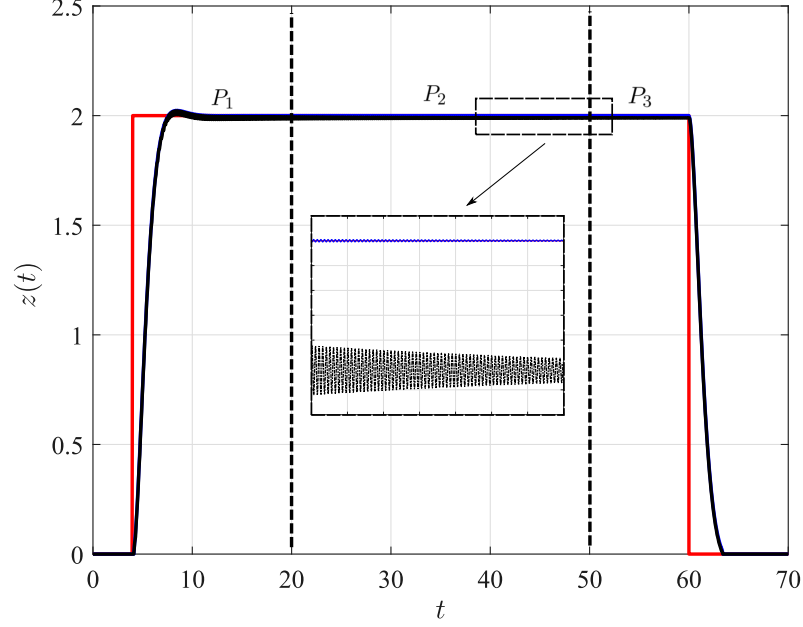
Figure 36 – Relative trajectory oscillation in the transient phase, for the PD (dashed blue line), and the SMC (solid red line).
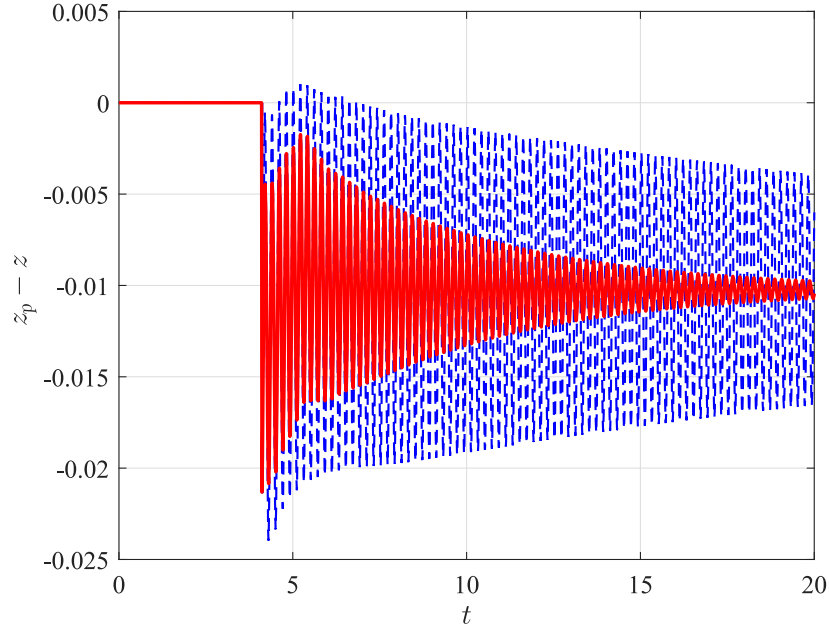
the oscillation of each controller during the first phase P_1. The relative trajectory oscillation between the quadrotor and its payload can then be calculated with a Fast

Fourier Transform (FFT), denoted by $|Z|$.

Note that in the first phase (P_1) the relative oscillations are higher than other phases, since the cargo oscillates more significantly in the beginning of the flight (when it leaves the ground). Figure 36 shows that the SMC presents better performance compared to that of the PD, as the transient phase has less effect the SMC case. Figure 37 shows the frequency spectrum of the oscillation, for which the SMC amplitude peak is approximately 35% of the PD. Note that the payload displacement z_p is different when comparing the SMC and the PD controllers' performance. The SMC laws guarantee a better adherence to the quadrotor trajectory, and therefore better oscillation suppression as results in comparison to the PD results.

Figure 37 – Frequency spectrum of the relative trajectory oscillation at P_1, for the PD (dashed blue line), and the SMC (solid red line).

Source: Geronel, Botez and Bueno (2022a).

Both controllers are also used to evaluate the performance of a quadrotor when is subjected to an external disturbance during the second phase P_2. The proposed controllers are designed to reduce the relative trajectory oscillation produced by the coupling of a quadrotor with its attached mass.

If the UAV is subjected to the external disturbances, its trajectory is suddenly changed, and depending on the coupling parameters adopted, the relative displacement can be either enhanced or reduced. Thereby, the controllers must not only stabilize the tracking, but they should also guarantee an attenuation of the oscillations. Figure 38 shows the effect of an external disturbance during the second (cruise) phase P_2 for both

controllers. Regarding the controller comparison, external disturbances are applied only in the second phase (P_2), however in outdoor environment they can occur during the whole flight. The difference in the vertical direction of the quadrotor and its payload is due to the physical distance of the proposed attachment. The payload is translated vertically below from the CoG of the quadrotor, in order to allow the payload to move freely in this respective direction.

Figure 38 – Trajectory affected by a vertical Dryden wind disturbance using: a) the PD, and b) the SMC, showing the desired trajectory (solid red line), the quadrotor (solid blue line), and the payload displacement (dashed black line).
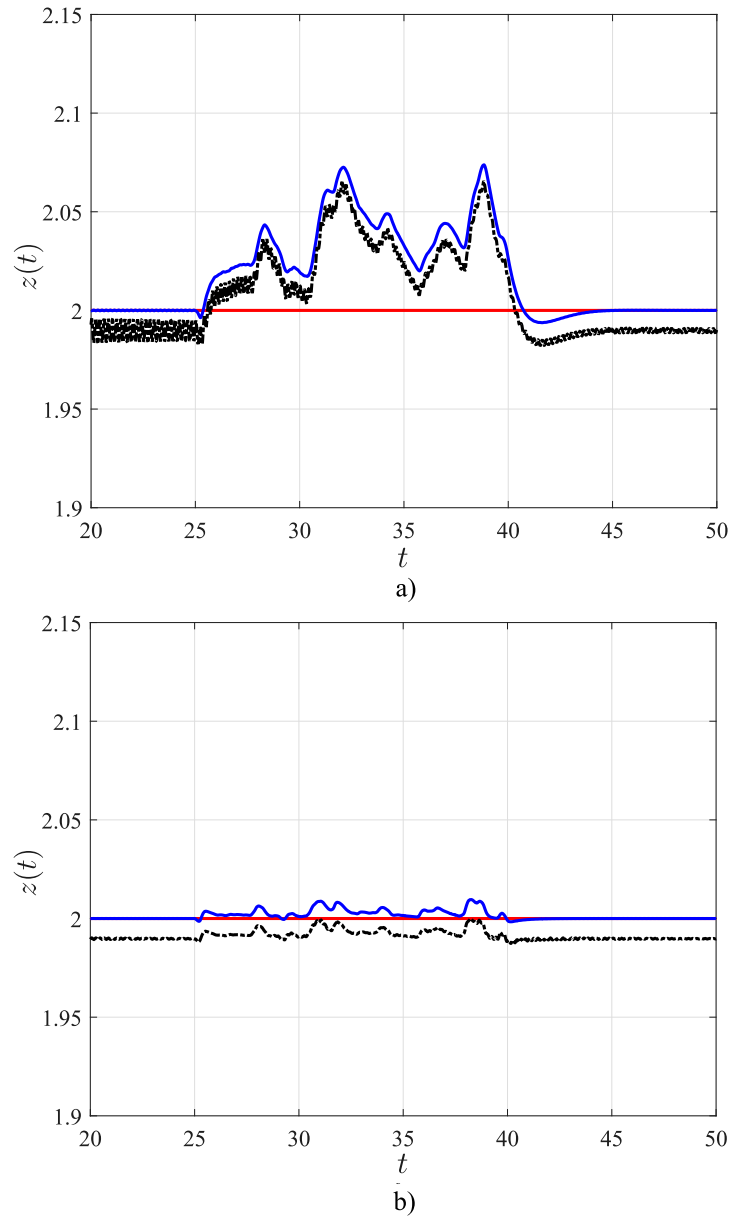
Source: Geronel, Botez and Bueno (2022a).

In the absence of external disturbance, the signal has its main impact only for a

specific frequency, while in the presence of external disturbance, the response is affected during a range of frequencies, as seen in Figure 39. Moreover, the peak is smaller and the band is narrower than when a disturbance impacts on the trajectory. It can be seen in Figure 38 that the SMC reduces the oscillation more than the PD. Especially at the time when a disturbance is applied to the system [25-40] seconds, not only the peak amplitude calculated with the SMC is smaller than that calculated with the PD, but the time required for the system to return to a minimum oscillation is also reduced. Figure 39 illustrates the presence and absence of an external disturbance. Figure 40 shows the relative trajectory oscillation between the quadrotor and the payload during the second phase P_2.

Figure 39 – Frequency spectrum of the relative trajectory oscillation during the cruise phase P_2, that shows the presence of disturbance (solid red line), and the absence of disturbance (solid black line).
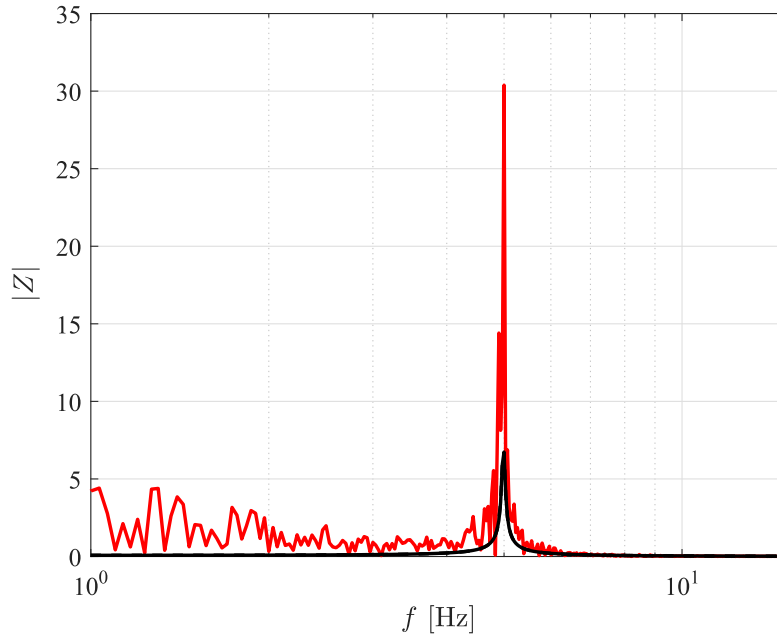
Source: Geronel, Botez and Bueno (2022a).

Figure 40 – Relative trajectory oscillation in the second (cruise) phase, for the PD (dashed blue line), the SMC (solid red line), and and the boundaries of the external disturbance (solid black lines).
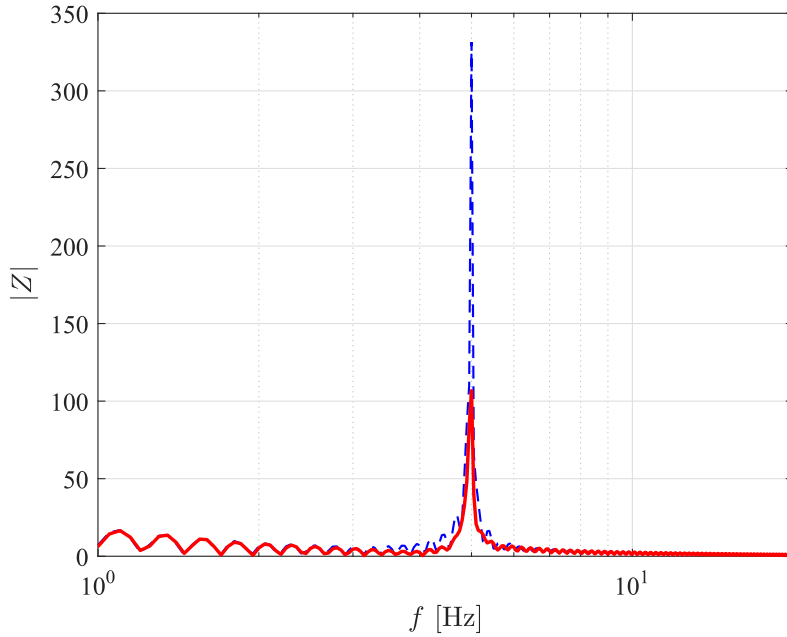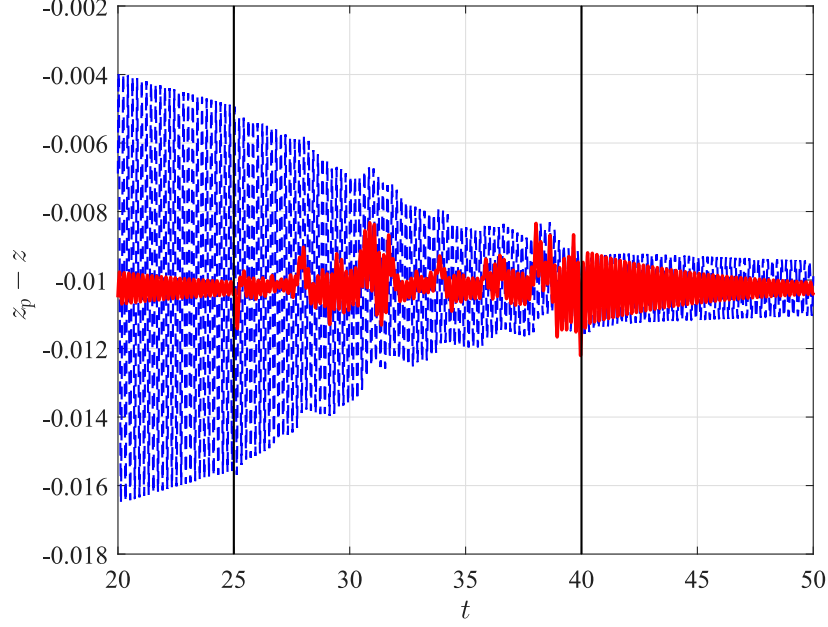

Source: Geronel, Botez and Bueno (2022a).

The SMC is able to reduce the gust effect more than the PD mainly because its formulation allows one to consider boundary uncertainties. Note that a discontinuous state function ($\dot{s}_k = -\epsilon_k sat(s_k) - \eta_k s_k$) was used to enforce the proposed controller on the surface, which improves the SMC with respect to the PD in terms of noise reduction and trajectory adherence. This approach allowed the quadrotor to follow smoothly its desired path, and therefore to ensure lower effects on its payload performance. Likewise, by applying the Fast Fourier Transform (FFT) to the signal ($z_p - z$), it can be shown that the peak calculated with the SMC is around eight times smaller than that found by using the PD. Figure 41 shows the frequency spectrum when an external disturbance is applied on the quadrotor and its attached system during the cruise phase.

In the last phase of landing (P_3), the controllers can attenuate the relative trajectory oscillation, however in contrast to the other two phases, the SMC presents a slight increase of oscillation amplitudes compared to the PD when the quadrotor begins the landing process [60-64] seconds. On the other hand, when the analysis covers the whole P_3 phase [50-70] seconds, the SMC still gives a better performance than the PD. Figure 42 shows the relative trajectory oscillations when a quadrotor is in the landing process, while Figure 43 presents the frequency spectrum of the signal. Note that in all frequency spectrum graphics (Figures 37, 41 and 43), there is a single peak exhibited. The frequency peak

Figure 41 – Frequency spectrum of the relative trajectory oscillation during the second phase P_2, obtained with the PD (dashed blue), and the SMC (solid red line).
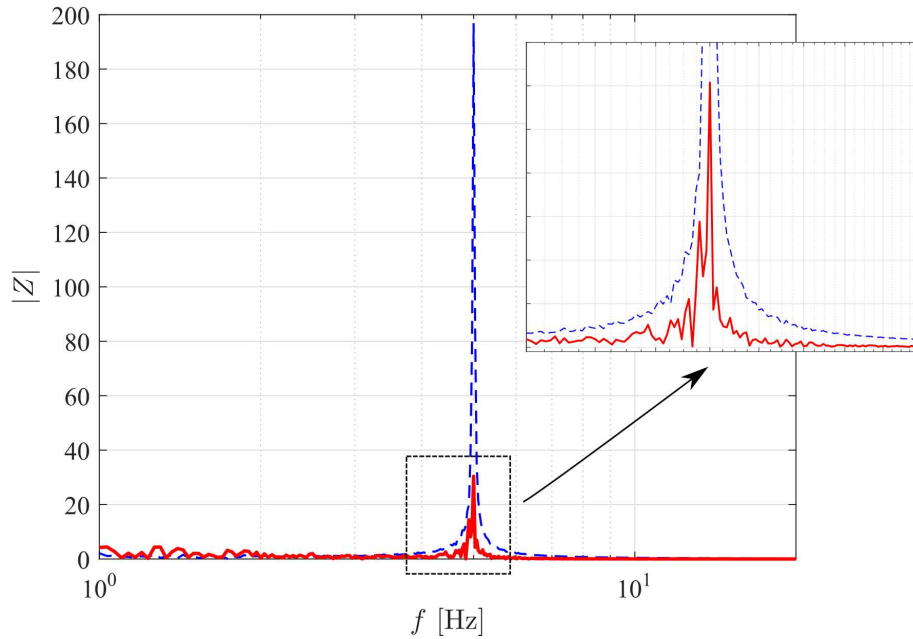
Source: Geronel, Botez and Bueno (2022a).

refers to the only elastic axis of the model (vertical), whereas the others axes are assumed to be a rigid body.

Figure 42 – Relative trajectory oscillation in the landing phase, for the PD (dashed blue line), and the SMC (solid red line).
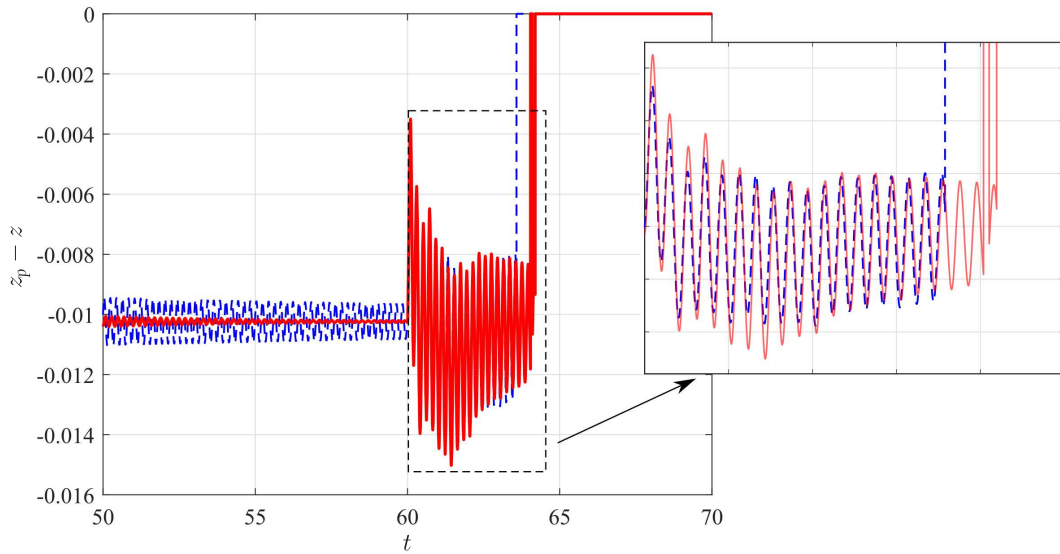
Source: Geronel, Botez and Bueno (2022a).

Figure 43 – Frequency spectrum of the relative trajectory oscillation during phase P_3, for the PD (dashed blue line), and the SMC (solid red line).
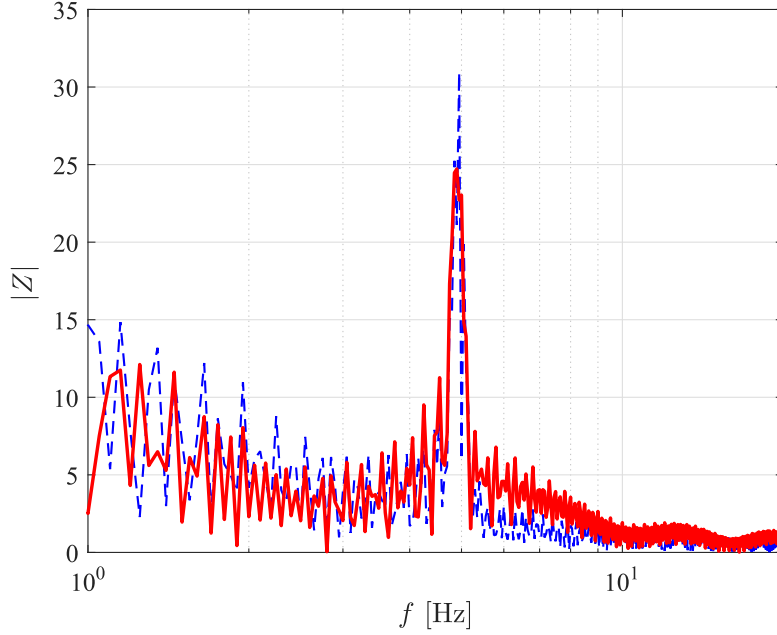
Source: Geronel, Botez and Bueno (2022a).

4.3.4 Performance Indices

Performance indices are employed to evaluate both controllers in different phases of flight, as well as their relative oscillations. A system exhibits its best performance when the controller parameters are adjusted to reach the minimum values of the performance indices (DORF; BISHOP, 2011). The first index is called the Integral of the Absolute magnitude of the Error (IAE), which is used in numerical simulations and is defined with the next Eq. (43)

$$IAE = \int_0^T |e_o(t)| dt \tag{43}$$

where $|e_o(t)|$ is the absolute oscillation error, and is given by the difference between the quadrotor and the payload displacements ($|z_p - z|$). T is the final time of each flight phase (since the trajectory is divided into three phases: taking-off, cruise and landing). Another proposed performance index is called the Integral of Time multiplied by the Absolute Error (ITAE), that is designed to reduce the errors at the beginning of the signal, as well as to obtain the steady-state error

$$ITAE = \int_0^T t|e_o(t)| dt \tag{44}$$

where t is the simulation time. To compare the performance indices of the two controllers, a percentage parameter can be defined as $P_{pi} = 100\frac{P_{SMC}}{P_{PD}}$, where P_{pi} is the percentage of the performance index (IAE and $ITAE$). The term P_{SMC} is the index calculated at each phase for the Sliding Mode Control, and P_{PD} is the index calculated by the Proportional Derivative. Table 10 shows the performance indices calculated for each flight phase.

Table 10 – Performance indices [%] for the controllers during three trajectory phases.

Disturbance Position Index	Transient Phase P_1	Cruise Phase P_2	Landing Phase P_3
P_{IAE}	35.40%	11.38%	48.25%
P_{ITAE}	26.73%	13.76%	49.51%

Source: Geronel, Botez and Bueno (2022a).

Based on the Table 10, all performance indices percentages show an advantage for using the SMC rather than the PD (since all percentage of performance indices are lower than 100%, thus they indicate a higher values of P_{PD} than the P_{SMC} values). For instance, by considering the P_{IAE} at the transient phase, the SMC requires only 35.40% of the energy spent by the PD. In addition, when an external disturbance is added to the dynamic system during the cruise phase P_2, a more significant reduction can be observed, since the P_{SMC} represents only 11.38% of the energy required by the P_{PD}. Note that if the external disturbances were applied in other phases, the indices would also present a higher difference. However, to evaluate their individual characteristics on the controller performance (since in phases P_1 and P_3, there is the presence of sudden acceleration), the disturbance vector is included only in the cruise phase. Thereby, when analyzing the results obtained for the third phase, the SMC shows a better performance than the PD (with smaller oscillation amplitude, around 49% less interference with the quadrotor and on-board payloads dynamics).

4.4   FINAL REMARKS

This chapter presents the dynamic model of a 7 degree of freedom quadrotor and its attached payload. The attachment system is composed by a stiffness and an attached mass, which ensures the payload to oscillate vertically. A convenient approach is provided to obtain a non-dimensional equation of motion and it is verified by numerical results. This approach allows one to estimate the vertical oscillation of a payload during the flight depending on the stiffness of attachment. The control strategy uses pre-defined forces to guide the quadrotor along a desired trajectory, allowing to estimate the payload frequency

oscillation over the path. The proposed equation to estimate the frequency of oscillation is more accurately for $p_m < 0.2$ and the results demonstrated that typical flight maneuvers do not affect the estimates substantially. The findings are especially interesting to support the design of cargo quadrotors for better performance and vibration control.

On the other hand, two control strategies have been used to investigate the relative trajectory oscillation between the quadrotor and its payload, as well as the quadrotor performance under external wind disturbances. The proposed strategy allows to compare both controllers (SMC and PD) results in different flight phases and to understand the impact of external disturbances, and maneuvers on the quadrotor flight. The Sliding Mode Controller has a fast response to fit to the trajectory, especially to compare its performance to the Proportional Derivative (PD). The SMC's faster convergence to the desired point in space is related to its robust control law even under uncertainty parameters (such as external disturbance), which guides and fits strongly the quadrotor trajectory on its proposed path. Performance Indices are used to measure the vibration intensity during different phases of the flight.

5 FLEXIBILITY ANALYSIS ON THE DYNAMICS OF A SUSPENDED PAYLOAD

The market for UAVs in the medical field is significant and it is predicted to increase by 25% between 2019 and 2025 (USD 400 million). However, due to the sensitivity of some products to vibrations, commercial UAVs companies must satisfy operational procedures to not cause any adverse effects on the medical products. In this context, the dynamic model of a payload with three translational and two rotational axes have been developed to investigate the vibrations characteristics over a flight. This new approach represents one of the most common configuration adopted by commercial UAV companies in medical transportation field (ACKERMAN; STRICKLAND, 2018), (KEEFFE; JOHNSON; MARAKA, 2020) and (CICHOSZ, 2019).

This chapter investigates the characteristics of a quadrotor with an 11 degrees of freedom and the design of an Adaptive Sliding Mode control. Section 5.1 describes the proposed dynamic model of a quadrotor with an 11 degrees of freedom, while Section 5.2 presents the Adaptive Sliding Model control design for tracking trajectory and suppressing payload residual oscillation. Numerical results have shown the vibration characteristics and the adaptive controller performance.

5.1 DYNAMIC MODEL

Likewise in Section 4.1.1, two coordinate frames are used to describe the quadrotor motion, which is represented by fix degrees of freedom. Five additional degrees of freedom are used to represent the payload motion. While x_p, y_p and z_p represent the payload position, the terms ϕ_p and θ_p represent the payload rotation. In addition, the connection between the quadrotor and its payload is assumed to be an elastic attachment, in which F_s is the resultant of constraint forces components (F_{sx}, F_{sy} and F_{sz}). Each of constraint forces components is represented by $F_{sc} = k_p(j - j_p) - k_p l_b r_{qp}$ (where $j = x, y, z$) and l_b is

the physical distance between the quadrotor and its payload. Figure 44 shows the elastic attachment between the quadrotor and its payload, where m and m_p are the quadrotor and payload masses, respectively.

Figure 44 – Schematic illustration of the payload dynamics, showing the attachment constraint forces.
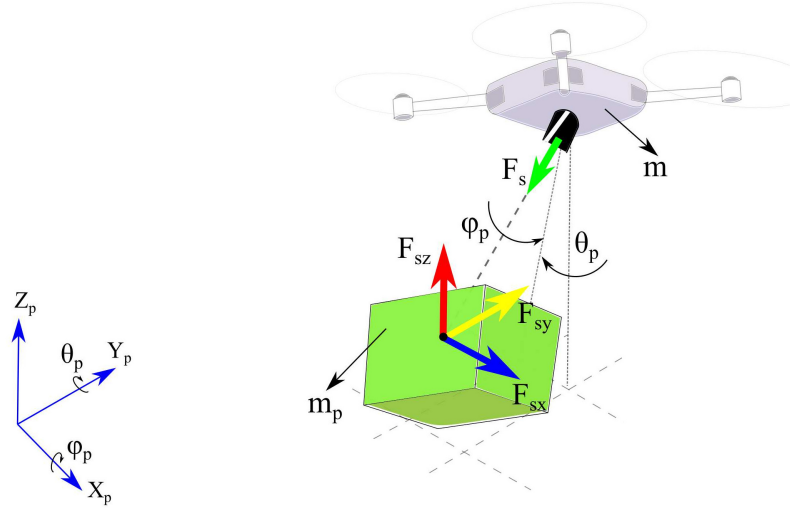
Source: Geronel, Botez and Bueno (2022b).

The combination of swing-payload and elastic attachment dynamics allows the payload to move and vibrate freely in the three-dimensional trajectory, with respect to the quad-rotor's motion. The equation of motion of a quadrotor carrying a payload is presented as follows

$$\mathbf{M}_I\ddot{\boldsymbol{\eta}}_I + \mathbf{C}_I\dot{\boldsymbol{\eta}}_I + \mathbf{K}_I\boldsymbol{\eta}_I + \mathbf{g}_I = \boldsymbol{\tau}_I + \mathbf{F}_d + \mathbf{F}_{Sk} \tag{45}$$

where $\mathbf{M}_I$ is the matrix of inertia, $\mathbf{C}_I$ represents the Coriolis matrix, $\mathbf{K}_I$ is the stiffness matrix, $\mathbf{g}_I$ is the gravitational vector, $\boldsymbol{\tau}_I$ is the input control, and $\mathbf{F}_{Sk}$ is the constraint force vector. In contract to the previous dynamic model, all matrices of Eq. (45) exhibits a (11×11) dimension, whereas the dimension of their vectors corresponds to (11×1). Note that, in comparison to the first approach, a constraint force vector is included to the motion equation to relate the quadrotor and payload's influence and also to represent the physical distance between them. The generalized state vector is defined by 11 degrees of freedom with the following Eq. (46)

$$\boldsymbol{\eta}_I = \{x \ y \ z \ \phi \ \theta \ \psi \ x_p \ y_p \ z_p \ \phi_p \ \theta_p\}^T \tag{46}$$

or rewritten as $\boldsymbol{\eta}_I = \{\boldsymbol{\eta}_{q_I} \ x_p \ y_p \ z_p \ \phi_p \ \theta_p\}^T$. The state vector $\boldsymbol{\eta}_I$ is rearranged (in comparison to Section 4.1.2) to maintain the same order of the quadrotor's states (as

seen in Section 4.1.1). The distance vector between the quadrotor and its payload is defined by $r_{qp} = \{-l_b c\phi_p s\theta_p \ -l_b s\phi_p \ \ -l_b c\phi_p c\theta_p\}^T$. Additionally, matrices of inertia $(\mathbf{M}_I)$ and Coriolis $(\boldsymbol{C}_I)$ are represented as follows

$$\mathbf{M}_I = \begin{bmatrix} \mathbf{M}_1 & \mathbf{M}_2 \\ \mathbf{M}_3 & \mathbf{M}_4 \end{bmatrix}, \qquad \mathbf{C}_I = \begin{bmatrix} \mathbf{C}_1 & \mathbf{C}_2 \\ \mathbf{C}_3 & \mathbf{C}_4 \end{bmatrix}, \tag{47}$$

The matrices and vectors from the equation of motion can also be written in the body-fixed reference frame, as shown in the following equations

$$\begin{aligned} \mathbf{M}_1 &= \mathbf{I}_{9\times9} \\ \mathbf{C}_1 &= \mathbf{J}_B\mathbf{M}_B^{-1}\mathbf{C}_B\mathbf{J}_B^{-1} - \dot{\mathbf{J}}_B\mathbf{J}_B^{-1} + \mathbf{C}_{dg} \\ \mathbf{K}_1 &= \mathbf{J}_B\mathbf{M}_B^{-1}\mathbf{K}_B \\ \mathbf{g}_1 &= \mathbf{J}_B\mathbf{M}_B^{-1}\mathbf{g}_B \\ \boldsymbol{\tau}_1 &= \mathbf{J}_B\mathbf{M}_B^{-1}\boldsymbol{\tau}_B \end{aligned} \tag{48}$$

Note the Coriolis matrix includes the drag effects. The matrices $\mathbf{M}_2$, $\mathbf{M}_3$ and $\mathbf{M}_4$ are defined as

$$\mathbf{M}_3 = \begin{bmatrix} m_p l_b s\phi_p s\theta_p & -m_p l_b c\phi_p & m_p l_b s\phi_p c\theta_p & \mathbf{0}_{1\times6} \\ -m_p l_b c\phi_p c\theta_p & 0 & m_p l_b c\phi_p s\theta_p & \mathbf{0}_{1\times6} \end{bmatrix} \tag{49}$$

and $\mathbf{M}_2 = \mathbf{M}_3^T$, $\mathbf{M}_4 = diag(m_p l_b{}^2, m_p l_b{}^2 c\phi_p{}^2)$, and $diag(.)$ indicates a diagonal matrix. The Coriolis matrix $\mathbf{C}_1$ is calculated with the following expression $\mathbf{C}_1 = \mathbf{J}_B\mathbf{M}_B^{-1}\mathbf{C}_B\mathbf{J}_B^{-1} - \dot{\mathbf{J}}_B\mathbf{J}_B^{-1}$, such that

$$\mathbf{C}_B = \begin{bmatrix} m\mathbf{C}_{q_{B1}} & \mathbf{0}_{3\times3} & \mathbf{0}_{3\times3} \\ \mathbf{0}_{3\times3} & \mathbf{C}_{q_{pB2}} & \mathbf{0}_{3\times3} \\ \mathbf{0}_{3\times3} & \mathbf{0}_{3\times3} & m_p\mathbf{C}_{q_{B1}} \end{bmatrix} \tag{50}$$

where $\mathbf{M}_B = diag(m, m, m, I_x + I_x^p, I_y + I_y^p, I_z + I_z^p, m_p, m_p, m_p)$, the payload moment of inertia is defined by $I_i^p = \hat{\alpha}_p I_i$, and $\mathbf{C}_{q_{B1}}$ and $\mathbf{C}_{q_{pB2}}$ are defined in Section 4.1. The other matrices $\mathbf{C}_2$ and $\mathbf{C}_4$ are expressed with the following Eqs. 51-52

$$\mathbf{C}_2 = \begin{bmatrix} m_p l_b(c\phi_p s\theta_p \dot{\phi}_p + s\phi_p c\theta_p \dot{\theta}_p) & m_p l_b(s\phi_p c\theta_p \dot{\phi}_p + c\phi_p s\theta_p \dot{\theta}_p) \\ m_p l_b s\phi_p \dot{\phi}_p & 0 \\ m_p l_b(c\phi_p c\theta_p \dot{\phi}_p - s\phi_p s\theta_p \dot{\theta}_p) & -m_p l_b(s\phi_p s\theta_p \dot{\phi}_p - c\phi_p c\theta_p \dot{\theta}_p) \\ \mathbf{0}_{6\times1} & \mathbf{0}_{6\times1} \end{bmatrix} \tag{51}$$

and,

$$\mathbf{C}_4 = \begin{bmatrix} 0 & -m_p l_b^2 s\phi_p c\phi_p \dot{\theta}_p \\ m_p l_b^2 s\phi_p c\phi_p \dot{\theta}_p & m_p l_b^2 s\phi_p c\phi_p \dot{\phi}_p \end{bmatrix} \tag{52}$$

and $\mathbf{C}_3 = \mathbf{0}_{2\times9}$. The drag, aerodynamic and torque coefficients, due to the gyroscopic effect dynamics, are shown with the following Eq. (53)

$$\mathbf{C}_{dg} = \begin{bmatrix} \mathbf{C}_{dg1} & \mathbf{0}_{3\times3} & \mathbf{0}_{3\times3} \\ \mathbf{0}_{3\times3} & \mathbf{C}_{dg2} & \mathbf{0}_{3\times3} \\ \mathbf{0}_{3\times3} & \mathbf{0}_{3\times3} & \mathbf{0}_{3\times3} \end{bmatrix}, \qquad \mathbf{C}_{dg2} = \begin{bmatrix} k_{fax}\dot{\phi} & J_r\bar{\Omega} & 0 \\ -J_r\bar{\Omega} & k_{fay}\dot{\theta} & 0 \\ 0 & 0 & k_{faz}\dot{\psi} \end{bmatrix} \tag{53}$$

and $\mathbf{C}_{dg1} = diag(k_{dfx}, k_{fdy}, k_{fdz})$. The coefficients k_{fdx}, k_{fdx} and k_{fdz} are positive translation drag constants, the terms $k_{fax}\dot{\phi}$, $k_{fax}\dot{\theta}$ and $k_{fax}\dot{\psi}$ are the aerodynamic friction coefficients, J_r is the rotor inertia and $\bar{\Omega}$ is defined by the following relationship $\bar{\Omega} = \Omega_1 - \Omega_2 + \Omega_3 - \Omega_4$. The 9 DOF transformation matrix is given by

$$\mathbf{J}_B = \begin{bmatrix} \mathbf{J}_{q_{B1}} & \mathbf{0}_{3\times3} & \mathbf{0}_{3\times3} \\ \mathbf{0}_{3\times3} & \mathbf{J}_{q_{B2}} & \mathbf{0}_{3\times3} \\ \mathbf{0}_{3\times3} & \mathbf{0}_{3\times3} & \mathbf{J}_{q_{B1}} \end{bmatrix} \tag{54}$$

where $\mathbf{J}_{q_{B1}}$ and $\mathbf{J}_{q_{B2}}$ are defined in Section 4.1. The stiffness matrix is decomposed in x, y and z axes, enabling the overall vibration be the sum of the lateral and vertical components, i.e., to have relative displacements between the quadrotor and payload in all directions. The stiffness matrix is then defined as $\mathbf{K}_I = \begin{bmatrix} \mathbf{K}_{\eta1} & \mathbf{0}_{11\times2} \end{bmatrix}$, such that $\mathbf{K}_{\eta1} = \begin{bmatrix} \mathbf{K}_1 & \mathbf{0}_{2\times9} \end{bmatrix}^T$, and $\mathbf{K}_1 = \mathbf{J}_B \mathbf{M}_B^{-1} \mathbf{K}_B$, yielding

$$\mathbf{K}_B = \begin{bmatrix} \mathbf{k}_{sm} & \mathbf{0}_{3\times3} & -\mathbf{k}_{sm} \\ \mathbf{0}_{3\times3} & \mathbf{0}_{3\times3} & \mathbf{0}_{3\times3} \\ -\mathbf{k}_{sm} & \mathbf{0}_{3\times3} & \mathbf{k}_{sm} \end{bmatrix} \tag{55}$$

where $\mathbf{k}_{sm} = diag(k_{px}, k_{py}, k_{pz})$, such that k_{px}, k_{py}, and k_{pz} are the stiffness proportional terms related to the spring along its corresponding x, y or z directions respectively. Note that the torsional stiffness are not considered in this dynamic model. The control input vector is defined by $\boldsymbol{\tau}_B = \{\boldsymbol{\tau}_1^T \quad \mathbf{0}_{2\times1}\}^T$ (assuming that $\boldsymbol{\tau}_1 = \{\boldsymbol{\tau}_{q_B}^T \quad \mathbf{0}_{3\times1}\}^T$). The gravitational vector is represented as $\mathbf{g}_B = \{\mathbf{g}_1^T \quad m_p g l_b c\theta_p s\phi_p \quad m_p g l_b s\theta_p c\phi_p\}^T$ (such that $\mathbf{g}_1 = \{\mathbf{g}_{q_B} \quad -m_p g s\theta \quad m_p g c\theta s\phi \quad m_p g c\theta c\phi\}^T$). The second order differential equation can be represented in state-space form as follows $\dot{\boldsymbol{x}}_s(t) = \mathbf{A}_c \boldsymbol{x}_s(t) + \mathbf{B}_c \mathbf{u}_c(t) + \mathbf{X}_{gc} + \mathbf{F}_d + \mathbf{B}_{Sk}\mathbf{F}_{S2}$, where the state vector is represented by $\boldsymbol{x}_s = \{\dot{\boldsymbol{\eta}}_I^T \quad \boldsymbol{\eta}_I^T\}^T$, the control input vector $\mathbf{u}_c(t) = \{\boldsymbol{\tau}_I^T \quad \mathbf{0}_{11\times1}\}^T$, and the gravitational vector $\mathbf{X}_{gc} = \{-(\mathbf{M}_I^{-1}\mathbf{g}_I)^T \quad \mathbf{0}_{11\times1}\}^T$. The

dynamic ($\mathbf{A}_c$) and input ($\mathbf{B}_c$) matrices are respectively defined by

$$\mathbf{A}_c = \begin{bmatrix} -\mathbf{M}_I^{-1}\mathbf{C}_I & -\mathbf{M}_I^{-1}\boldsymbol{K}_I \\ \mathbf{I}_{11\times11} & \mathbf{0}_{11\times11} \end{bmatrix} \qquad \mathbf{B}_c = \begin{bmatrix} -\mathbf{M}_I^{-1} \\ \mathbf{0}_{11\times11} \end{bmatrix} \tag{56}$$

The constraint force vector is defined in the three axes by $\mathbf{F}_{Sk} = \mathbf{B}_{Sk}\mathbf{F}_{S2}$, such that $\mathbf{F}_{S2} = \{F_{sx}\ F_{sy}\ F_{sz}\}^T$, and it is rewritten as follows

$$\mathbf{F}_{S2} = \{k_p l_b c\phi_p s\theta_p \quad k_p l_b s\phi_p \quad k_p l_b c\phi_p c\theta_p\}^T \tag{57}$$

and $\mathbf{B}_{Sk}$ is vector defined by $\{\mathbf{J}_B\mathbf{M}_B^{-1}\mathbf{B}_{B0}\ \mathbf{0}_{11\times1}\}^T$, where $\mathbf{B}_{B0}$ is represented by

$$\mathbf{B}_{B0} = \begin{bmatrix} \mathbf{B}_{B01}\ \mathbf{0}_{3\times3}\ -\mathbf{B}_{B01}\ \mathbf{0}_{2\times3} \end{bmatrix}^T \tag{58}$$

where $\mathbf{B}_{B01}$=diag(1,1,1). Therefore, a new attachment representation (by constraint forces) has been developed to evaluate the swing and elastic dynamics, in terms of vibration. In contrast to the first configuration (Section 4.1.2), the payload can translate along the three directions and rotation around x and y axes.

5.2   CONTROLLER DESIGN

This section presents the design of an Adaptive Sliding Mode Control (ASMC). The inputs and outputs for altitude, position and attitude angles of the quadrotor are obtained by the Sliding Mode Control methodology. The position and attitude controllers present adaptive rules with the aim to compensate the dynamics of the attached payload. This new strategy enhances significantly the controller performance, allowing to be employed for transporting different types of medicines, including those with sensitive to vibration and those ones dropped during a flight.

In Section 4.3.2, nominal constant coefficients (m_p, Δ_x, Δ_y and Δ_z to U_1, U_2, U_3 and U_4, respectively) are used to design the controller, whereas in this case, adaptive coefficients are chosen to compensate the extra dynamics and attenuate the payload uncertainty, according to the proposed trajectory and payload weight. An adaptive altitude coefficient is designed to compensate for the additional weight of the attached payload. Then, adaptive attitude coefficients are computed to be included on the rotational dynamics. Figure 45 depicts a schematic illustration of the controller design.

Figure 45 – Block diagram describing the closed loop control.
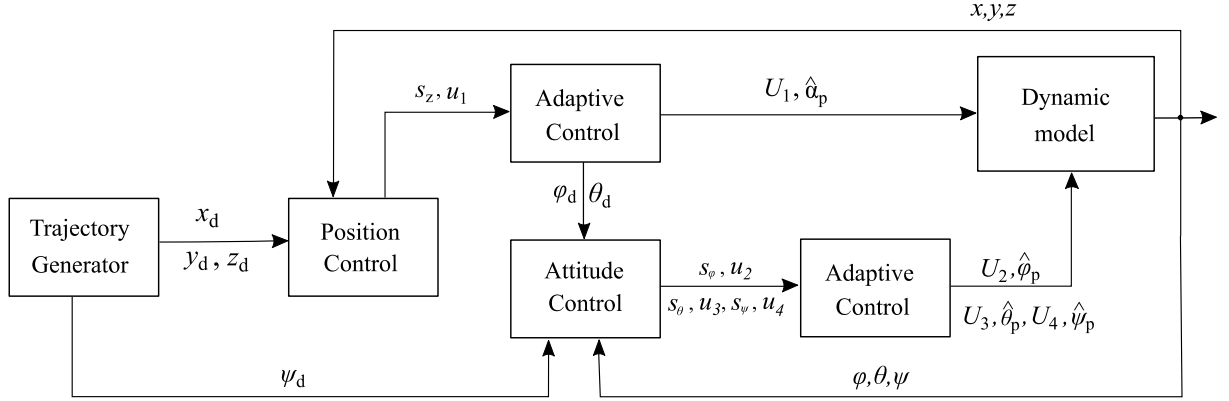
Source: Prepared by the author.

5.2.1 Altitude control design

The sliding surface is represented by the following expression $s_k = \dot{e}_k + \lambda_k e_k$, where s_k, and its derivative with respect to time is given by $\dot{s}_k = \ddot{e}_k + \lambda_k \dot{e}_k$, as seen in Section 4.3.2. According to Utkin (2013), s_k should be a discontinuous state function to improve the controller robustness and reduce the uncertainties influence, such that its derivative can be defined as $\dot{s}_k = -\eta_k s_k - \epsilon_k sat(s_k)$, where the terms ϵ_k and η_k are the sliding surface exponential coefficients (ELHENNAWY; HABIB, 2017). The corresponding control law for the altitude controller is defined by

$$u_1 = \frac{m}{c\theta c\phi}\left(\ddot{z}_d + \lambda_z \dot{e}_z + \frac{k_{dz}}{m}\dot{z} + g - \frac{k_{pz}}{m}z + \frac{k_{pz}}{m}z_p + \frac{k_{pz}}{m}l_b + \eta_z s_z + \epsilon_z sat(s_z)\right) \tag{59}$$

where the saturated function $(sat(s_k))$ is generally chosen to attenuate the chattering effect on the actuators (SLOTINE; LI, 1991). In comparison to the first approach (Section 4.3.2), the elastic and drags effects are included to the altitude controller law. As an under-actuated system, the motion along (x, y) plane is associated with the desired roll and pitch angles (ϕ_d, θ_d). The roll and pitch angles are generated through two virtual inputs, and they are described in Eq. (37) in Section 4.3.2.

Stability Analysis

The following equation is selected to be a Lyapunov candidate function $V_z = \frac{1}{2}s_z^2$. The candidate function V_z must be positive definite with its time derivative be represented by a negative definite function. The Lyapunov candidate is used to analyze the altitude position proof, as described by $\dot{V}_z = s_z \dot{s}_z$. By combining the Lyapunov time derivative function $(\dot{V}_z)$ with the chosen surface $(\dot{s}_k = -\eta_k s_k - \epsilon_k sat(s_k))$ and the vertical motion

equation, the time derivative is expressed as

$$\dot{V}_z = -\eta_z s_z^2 - \epsilon_z |s_z| < 0 \tag{60}$$

where the negative definite derivative of the Lyapunov candidate is a condition that guarantees the asymptotically stability of altitude controller. Similarly, the stability of position and attitude controllers can be proved following the same steps Elhennawy and Habib (2017).

Adaptive Altitude control design

The corresponding control law (u_1) is designed for a quadrotor with no payload. The real mass is then estimated, based on the nominal (m) and a positive constant (α_p), leading to $\hat{m} = \alpha_p m$. The coefficient α_p introduces robustness against the influence of the payload on the dynamics, compensating this additional weight to the proposed control law. By assuming $\tilde{\alpha}_p = \hat{\alpha}_p - \alpha_p$ and using the adaptive control law, the derivative of $\hat{\alpha}_p$ is then obtained by

$$\dot{\hat{\alpha}}_p = \gamma_p s_z u_1 c\phi c\theta / m \tag{61}$$

where γ_p is a positive constant, and the modified control law is computed by $U_1 = \hat{\alpha}_p u_1$. To estimate the adaptive coefficient, a Lyapunov function is defined as $V_p = 0.5 s_z^2 + \tilde{\alpha}_p^2/(2\alpha_p \gamma_p)$, and the time derivative is then expressed as follows

$$\dot{V}_p = s_z \dot{s}_z + \frac{1}{\alpha_p \gamma_p} \tilde{\alpha}_p \dot{\hat{\alpha}}_p \tag{62}$$

Substituting the vertical equation of motion in Eq. (62), the $\dot{V}_p$ is then computed by $\dot{V}_p = s_z(\ddot{z}_d - c\theta c\phi U_1/\hat{m} + (k_{dz}/m)\dot{z} + c_{el} + g + \lambda_z \dot{e}_z) + \frac{1}{\alpha_p \gamma_p} \tilde{\alpha}_p \dot{\hat{\alpha}}_p$. In addition, by using the following relationships $U_1/\hat{m} = \hat{\alpha}_p u_1/(\alpha_p m)$ and $\hat{\alpha}_p = \tilde{\alpha}_p + \alpha_p$, the derivative of Lyapunov $\dot{V}_p$ is defined by

$$\dot{V}_p = s_z(\ddot{z}_d - \tilde{\alpha}_p c\theta c\phi u_1/(\alpha_p m) - u_1 c\theta c\phi/m + (k_{dz}/m)\dot{z} + c_{el} + g + \lambda_z \dot{e}_z) + \frac{1}{\alpha_p \gamma_p} \tilde{\alpha}_p \dot{\hat{\alpha}}_p \tag{63}$$

$$\dot{V}_p = s_z(-\tilde{\alpha}_p c\theta c\phi u_1/(\alpha_p m) - \eta_z s_z - \epsilon_z sat(s_z)) + \frac{1}{\alpha_p \gamma_p} \tilde{\alpha}_p \dot{\hat{\alpha}}_p \tag{64}$$

where $c_{el} = -(k_{pz}/m)z + (k_{pz}/m)z_p$. Since $\dot{V}_p$ must be a non-positive function (as seen $\dot{V}_z = -\eta_z s_z^2 - \epsilon_z |s_z| < 0$), the adaption rule is then obtained, as represented in Eq. (61).

5.2.2 Attitude control design

The attitude control inputs u_2, u_3 and u_4 are obtained by following similar steps, as described for u_1. A sliding surface is chosen, then a discontinuous state function is used to represent the sliding surface, and then the simplified equations for the attitude states are added to the controller design. The corresponding control laws are defined as follows (ELHENNAWY; HABIB, 2017)

$$u_2 = \frac{I_x}{l}\left[\ddot{\phi}_d - \frac{(I_y-I_z)}{I_x}\dot{\theta}\dot{\psi} + \lambda_\phi\dot{e}_\phi + \frac{k_{fx}}{I_x}\dot{\phi} + \frac{J_r\bar{\Omega}}{I_x}\dot{\theta} + \eta_\phi s_\phi + \epsilon_\phi sat(s_\phi)\right]$$

$$u_3 = \frac{I_y}{l}\left[\ddot{\theta}_d - \frac{(I_z-I_x)}{I_y}\dot{\phi}\dot{\psi} + \lambda_\theta\dot{e}_\theta + \frac{k_{fy}}{I_y}\dot{\theta} - \frac{J_r\bar{\Omega}}{I_y}\dot{\theta} + \eta_\theta s_\theta + \epsilon_\theta sat(s_\theta)\right] \qquad (65)$$

$$u_4 = I_z\left[\ddot{\psi}_d - \frac{(I_x-I_y)}{I_z}\dot{\theta}\dot{\phi} + \lambda_\psi\dot{e}_\psi + \frac{k_{fz}}{I_z}\dot{\psi} + \eta_\psi s_\psi + \epsilon_\psi sat(s_\psi)\right]$$

where λ_ϕ, λ_θ, λ_ψ, ϵ_ϕ, ϵ_θ, ϵ_ψ, η_ϕ, η_θ and η_ψ are also positive real constant parameters.

Adaptive Attitude control design

In the attitude control design, an adaptive coefficient is designed to compensate the payload influence on the rotational dynamics. Likewise, to the altitude (as seen in Section 5.2.1), the adaptive coefficients are computed based on Lyapunov's method, as expressed by $\dot{\hat{\beta}}_\phi = \gamma_\phi s_\phi u_2/I_x$, $\dot{\hat{\beta}}_\theta = \gamma_\theta s_\theta u_3/I_y$ and $\dot{\hat{\beta}}_\psi = \gamma_\psi s_\psi u_4/I_z$.

These coefficients are then included to the attitude control to compensate the uncertainties of the payload. Therefore, the attitude control inputs are defined as $U_2 = (1 + \hat{\beta}_\phi)u_2$, $U_3 = (1 + \hat{\beta}_\theta)u_3$ and $U_4 = (1 + \hat{\beta}_\psi)u_4$. Further details regarding the stability proof can be found in Section 5.2.1.

5.3 ELASTIC ATTACHMENT INFLUENCE

The physical parameters of the dynamic model (quadrotor with an attached payload) used for numerical simulations are presented in Table 11. Table 12 lists the controller gains computed for the Sliding Mode Control design. The initial altitude and attitude states of the quadrotor and its payload are designed to have small displacements.

In this section, the comparison between the presence and absence of the elastic dynamics on the UAV have been investigated. UAV displacement, control input and attitude angles are used to compare both situations, highlighting the elastic influence. A

Table 11 – Physical parameters of the quadrotor.

Parameter	Value	Unit	Parameter	Value	Unit
m	2.2	kg	I_x	0.0167	kgm^2
l	0.1725	m	I_y	0.0167	kgm^2
l_b	0.200	m	I_z	0.0231	kgm^2

Source: Prepared by the author.

Table 12 – Controller parameters.

Parameters	Value	Parameters	Value
ϵ_z, η_z, γ	1.80, 0.4, 0.2	ϵ_ϕ, ϵ_θ, ϵ_ψ,	1.50, 1.10, 1.10
λ_x, λ_y, λ_z	3.00, 3.20, 3.20	λ_ϕ, λ_θ, λ_ψ	1.50, 1.50, 1.50
η_ϕ, η_θ, η_ψ	0.04, 0.04, 0.04		

Source: Prepared by the author.

rectangular flight trajectory is composed of take-off and cruise along the x and y directions. Figure 46 depicts the quadrotor and payload three dimensional trajectories. For the dynamic model, the distance between the payload and quadrotor is defined by l_b = 0.2.

Figure 46 – Three-dimensional trajectory of the quadrotor and its payload, showing the desired trajectory (solid red line), quadrotor trajectory (solid blue line), and payload displacement (dashed black line).
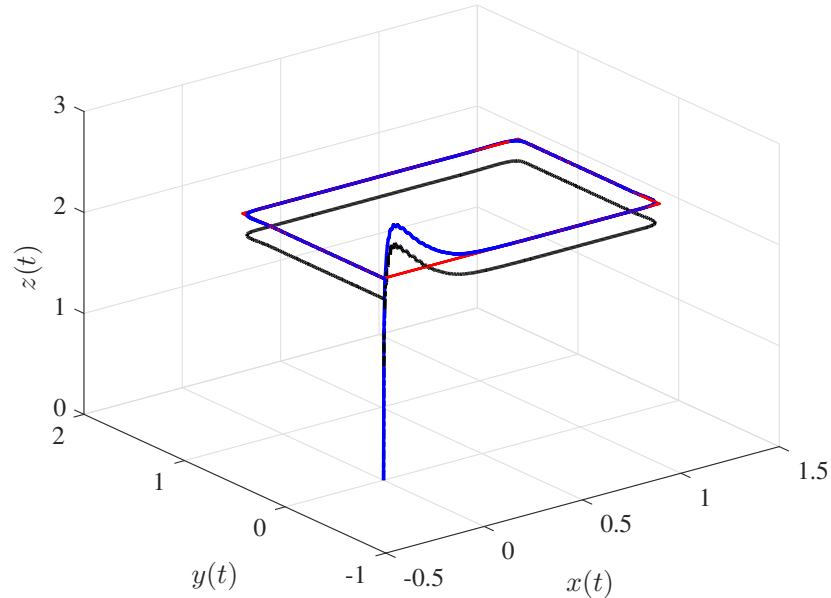
Source: Geronel, Botez and Bueno (2022b).

Figure 46 shows that there is no presence of external disturbances in the trajectory. Especially at the beginning of the flight, higher oscillation peaks are verified due to the rapid change of acceleration and controller characteristics. During the cruise phase, the

SMC attenuates better the residual vibration due to its great robustness to deal with boundary uncertainties.

Figure 47 – Vertical displacement of the quadrotor, showing the elastic (solid blue line) and rigid (solid purple line) attachments.
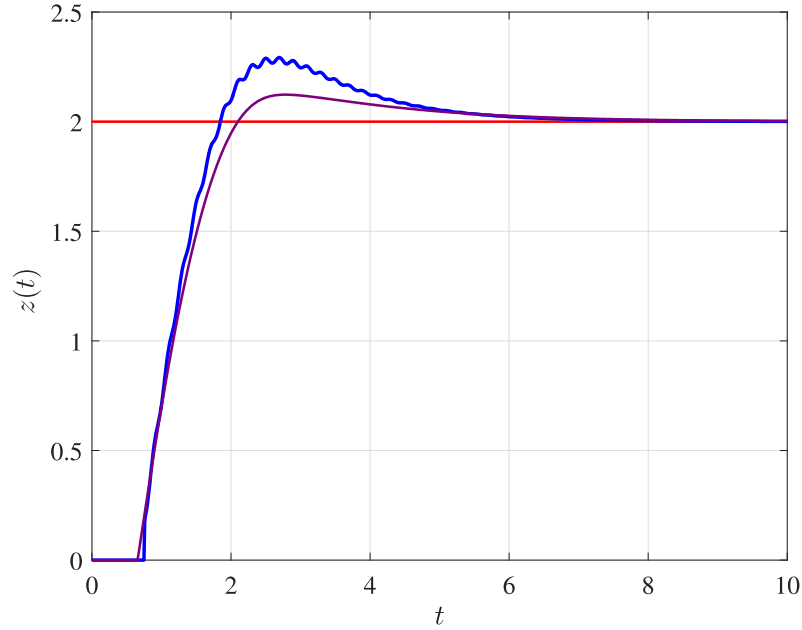
Source: Geronel, Botez and Bueno (2022b).

Figure 48 – Control input U_1, showing the elastic (solid blue line) and rigid (solid purple line) attachments.
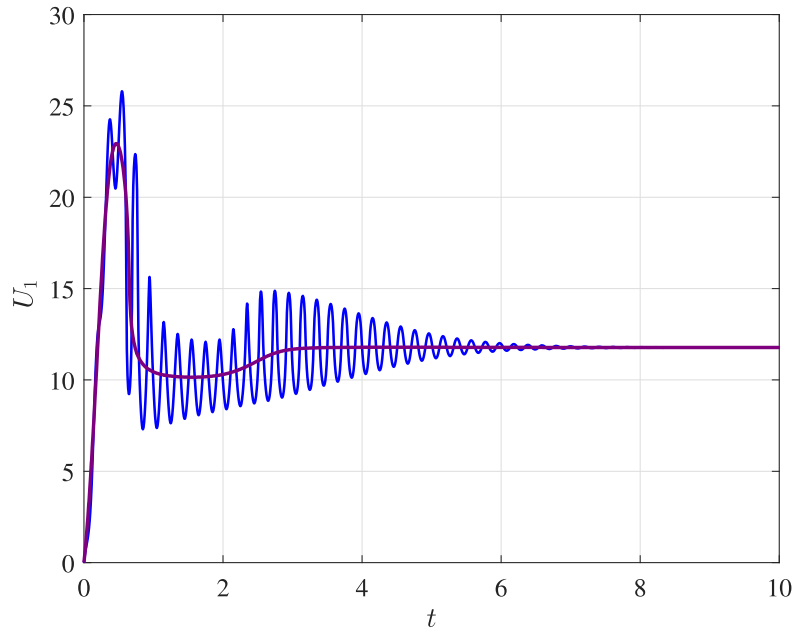
Source: Geronel, Botez and Bueno (2022b).

Initially, a comparison between the dynamics of the elastic and rigid attachment is

investigated. The take-off is analyzed since generally comprises the fastest change of altitude (in comparison to other phases). Scalea *et al.* (2018) have demonstrated that both the take-off and landing phases exhibit significant intensities of vibration in the payload compartment. Additionally, the take-off exhibited a larger period of vibration and higher amplitudes in comparison to the landing phase. Figure 47 shows the vertical displacement comparison between the elastic and rigid attachments on the quadrotor. The rigid attachment does not consider the effects of flexibility, as widely addressed in the literature (KLAUSEN; FOSSEN; JOHANSEN, 2017). Likewise, the control input (U_1), responsible for lifting the quadrotor, suffers the same influence, and Figure 48 shows the control input U_1 for the elastic and rigid attachments.

For simplicity, the elastic influence is shown only in the vertical direction, however, it also extends to the horizontal positions and the attitude angles. Figure 49 shows the roll angles, considering both the elastic and rigid attachment configurations. The undesired oscillation is presented along the trajectory, especially during maneuvers, and its changes of direction.

Figure 49 – Vertical displacement of the quadrotor, showing the elastic (solid blue line) and rigid (solid purple line) attachments.
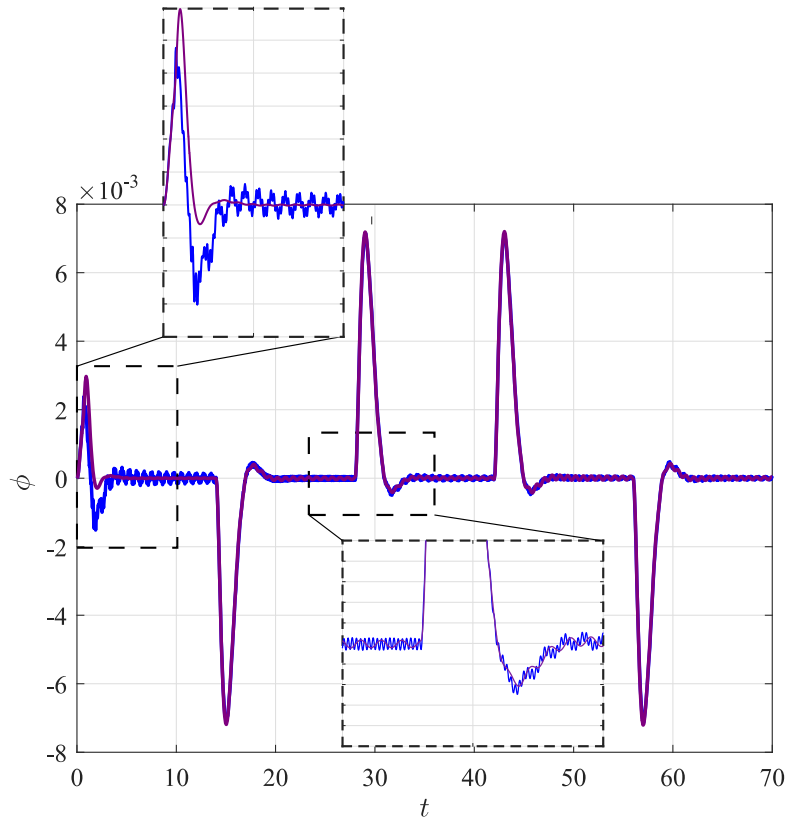
Source: Geronel, Botez and Bueno (2022b).

Figure 49 shows the presence of an undesired oscillation along the attitude state

variable (ϕ), especially related to the take-off ($t < 10$) and lateral motion ($25 < t < 35$). In addition, the amplitude of the swing angles (using elastic attachment) is more than two times higher in comparison to the rigid attachment (see Figure 50). The excessive vibration and lateral motion of the payload alters the quadrotor dynamics and impact on the controller performance. Therefore, the effects of an elastic attachment on the system dynamics must be evaluated to establish the cargo feasibility. The swing-payload dynamics characteristics are depicted in Figure 50 for both attachment configurations.

Figure 50 – Swing payload dynamics, showing the a) elastic attachment (solid blue line) and b) rigid attachment (solid purple line).
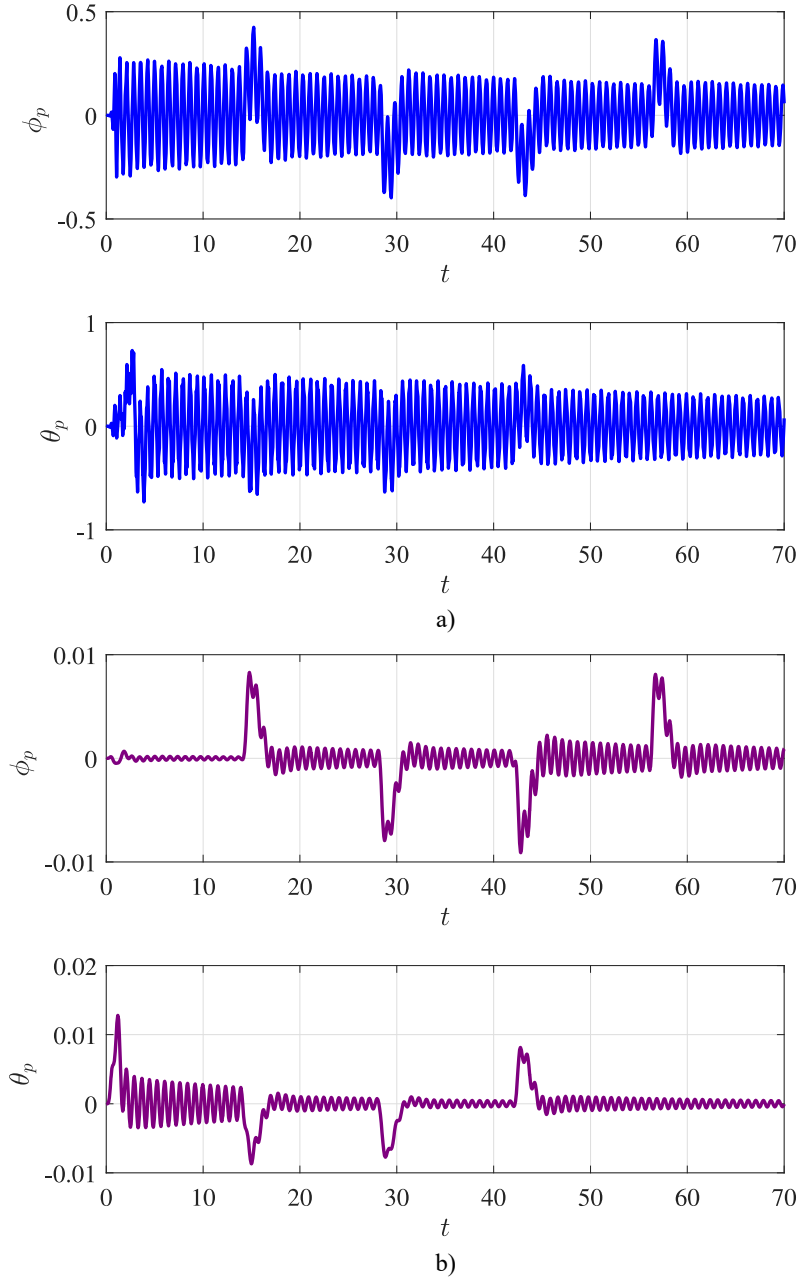
Source: Geronel, Botez and Bueno (2022b).

5.3.1   Vibration characteristics

The vibration characteristics also assessed. These vibrations are calculated using the difference between the payload and the quadrotor's trajectories, as represented by $(j_p - j)$, where $j = x, y, z$. In addition, an external disturbance is applied to the quadrotor during a specific interval of time (limited by the dashed red lines) to simulate the outdoor environment. Both the elastic dynamics and swing dynamics changed in the presence of external disturbances since they are directly impacted. Figure 51 shows the relative displacement between the quadrotor and its payload along the x, y and z axes.

Figure 51 – Relative displacement along a) x, b) y and c) z, showing the desired trajectory (solid red line) and the external disturbances during a time interval (dashed red line).
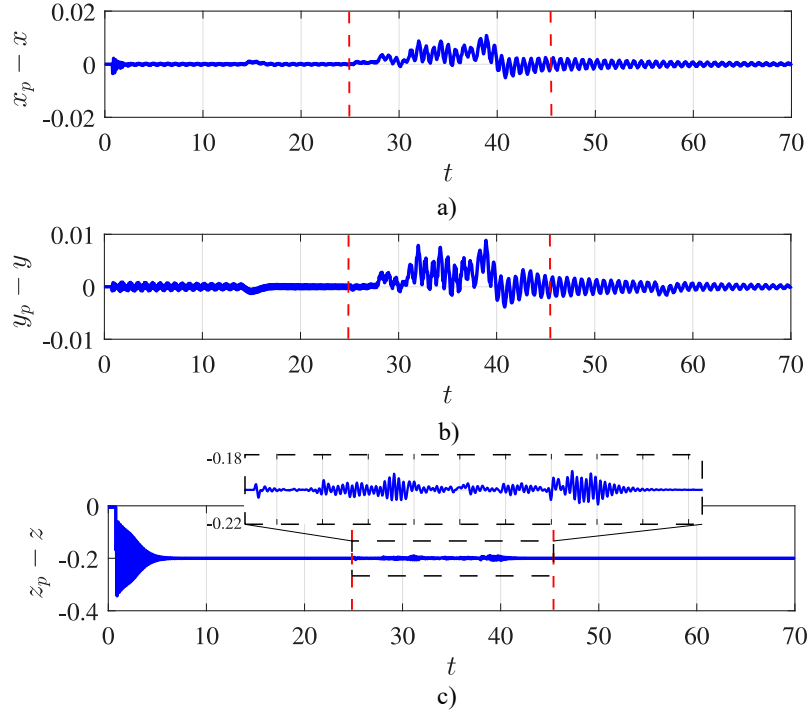
Source: Geronel, Botez and Bueno (2022b).

The Root Mean Square technique is used to verify the level of vibration during the quadrotor flight. The RMS of the relative displacement under external disturbances is approximately 10 times higher than in the absence of this perturbation. For instance, in the x direction, the presence gives values of 0.0037, while the absence 0.0003023. Figure 52 shows the influence of the Dryden disturbance, based on the wind velocity. The index $\bar{\omega}_{wd}$ represents the normalized wind velocity, and $\bar{z}_d$ is the RMS of the quadrotor path under external disturbances (from 25 to 45 seconds).

Based on Figure 52, according to the wind velocity, the payload can suffer higher oscillation amplitudes (in comparison to an indoor flight). Note that the range of

Figure 52 – Relationship between the wind velocity and undesired oscillation.
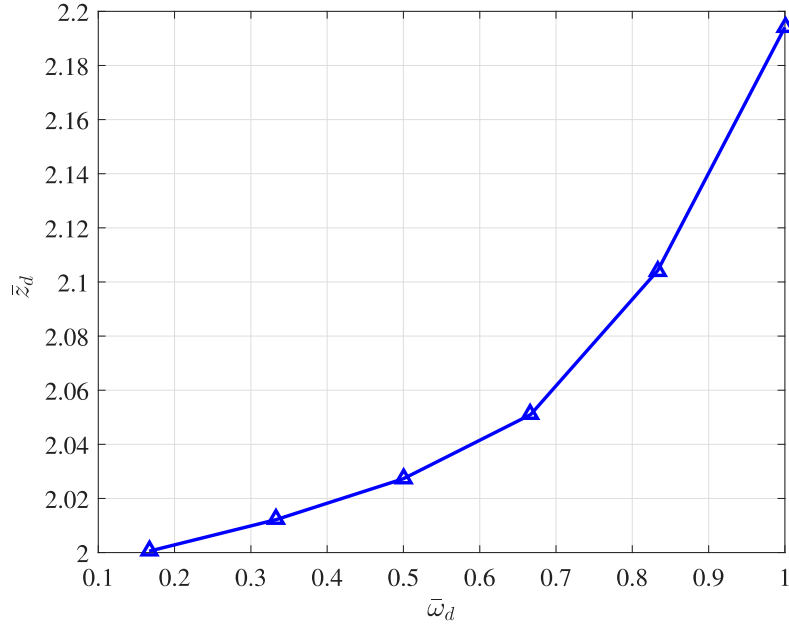
wind velocity used is [0.5 to 3]m/s. Finally, in the presence of severe wind intensity, the controller performance is decreased, and this superior vibration can impact on the transported payload integrity. The RMS is also used to analyze the influence of the attached payload on the quadrotor trajectory performance. Figure 53 shows the relationship between the mass ratio and the RMS of the quadrotor oscillation during the take-off phase. It can be observed that, $\bar{Z}_{RMS}$ represents the Z_{RMS} divided by the natural frequency of the system (as calculated in (GERONEL; DOWELL; BUENO, 2021)), and p_m is the ratio between the payload (m_p) and the quadrotor (m) masses, respectively.

Oakey *et al.* (2021a) have shown that the quadrotor often presents higher vibration than those of traditional road transportation. Each product is affected by a different vibration intensity, and the understanding of this relationship increases the successfully widespread of commercial quadrotors in the medical field. Therefore, depending on the proposed trajectory, attachment configuration and payload weight, several implications can be related to the medicine goods integrity.

Finally, to evaluate the attachment influence, the energy of the take-off (t<10 seconds) and cruise phases is calculated. The payload weight was fixed in 20% of the quadrotor mass, while the stiffness ranged from $0.25k_p$ to $2k_p$ (axis y). Then, the stiffness was fixed in k_p and the payload ranged from $0.25m_p$ to $2m_p$ (axis x). The reference parameters of m_p and k_p are 0.44kg and 361.88 N/m, respectively. Figure 54 shows the normalized energy of each flight phase, by changing the payload weight and attachment value.

Figure 53 – Relationship between the quadrotor weight and trajectory performance during take-off phase.
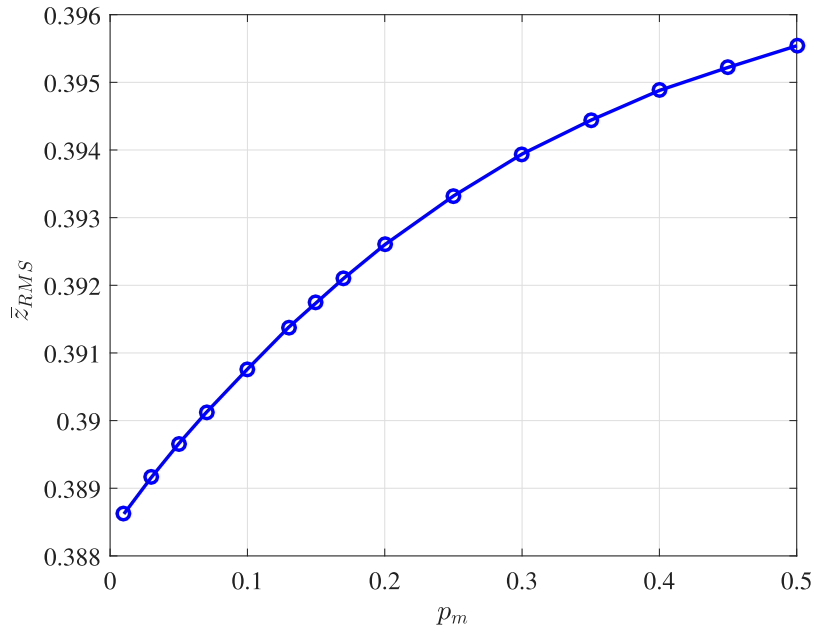
Source: Geronel, Botez and Bueno (2022b).

Figure 54 – Energy calculated by changing the payload weight and stiffness coefficient, where take-off (solid blue line), and cruise (dashed red line) phases.
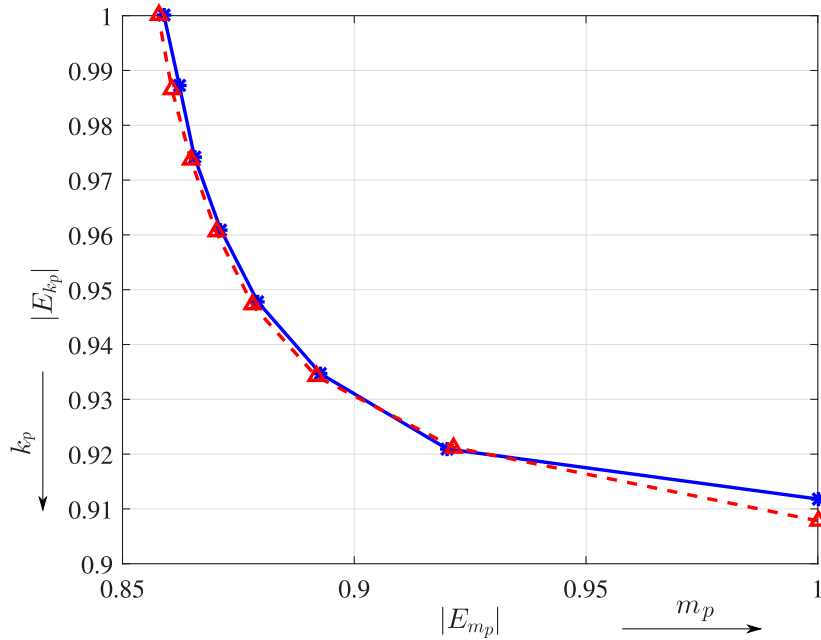
Source: Geronel, Botez and Bueno (2022b).

Figure 54 shows that both the payload weight and stiffness coefficients impact on the unwanted oscillation trajectory. Lower stiffness values increase the undesired vibration ($|E_{(k_p)}|$ closer to 1) as well as higher values of payload weight ($|E_{(m_p)}|$ closer to 1). According to the RMS analysis, the range between m_p to $1.5m_p$ and k_p to $1.5k_p$ exhibits

great performances in terms of energy.

5.4   ADAPTIVE CONTROLLER PERFORMANCE

The UAV dynamics can be negatively impacted due to the payload displacements (GUERRERO-SANCHEZ M.; VALENCIA-PALOMO, 2021; PALUNKO; FIERRO; CRUZ, 2012). Asymmetry, uncertainty and payload vibrations can change the UAV inertia and slows the attitude response (PIZETTA; BRANDAO; SARCINELLI-FILHO, 2015). In the absence of an adaptive controller, the corresponding control law required the previous knowledge of the payload nominal value (GERONEL; BOTEZ; BUENO, 2022a). Instead of defining the altitude control law by $U_1 = \hat{\alpha}_p u_1$, it is previously proposed to consider the sum of mass nominal values $U_1 = (m + m_p)u_1$. Although the adaptive altitude controller $(\hat{\alpha}_p)$ is used to compensate both the controller performance and the payload dynamics, this adaptive coefficient can be computed differently based on the desired trajectory and payload. The use of this adaptive coefficient results in the enhance the attitude response, and consequently decreases the relative trajectory oscillation. Figure 55 depicts the circular trajectory of the quadrotor and its payload, and Figure 56 shows the estimation of the altitude payload coefficient during the flight.

Figure 55 – Three-dimensional circular trajectory configuration of the quadrotor and its payload, showing the desired trajectory (solid red line), quadrotor trajectory (solid blue line), and payload trajectory (dashed black line).
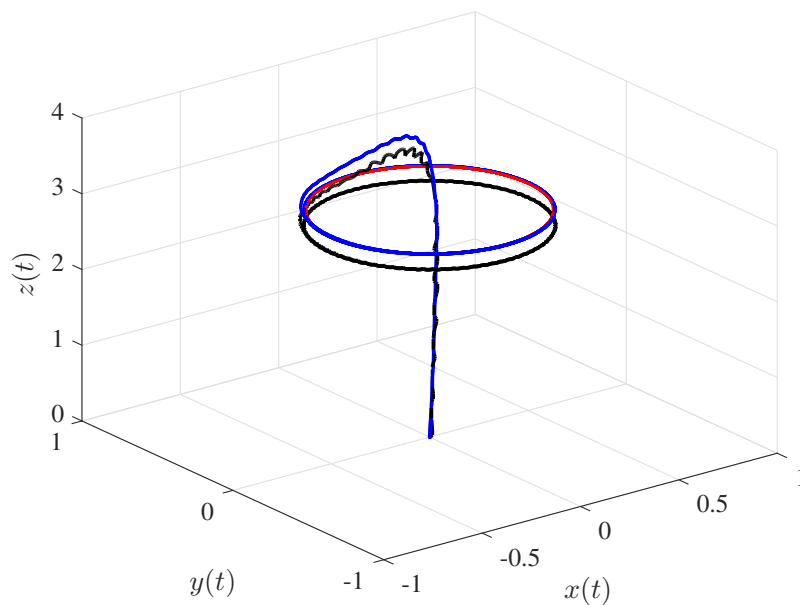
Source: Prepared by the author.

A circular trajectory is used to assess the vibration characteristics in two situations: the presence and absence of the adaptive coefficients on the controller design. Additionally, a physical distance between the quadrotor and its payload is considered to design the mathematical model, which can also be observed in Figure 55 by the blue and black lines. Note that at the beginning of the flight, the trajectories oscillations are amplified (as seen by oscillations in both lines) due to the sudden acceleration and controller behavior.

Figure 56 – Estimation of the altitude adaptive coefficient in time.
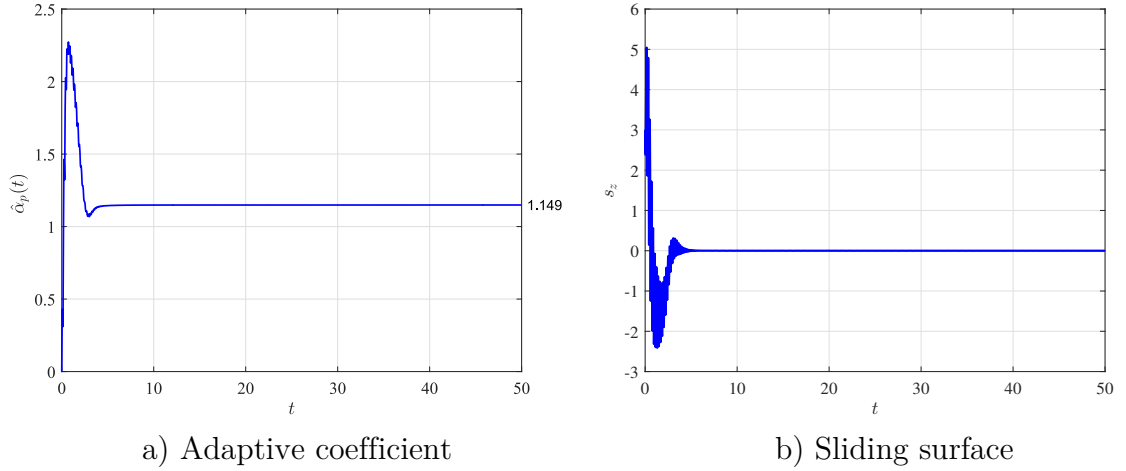

a) Adaptive coefficient   b) Sliding surface

Source: Prepared by the author.

The nominal attached mass corresponds to 15% of the quadrotor weight. Figure 56 shows that the coefficient assumes its nominal value just a few seconds after the beginning of the flight. This estimation behavior is due to the Sliding Mode Control. The SMC works in two steps: first, it guides the convergence to the sliding surface, and then it maintains the state variable on its surface. Note that the surface is reached after approximately 7 seconds, corresponding to the same instant that the adaptive coefficient is successfully estimated. At last, this coefficient is also included in the dynamic matrices, since the normalized payload moments of inertia are defined by $I_i^p = \hat{\alpha}_p I_i$, with the aims to remove the need of the payload nominal value previous knowledge.

The first analysis consider the payload dynamics and the adaptive attitude is not included on the controller design. Unlike Geronel, Botez and Bueno (2022a), the elastic coefficients are then included on the controller development, as seen in Section 5.2.1. The vibration corresponds to the relative trajectory oscillation, i.e. the difference between the quadrotor and its payload trajectories. The vertical and lateral vibration characteristics are then computed by $(z_p - z)$, $(y_p - y)$ and $(x_p - x)$ along z, y and x axes, respectively. Figures 57 and 58 show the minimization of the vibration characteristics due to the inclusion of the elastic influence, in terms of attitude and altitude states.

Figure 57 – Relative trajectory oscillation, showing that the presence of elastic coefficients (solid green line) and the absence of elastic coefficients (solid blue line) on the control law design.

a) Lateral relative trajectory   b) Vertical relative trajectory
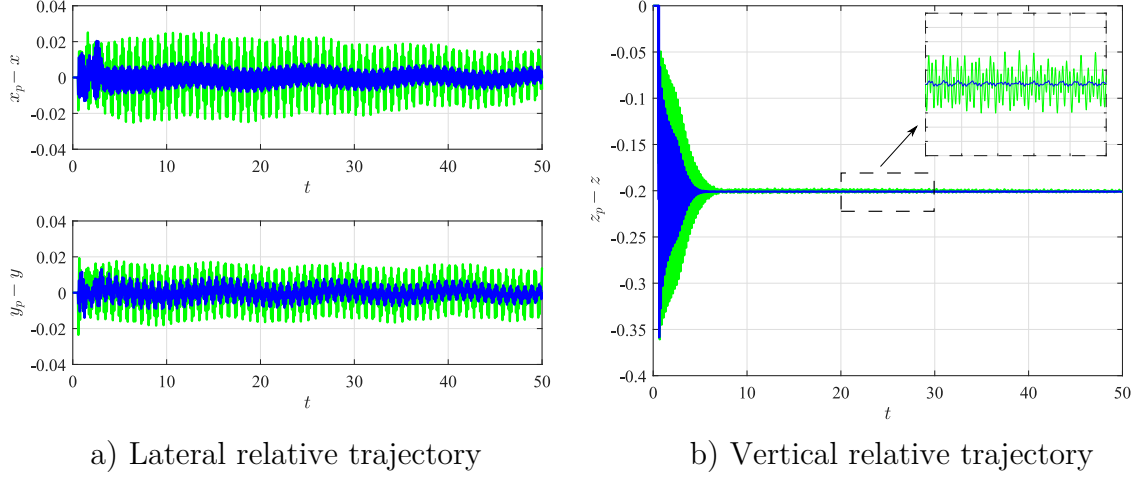
Source: Prepared by the author.

Figure 58 – Attitude angles, showing that the presence of elastic coefficients (solid green line) and the absence of elastic coefficients (solid blue line) on the control law design..

a) Quadrotor's angles   b) Payload's angles
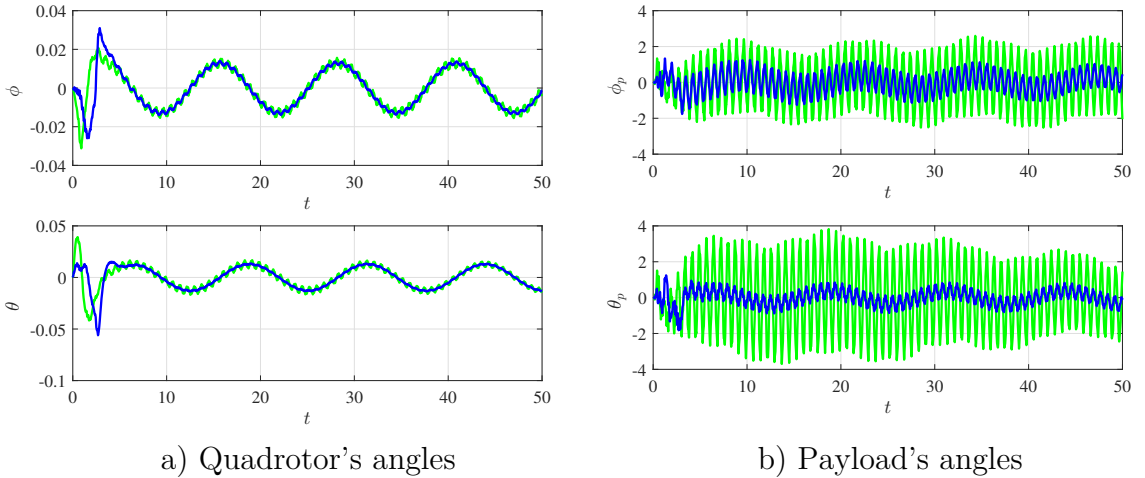
Source: Prepared by the author.

The oscillation behavior for the three axes are significant minimized, in the presence of the elastic effect. This addition acts as a dissipative force, enhancing the controller performance and then reducing the relative trajectory oscillation. This effect is similarly noted, if a discontinuous state function is included on the SMC with the aim to improve the robustness of the control algorithm and reduce the uncertainties influence. Figure 57 shows that if this reduction acts during the whole time, the amplitudes of lateral relative trajectories are approximately constant over the flight. On the other hand, in the vertical direction, the relative trajectory reduction is more prominent at the beginning of the flight (which represents the sudden change of altitude), whereas a positive decrease is also noted

during the cruise phase (as seen by the comparison in the interval range of 20-30 s).

Figure 58 shows that there is also a minimization of the oscillations for both attitude angles. This positive oscillation reduction is crucial for certain applications, including medical delivery, which allows to expand the services of medical products transportation, even those with high sensitivity to vibration. Note that the payload's angles and the amplitudes of oscillations are the half of their initial ones, highlighting the enhance of performance and stability of the aerial aircraft.

5.4.1 Attitude Adaptive Performance

The payload dynamics and attitude adaptive coefficients are considered in this subsection to assess the controller performance. The attitude adaptive coefficients are also designed to compensate for the extra dynamics of the attached mass on rotational motion. An additional term ΔI_w is used to estimate and compensate the payload dynamics on the attitude control laws (GERONEL; BOTEZ; BUENO, 2022a). Likewise in the altitude controller, these adaptive coefficients replace this initial percentage (ΔI_w), by guaranteeing a different value based on the proposed trajectory and maneuvers. Figure 59 depicts the attitude payload coefficients over a quadrotor flight.

Figure 59 – Estimation of the attitude adaptive coefficients for the second trajectory configuration.
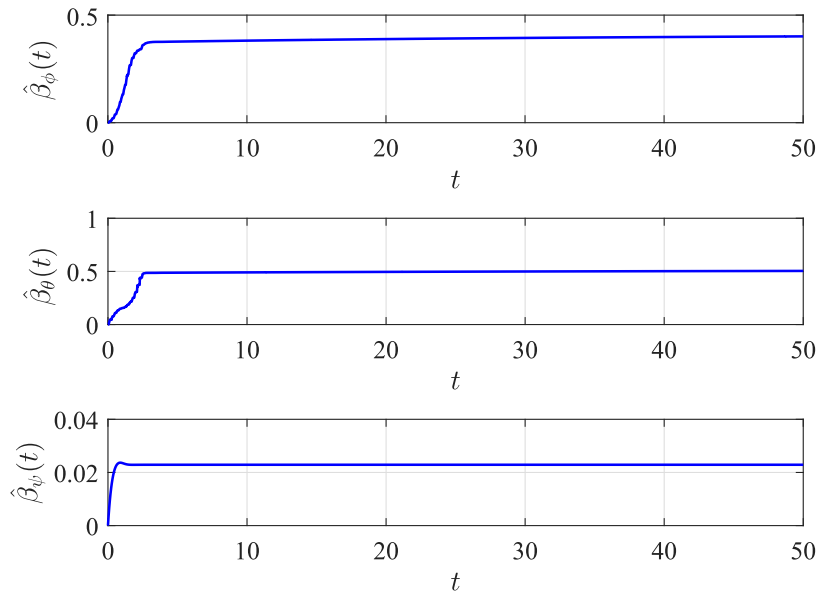
Source: Prepared by the author.

The convergence of attitude coefficients occurs after a few seconds due to the sliding

surface behavior of these states. Figure 60 shows the lateral relative trajectory oscillation in the presence and the absence of the adaptive control.

Figure 60 – Lateral relative displacement oscillations of the quadrotor for the circular trajectory, showing that the presence of the coefficients on the control law design (solid black line) and the absence of the coefficients on the control law design (solid blue line).
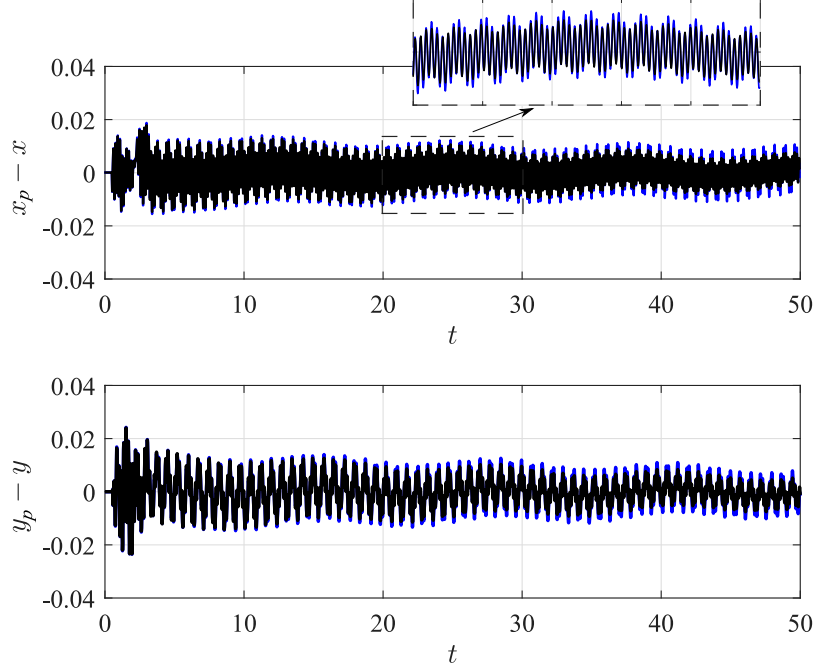
Source: Prepared by the author.

The results have shown the positive reduction of relative trajectory oscillation. The oscillations along the desired reference are significant decreased, especially after 20 seconds. In this sense, they accurately attenuate the effects of payload variations (such as weight) and momentum of inertia. Figure 61 illustrates the payload rotation along x and y axes.

The yaw motion is not assessed in this case, since both quadrotor and its payload motion are assumed to be coincident, as seen in the dynamic model. The Root Mean Square (RMS) is used to evaluate the oscillations (O_{rms}) level, defined by $O_{rms} = \sqrt{\frac{1}{n}(x_1^2 + x_2^2 + ... + x_n^2)}$ where n is the length of a vector, and x_i is each term of the vector. In terms of RMS analysis, the suppression of payload attitude angles present a reduction up to 20%. For instance, in the absence of the coefficients on the controller design, the RMS values of ϕ_p and θ_p are 0.0215 and 0.0149, otherwise they are 0.0172 and 0.0139, respectively.

Figure 61 – Lateral oscillations of the payload for the circular trajectory, showing that the presence of the coefficients on the control law design (solid black line) and the absence of the coefficients on the control law design (solid blue line).

Source: Prepared by the author.

The use of adaptive coefficients are also used to investigate a different trajectory configuration and payload contribution. Figure 62 shows the second rectangular trajectory configuration, and Figure 63 depicts the adaptive coefficients estimation.

Figure 62 – Three-dimensional rectangular trajectory configuration, showing the desired trajectory (solid red line), quadrotor trajectory (solid blue line), and payload trajectory (dashed black line).

Source: Prepared by the author.

Figure 63 – Estimation of the altitude and attitude adaptive coefficients for the second configuration in time.

a) Altiude adaptive coefficient b) Attitude adaptive coefficients

Source: Prepared by the author.

This corresponding trajectory is composed by take-off and cruise phases along x and y directions. Similar to the first configuration, at the beginning of the flight, there is a more significant overshoot due to the adaptive coefficients estimation, as shown in Figure 63. In addition, the convergence of altitude coefficient is reached after a few seconds due to the SMC behavior. In this configuration, a 20% of the payload weight in relation to the quadrotor is reached, highlighting that these coefficients are successfully computed regardless the value of additional mass. Similarly, the attitude coefficients are also estimated based on the additional effort caused by the payload dynamics. In this case, the coefficients $\hat{\beta}_\theta(t)$ and $\hat{\beta}_\phi(t)$ exhibit different values than those ones obtained for the circular configuration, which shows an estimation based on the proposed trajectory. Figure 64 and 65 show lateral relative displacement of the quadrotor and the payload oscillations, respectively.

Figure 64 – Lateral relative displacement oscillations of the quadrotor for the rectangular trajectory, showing that the presence of the coefficients on the control law design (solid black line) and the absence of the coefficients on the control law design (solid blue line).
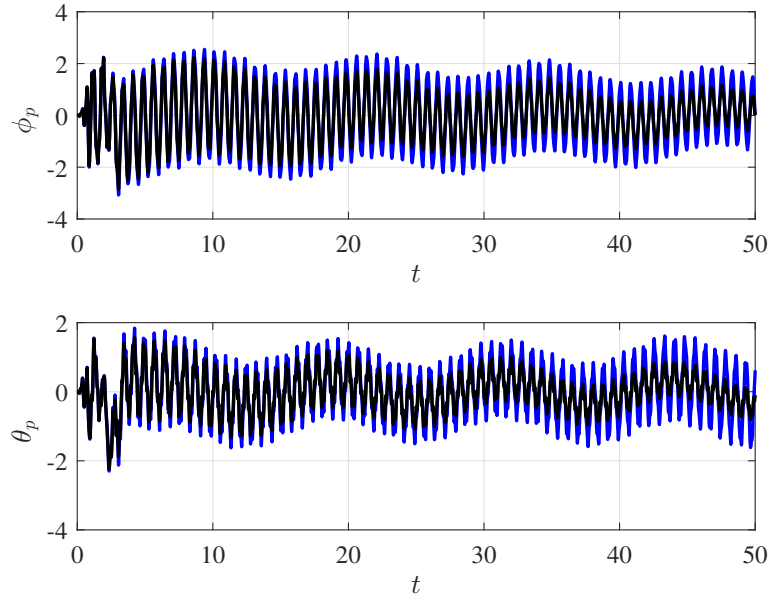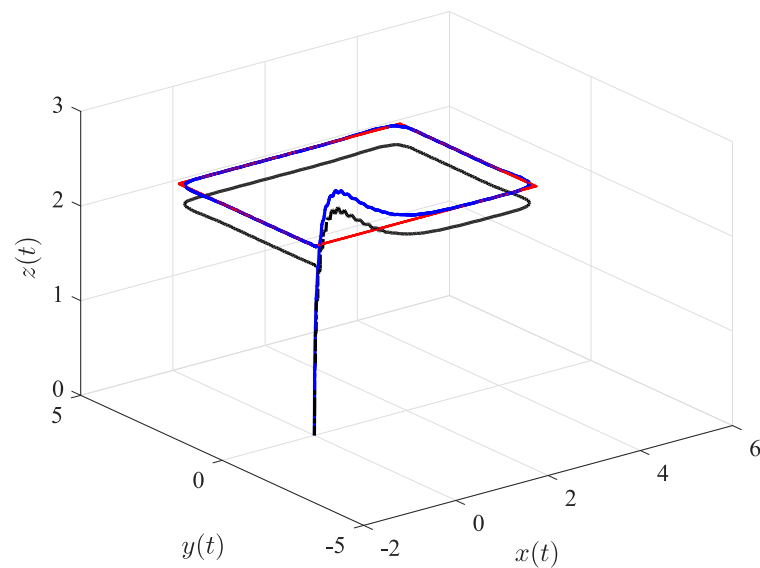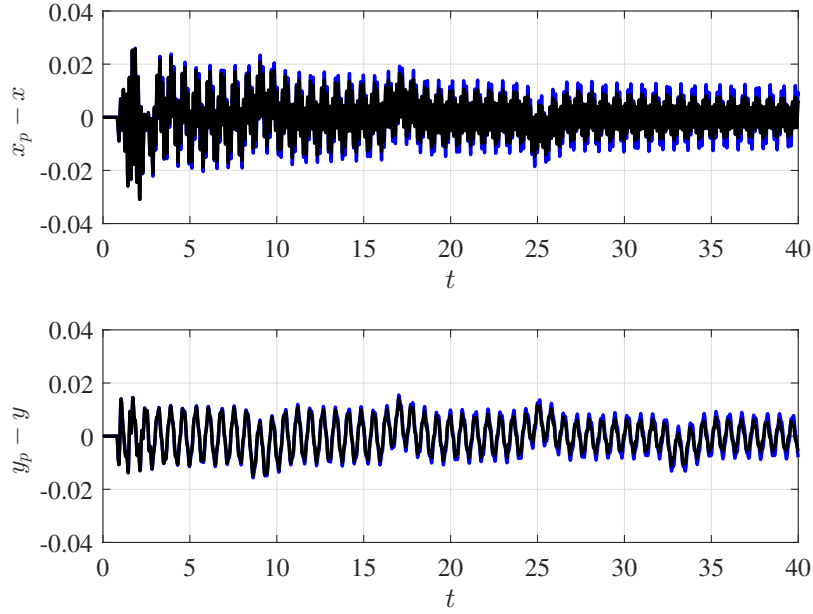

Source: Prepared by the author.

Figure 65 – Lateral oscillations of payload for the circular trajectory, showing that the presence of the coefficients on the control law design (solid black line) and the absence of the coefficients on the control law design (solid blue line).
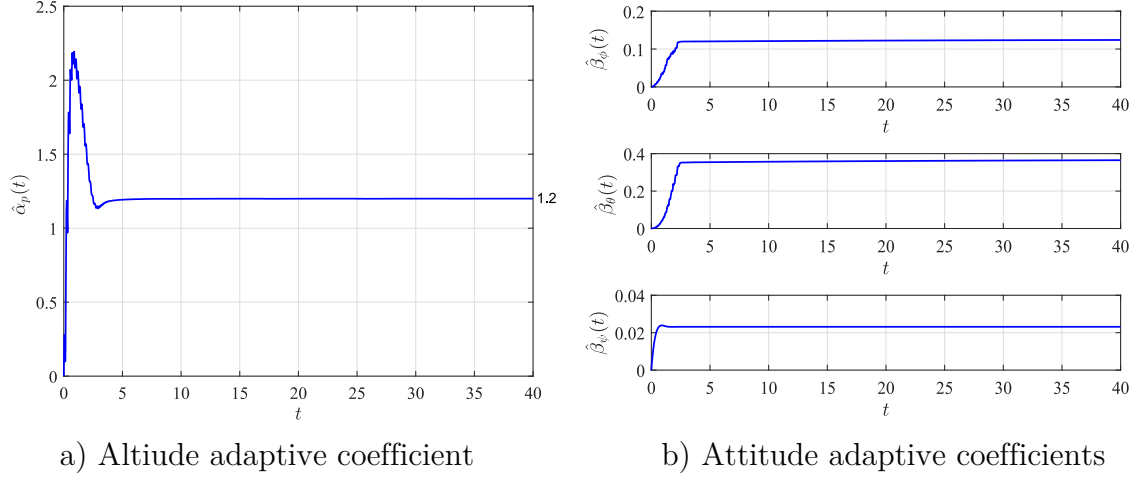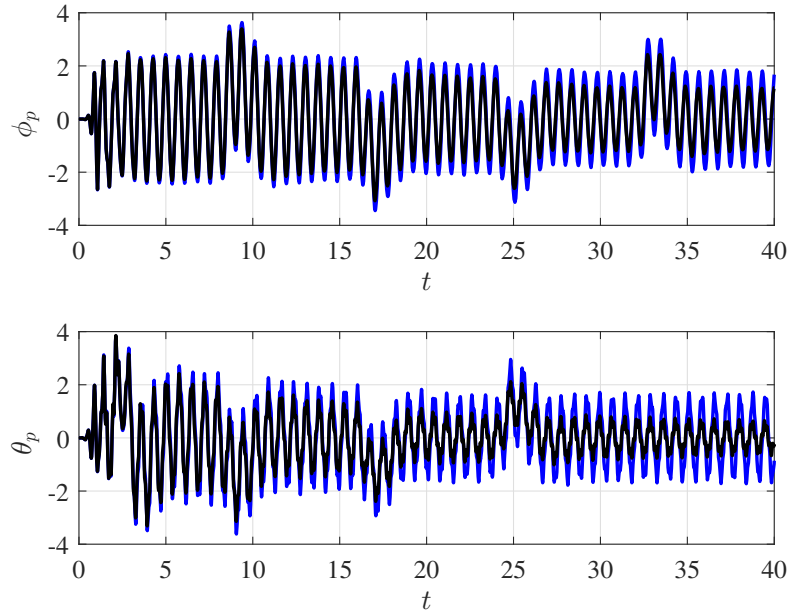

Source: Prepared by the author.

Besides the attenuation caused by the elastic influence on the controller design, the adaptive coefficients enhance even more its performance. Similar to the circular trajectory,

the relative trajectory osculations from the quadrotor and also the payload exhibit a significant attenuation in comparison to the absence of the proposed controller. Table 13 shows the comparison between the presence and absence of the adaptive coefficients. The parameter $\bar{O}_{rms}$ corresponds to the RMS in the absence of these coefficients, and O_{rms} indicates the presence on the controller design. $P_0[\%]$ is a percentage between those previous parameters, and it is defined by $P_0 = 100(\bar{O}_{rms} - O_{rms})/\bar{O}_{rms}$.

Table 13 – RMS comparison for the rectangular trajectory.

Parameter	$x_p - x$	$y_p - y$	ϕ_p	θ_p
$\bar{O}_{rms}$	0.0082	0.0066	0.0535	0.0457
O_{rms}	0.0070	0.0057	0.0452	0.0335
$P_0[\%]$	14.63	13.63	15.51	26.69

Source: Prepared by the author.

Note that there is an improved performance up to 27% for θ_p, and the other states minimize their oscillation around 14%. Therefore, the use of adaptive coefficients on the control design eliminates the need of previous knowledge of the payload dynamics, and thus guaranteeing a positive tracking trajectory. In addition, it allows one to suppress significantly the residual oscillations on the main states variables. Therefore, these adaptive coefficients are estimated according to the proposed trajectory and additional transported mass.

5.4.2   Dropping of Medical products

The dropping of medical products over flight is also investigated. According to commercial UAVs, two main configurations of attachments are considered to transport any cargo: fixed and swing payload. Even though most of the current applications consider fixed configuration, there is a security issue regarding the payload dropping. The quadrotor can be damaged or stolen in case it needs to land on the ground to drop the payload. Thereby, the adaptive coefficients can be used to compensate the variation of payload and thus keep the quadrotor on its initial trajectory.

The influence of involved uncertainties and disturbances can also be estimated by the coefficients, in order to compensate these variable parameters. The uncertainty is associated to a variable payload. It is assumed and additional mass of 20% of the quadrotor ($p_m = 0.2$), and after 20 seconds, the added mass is the half of initial mass (i.e. 10%). Figure 66 illustrates the drop of a medical product. Meanwhile, the trajectory and altitude coefficient are depicted in Figure 67.

Figure 66 – Schematic illustration of the quadrotor dropping a medical product.
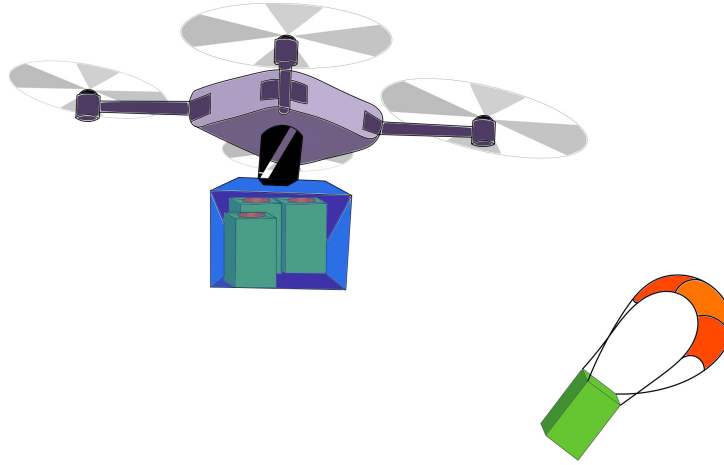
Figure 67 – Controller performance with variable payload.

a) Three-dimensional Trajectory

b) Altitude adaptive coefficient
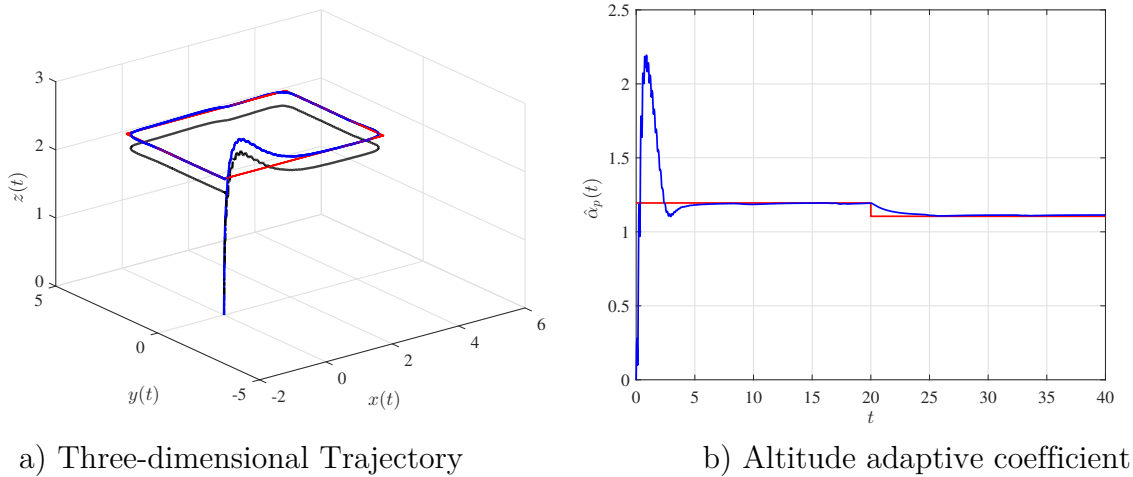
Despite the variable payload, the controller still enables the quadrotor along the desired trajectory. A slight overshot is observed in the middle of the trajectory, when a mass reduction is considered to illustrate a drop of medicine. However, after a few seconds, the original path has been successfully achieved, as seen in Figure 67. Similar, the adaptive coefficient is accordingly estimated to the ratio of mass (p_m).

5.5   FINAL REMARKS

This chapter presents two of the main contributions of this thesis. The use of constraint forces to represent a suspended payload with elastic attachment and the design of an adaptive sliding mode control to reduce payload vibrations influence. The presented

equation of motion considers both the quadrotor and payload dynamics, through the combination of the elastic and the swing-payload dynamics. The complete integration of these dynamics converge the real motion of the quadrotor with an attached payload, which are currently used in the medical field (a compartment attached to the CoG of the quadrotor). This proposed dynamic is used to evaluate the payload vibration characteristics in different scenarios and under external disturbances. The differences between a rigid and elastic attachments, wind velocity, payload weight and controller performance on the quadrotor's flight have been investigated.

The addition of different payload can be modeled like uncertainties to the system, and an Adaptive Sliding Mode Control (ASMC) is proposed to compensate the corresponding uncertainty dynamics. The estimation of the proposed coefficients are obtained to design the ASMC, and the procedure is accomplished using an adaptive method based on Lyapunov theory. The quadrotor control inputs are then designed, and the nominal value does not need to be previously known. According to the proposed trajectory, the use of the adaptive coefficients can reduce the relative trajectory oscillations and attitude angles up to 27%. In addition, the coefficients can be adapted accordingly to the proposed trajectory and payload, even in cases of dropping. These coefficients can be used in change of payload mass, aggressive maneuvers and boundary disturbances. Therefore, the proposed Adaptive Sliding Mode Control can be properly used in different types of payloads and trajectories

6   FINAL REMARKS

This thesis investigate two new dynamic model of a payload with flexible attachment, and they correspond to a restricted motion in the vertical direction and a three dimensional translation combined with rotational motion. These models have been developed to cover most of the current UAVs employed in the medical field and to explore the main vibration effects on the quadrotor and its payload dynamics.

Initially the vibration characteristics were evaluated experimentally. Experimental tests were carried out using four different attachment systems (no payload, fixed, fixed with additional mass and swing load). These proposed attachment systems aim to investigate the level of the vibration of the payload (related to the acceleration along th three main axes) during a flight as well as the influence on the quadrotor dynamics. An amplification of acceleration levels of the payload in relation to the quadrotor was observed for all the considered configurations. This increase was verified in all directions (x, y, z), ranging from about 30% to more than 200%.

In the first dynamic model, a vertical vibrating payload is attached directly to the quadrotor body. In the quasi-loop controller is designed to describe a hand-controlled UAV, and a non-dimensional equation of motion is developed, with the aim to estimate the oscillation of a payload during the flight. These non-dimensional equations are then associated to an equivalent mass-spring system to determine the oscillation of frequency from the masses of the quadrotor and its payload, and the stiffness of fixation. Then, the vibrating frequency can be estimated easily in practical applications in engineering. Regarding the control design by desired trajectory, two conventional controllers are used to assess the payload vibration characteristics in different flight phases and under external disturbances. Performance Indices are used to compare the vibration intensity from both controllers in different situations.

Regarding the second dynamic model, a more comprehensive integration of swing and elastic dynamics have been assessed. The elasticity of an attachment is well known for decreasing the impulsive forces on the payload; however, this effect can enhance the

relative trajectory between the quadrotor and its payload. Then, adaptive coefficients are added to the controller design to compensate for the payload dynamics and reduce the uncertainties. The main advantage of using these adaptive coefficients in the control laws is that there is no need of previous knowledge of the payload dynamics, dimensions and weight. Additionally, in some practical applications with load variations (such as medical cargo's jettisoning), the coefficients can be estimated accordingly to the change of dynamics, i.e. based on the cargo variation. The relative trajectory oscillations and attitude angles are reduced up to 27% in the presence of the adaptive controllers.

6.1   SUGGESTIONS FOR FUTURE WORK

Three different topics are identified as interesting suggestions for future works in this field, and they are presented below

- To investigate the vibration characteristics when considering a flexible UAV and assess their implications on the dynamic of the flight.

- To investigate the influence of payload on the global moment of inertia and its implications on the flight dynamics. Evaluate the differences when considering a payload in different positions.

- To consider an improved tests facilities considering the use of tracking cameras and on-board instrumentation (such as accelerometers) to obtain enhanced controller and UAV dynamic details regarding the experimental tests.

- To design a feedforward control according to the frequency of oscillation of the payload. The strategy aims to anticipate the control signal (according to the frequency of oscillation of the payload) to be used in the design of corresponding control law.

REFERENCES

ABOUDONIA, A.; RASHAD, R.; EL-BADAWY, A. Time domain disturbance observer based control of a quadrotor unmanned aerial vehicle. In: **XXV International Conference on Information, Communication and Automation Technologies (ICAT)**. Sarajevo, Bosnia and Herzegovina: IEEE, 2015. p. 1--6.

ACKERMAN, E.; STRICKLAND, E. Medical delivery drones take flight in east africa. **IEEE Spectrum**, v. 55, n. 1, p. 34--35, 2018.

ALKOMY, H.; SHAN, J. Vibration reduction of a quadrotor with a cable-suspended payload using polynomial trajectories. **Nonlinear Dynamics**, Springer, v. 104, n. 4, p. 3713--3735, 2021.

ALWATEER, M.; LOKE, S. W. Emerging drone services: Challenges and societal issues. **IEEE Technology and Society Magazine**, v. 39, n. 3, p. 47--51, 2020.

AMUKELE, T.; NESS, P. M.; TOBIAN, A. A. R.; BOYD, J.; STREET, J. Drone transportation of blood products. **Transfusion**, v. 57, n. 3, p. 582--588, 2017. Available from: https://onlinelibrary.wiley.com/doi/abs/10.1111/trf.13900.

AMUKELE, T. K.; HERNANDEZ, J.; SNOZEK, C. L. H.; WYATT, R. G.; DOUGLAS, M.; AMINI, R.; STREET, J. Drone transport of chemistry and hematology samples over long distances. **American journal of clinical pathology**, Oxford University Press US, v. 148, n. 5, p. 427--435, 2017.

AURAMBOUT, J. P.; GKOUMAS, K.; CIUFFO, B. Last mile delivery by drones: An estimation of viable market potential and access to citizens across european cities. **European Transport Research Review**, Springer, v. 11, n. 1, p. 1--21, 2019.

BECK, S.; BUI, T. T.; DAVIES, A.; COURTNEY, P.; BROWN, A.; GEUDENS, J.; ROYALL, P. G. An evaluation of the drone delivery of adrenaline auto-injectors for anaphylaxis: Pharmacists: Perceptions, acceptance, and concerns. **Drones**, v. 4, n. 4, p. 1--22, 2020. ISSN 2504-446X. Available from: https://www.mdpi.com/2504-446X/4/4/66.

BEHZAD, S.; MAJDEDDIN, N.; IMAN, I. Cooperative load transportation using multiple uavs. **Aerospace Science and Technology**, v. 84, p. 158--169, 2019. ISSN 1270-9638. Available from: https://www.sciencedirect.com/science/article/pii/S1270963817306697.

BETÉ, T. S.; STORÓPOLI, J. E.; RAMOS, H. R.; CONTI, D. M.; QUARESMA, C. C.; OLIVEIRA, E. A. A. Q. Comparative analysis of unmanned aircraft regulations for the development of startups. **Journal of technology management & innovation**, SciELO Chile, v. 16, n. 2, p. 41--55, 2021.

CARBAJA, F.; BADILLO, H.; OLVERA, R.; CONTRERAS, A.; GONZALEZ, A.; GARCIA, I. L. On active vibration absorption in motion control of a quadrotor uav. **Mathematics**, v. 10, n. 2, p. 1--25, 2022. ISSN 2227-7390. Available from: https://www.mdpi.com/2227-7390/10/2/235.

CASTILLO-ZAMORA, J. J.; CAMARILLO-GOMEZ, K. A.; PEREZ-SOTO, G. I.; RODRIGUEZ-RESENDIZ, J. Comparison of pd, pid and sliding-mode position controllers for vñtail quadcopter stability. **IEEE Access**, v. 6, p. 38086--38096, 2018.

CICHOSZ, M. Logistics startups and logistics service providers: Competitors or partners in exploration? In: SPRINGER. **TranSopot Conference**. Vienna , Austria, 2019. p. 1--11.

CLAESSON, A.; FREDMAN, D.; SVENSSON L .AND RINGH, M.; HOLLENBERG, J.; NORDBERG, P.; ROSENQVIST, M.; DJARV, T.; ÖSTERBERG, S.; LENNARTSSON, J. *et al.* Unmanned aerial vehicles (drones) in out-of-hospital-cardiac-arrest. **Scandinavian journal of trauma, resuscitation and emergency medicine**, BioMed Central, v. 24, n. 1, p. 1--9, 2016.

CLARKE, R. The regulation of civilian drones' impacts on behavioural privacy. **Computer Law & Security Review**, v. 30, n. 3, p. 286--305, 2014. ISSN 0267-3649. Available from: https://www.sciencedirect.com/science/article/pii/S0267364914000570.

CORNELIUS, A. T.; JOHNATHON, M. A.; SCOTT, P. Z.; DONALD, H. J. Use of unmanned aerial vehicles for medical product transport. **Air Medical Journal**, v. 34, n. 2, p. 104--108, 2015. ISSN 1067-991X. Available from: https://www.sciencedirect.com/science/article/pii/S1067991X14003332.

DORF, R. C.; BISHOP, R. H. **Modern Control Systems**. United States of America: Pearson, 2011.

DUFEK, J.; TRAORE, S.; SWANSON, C.; FIPPS, G.; MURPHY, R. Preventing irrigation canal breaches using small unmanned aerial system with multispectral payload. In: **2019 IEEE International Symposium on Safety, Security, and Rescue Robotics (SSRR)**. W¸rzburg, Bavaria/Germany: IEEE, 2019. p. 133--138.

ELHENNAWY, A. M.; HABIB, M. K. Trajectory tracking of a quadcopter flying vehicle using sliding mode control. In: **IECON 2017 - 43rd Annual Conference of the IEEE Industrial Electronics Society**. Beijing, China: IEEE, 2017. p. 6264--6269.

FARAMONDI, L.; OLIVA, G.; ARDITO, L.; CRESCENZI, A.; CARICATO, M.; TESEI, M.; MUDA, A. O.; SETOLA, R. Use of drone to improve healthcare efficiency and sustainability. In: **43rd International Convention on Information, Communication and Electronic Technology (MIPRO)**. Opatija, Croatia: IEEE, 2020. p. 1783--1788.

FATEHI, M. H.; EGHTESAD, M.; AMJADIFARD, R. Modelling and control of an overhead crane system with a flexible cable and large swing angle. **Journal of Low Frequency Noise, Vibration and Active Control**, v. 33, n. 4, p. 395--409, 2014. Available from: https://doi.org/10.1260/0263-0923.33.4.395.

FOSSEN, T. I. **Guidance and control of ocean vehicles**. West Sussex, England: Jhon Wiley and Sons Ltda, 1994.

GATTESCHI, V.; LAMBERTI, F.; PARAVATI, G.; SANNA, A.; DEMARTINI, C.; LISANTI, A.; VENEZIA, G. New frontiers of delivery services using drones: A prototype system exploiting a quadcopter for autonomous drug shipments. In: **2015 IEEE 39th Annual Computer Software and Applications Conference**. Taichung, Taiwan: IEEE Computer Society, 2015. v. 2, p. 920--927.

GERONEL, R. S.; BEGNINI, R. G.; BOTEZ, R. M.; BUENO, D. D. An overview on the use of unmanned aerial vehicles for medical product transportation: fight dynamics and vibration issues. **Journal of the Brazilian Society of Mechanical Sciences and Engineering**, v. 44, p. 1--18, 2022.

GERONEL, R. S.; BOTEZ, R. M.; BUENO, D. D. Vibration analysis of a quadcopter carrying a payload. In: **COBEM, 26th International Congress of Mechanical Engineering**. Virtual Conference: ABCM, 2021. p. 1--9.

GERONEL, R. S.; BOTEZ, R. M.; BUENO, D. D. Dynamic responses due to the dryden gust of an autonomous quadrotor uav carrying a payload. **The Aeronautical Journal**, Cambridge University Press, p. 1--23, 2022.

GERONEL, R. S.; BOTEZ, R. M.; BUENO, D. D. On the effect of flexibility on the dynamics of a suspended payload carried by a quadrotor. **Designs**, v. 6, n. 2, p. 1--28, 2022. ISSN 2411-9660. Available from: https://www.mdpi.com/2411-9660/6/2/31.

GERONEL, R. S.; BOTEZ, R. M.; BUENO, D. D. The use of polynomial trajectory for vibration reduction of a payload carried by a quadrotor. In: **Workshop PPGEM**. Ilha Solteira: Unesp, 2022.

GERONEL, R. S.; BOTEZ, R. M.; BUENO, D. D. The use of state feedback control based on lmi to suppress oscillations of payload carried by uav. In: **International Symposium on Unmanned Systems and the Defense Industry 2022**. Hybrid:Madrid/Spain and Virtual Conference: SARES, 2022. p. 1--5.

GERONEL, R. S.; BOTEZ, R. M.; BUENO, D. D. A vibration suppression for payloads attached to an uav based on sma springs. In: **AIAA SCITECH 2023 Forum**. National Harbor / MD and Online: ARC, 2023. p. 1042.

GERONEL, R. S.; BUENO, D. D. Trajectory tracking of a quadcopter with an attached payload mass under external disturbances. In: **14th IEEE International Conference on Industry Applications (INDUSCON)**. Sao Paulo, Brazil, 15-18 of August: IEEE Conference Publication, 2021. p. 1288--1295.

GERONEL, R. S.; BUENO, D. D.; BOTEZ, R. M. Vibration analysis of a payload connected to quadrotor-type uav by sma spring. In: **AIAA SCITECH 2022 Forum**. San Diego/California: ARC, 2022. p. 1042.

GERONEL, R. S.; DOWELL, E. H.; BUENO, D. D. Estimating the oscillation frequency of a payload mass on quadcopter in non-autonomous flight. **Journal of Vibration and Control**, v. 2021, n. 0, p. 10775463211046699, 2021. Available from: https://doi.org/10.1177/1077546321104699.

GOVINDARAJAN, B.; SRIDHARAN, A. Conceptual sizing of vertical lift package delivery platforms. **Journal of Aircraft**, v. 57, n. 6, p. 1170--1188, 2020. Available from: https://doi.org/10.2514/1.C035805.

GUERRERO-SANCHEZ M., L. R. C. P. H.-G. O. G.-B. C.; VALENCIA-PALOMO, G. Nonlinear control strategies for a uav carrying a load with swing attenuation. **Applied Mathematical Modelling**, v. 91, p. 709--722, 2021. ISSN 0307-904X. Available from: https://www.sciencedirect.com/science/article/pii/S0307904X20305473.

GUPTA, A.; AFRIN, T.; SCULLY, E.; YODO, N. Advances of uavs toward future transportation: The state-of-the-art, challenges, and opportunities. **Future Transportation**, v. 1, n. 2, p. 326--350, 2021. ISSN 2673-7590. Available from: https://www.mdpi.com/2673-7590/1/2/19.

HAIDARI, L. A.; BROWN, S. T.; FERGUSON, M.; BANCROFT, E.; SPIKER, M.; WILCOX, A.; AMBIKAPATHI, R.; SAMPATH, V.; CONNOR, D. L.; YEE, B. L. The economic and operational value of using drones to transport vaccines. **Vaccine**, v. 34, n. 34, p. 4062--4067, 2016. ISSN 0264-410X. Available from: https://www.sciencedirect.com/science/article/pii/S0264410X16304352.

HAMPSON, M. Drone delivers human kidney: The organ was flown several kilometers by a drone without incurring damage - [news]. **IEEE Spectrum**, v. 56, n. 1, p. 7--9, 2019.

HII, M. S. Y.; COURTNEY, P.; ROYALL, P. G. An evaluation of the delivery of medicines using drones. **Drones**, v. 3, n. 3, p. 1--20, 2019. ISSN 2504-446X. Available from: https://www.mdpi.com/2504-446X/3/3/52.

HROVATIN, D.; ZEMVA, A. Exploiting solar energy during an aerial mapping mission on a lightweight uav. **Electronics**, v. 10, n. 22, p. 1--21, 2021. ISSN 2079-9292. Available from: https://www.mdpi.com/2079-9292/10/22/2876.

HUANG, K.; SHAO, K.; ZHEN, S.; SUN, H.; YU, R. A novel approach for trajectory tracking control of an under-actuated quad-rotor uav. **IEEE/CAA Journal of Automatica Sinica**, p. 1--10, 2016.

JOHANNESSEN, K. A.; WEAR, N. K. S.; TOSKA, K.; HANSB⁻, M.; BERG, J. P.; FOSSE, E. Pathologic blood samples tolerate exposure to vibration and high turbulence in simulated drone flights, but plasma samples should be centrifuged after flight. **IEEE Journal of Translational Engineering in Health and Medicine**, v. 9, p. 1--10, 2021.

JOHNSON, A. M.; CUNNINGHAM, C. J.; ARNOLD, E.; ROSAMOND, W. D.; ZÈGRE-HEMSEY, J. K. Impact of using drones in emergency medicine: What does the future hold? **Open Access Emergency Medicine: OAEM**, Dove Press, v. 13, p. 487, 2021.

JR, J. B. R.; PARKER, B. C.; VIGNESH, V. Medical applications of drones for disaster relief: A review of the literature. **Surgical technology international**, v. 33, p. 17--22, 2018.

JU, C.; SON, H. I. Multiple uav systems for agricultural applications: Control, implementation, and evaluation. **Electronics**, v. 7, n. 9, p. 1--19, 2018. ISSN 2079-9292. Available from: https://www.mdpi.com/2079-9292/7/9/162.

KAVIRI, S.; TAHSIRI, A.; TAGHIRAD, H. D. A cooperative control framework of multiple unmanned aerial vehicles for dynamic oil spill cleanup. **Journal of the Brazilian Society of Mechanical Sciences and Engineering**, Springer, v. 43, n. 6, p. 1--17, 2021.

KEDADOUCHE, M.; YULAN, S.; LIU, Z.; THOMAS, M.; CHARLAND-ARCAND, G.; BECK, A. Design of a vibration isolator for the inertial navigation system of an autopilot dedicated to the operation of light drones. In: IEEE. **2018 9th International Conference on Mechanical and Aerospace Engineering (ICMAE)**. Budapest, Hungary, 2018. p. 73--78.

KEEFFE, D. T.; JOHNSON, K.; MARAKA, S. Or30-04 autonomous drone delivery of insulin. **Journal of the Endocrine Society**, Oxford University Press US, v. 4, n. Supplement_1, p. OR30--04, 2020.

KIM, J.; KANG, M. S.; PARK, S. Accurate modeling and robust hovering control for a quad-rotor vtol aircraft. In: **Selected papers from the 2nd International Symposium on UAVs**. Reno, Nevada, USA June 8-10, 2009: Springer, 2009. p. 9--26.

KIM, J.; KIM, S.; JU, C.; SON, H. I. Unmanned aerial vehicles in agriculture: A review of perspective of platform, control, and applications. **IEEE Access**, v. 7, p. 105100--105115, 2019.

KLAUSEN, K.; FOSSEN, T. I.; JOHANSEN, T. A. Nonlinear control of a multirotor uav with suspended load. In: **2015 International Conference on Unmanned Aircraft Systems (ICUAS)**. Denver - USA: IEEE, 2015. p. 176--184.

KLAUSEN, K.; FOSSEN, T. I.; JOHANSEN, T. A. Nonlinear control with swing damping of a multirotor uav with suspended load. **Journal of Intelligent & Robotic Systems**, Springer, v. 88, n. 2, p. 379--394, 2017.

KONERT, A.; SMEREKA, J.; SZARPAK, L. The use of drones in emergency medicine: practical and legal aspects. **Emergency medicine international**, Hindawi, v. 2019, p. 1--6, 2019. Available from: https://doi.org/10.1155/2019/3589792.

KOZIOŁ, A.; SOBCZYK, A. Usage of unmanned aerial vehicles in medical services: A review. **Materials Research Proceedings**, Materials Research Forum LLC, v. 24, p. 288--293, 2022.

KREY, M. Drones: Application and business models in swiss hospitals. In: UNIVERSITY OF HAWAI'I AT MANOA. **51st Hawaii International Conference on System Sciences (HICSS)**. Waikoloa Village HI, USA, 3-6 January 2019, 2018. p. 3081--3089.

KUSZNIR, T.; SMOCZEK, J. Sliding mode-based control of a uav quadrotor for suppressing the cable-suspended payload vibration. **Journal of Control Science and Engineering**, Hindawi, v. 2020, p. 1--12, 2020.

LIMA, G. V. **Modelagem Dinamica e Controle para Navegacao de um Veiculo Aereo nao Tripulado do tipo Quadricoptero**. Thesis (Ph. D.) --- Universidade Federal de Uberlandia, 2015.

LIN, M.; CHEN, Y.; HAN, R.; CHEN, Y. Discrete optimization on truck-drone collaborative transportation system for delivering medical resources. **Discrete Dynamics in Nature and Society**, Hindawi, v. 2022, p. 1--13, 2022.

LING, G.; DRAGHIC, N. Aerial drones for blood delivery. **Transfusion**, Wiley Online Library, v. 59, n. S2, p. 1608--1611, 2019.

LV, T.; YANG, Y.; CHAI, L. Extended state observer based mpc for a quadrotor helicopter subject to wind disturbances. In: **2019 Chinese Control Conference (CCC)**. Guangzhou, China: IEEE, 2019. p. 8206--8211.

MALIK, R.; ROY, I. Probing the mechanism of insulin aggregation during agitation. **International Journal of Pharmaceutics**, v. 413, n. 1, p. 73--80, 2011. ISSN 0378-5173. Available from: https://www.sciencedirect.com/science/article/pii/S0378517311003516.

MION, F. U. Flying drones to exchange lab samples: Service innovation by the swiss multisite hospital eoc. In: _____. **Service Design and Service Thinking in Healthcare and Hospital Management: Theory, Concepts, Practice**. Cham: Springer International Publishing, 2019. p. 463--479. ISBN 978-3-030-00749-2. Available from: https://doi.org/10.1007/978-3-030-00749-2_26.

MOGILI, R. U.; DEEPAK, B. B. V. L. Review on application of drone systems in precision agriculture. **Procedia Computer Science**, v. 133, p. 502--509, 2018. ISSN 1877-0509. Available from: https://www.sciencedirect.com/science/article/pii/S1877050918310081.

OAKEY, A.; WATER, T.; ZHU, W.; ROYALL, P.; CHERRETT, T.; COURTNEY, P.; MAJOE, D.; JELEV, N. Quantifying the effects of vibration on medicines in transit caused by fixed-wing and multi-copter drones. **Drones**, v. 5, n. 1, p. 1--22, 2021. ISSN 2504-446X. Available from: https://www.mdpi.com/2504-446X/5/1/22.

OAKEY, A.; WATERS, T.; ZHU, W.; ROYALL, P. G.; CHERRETT, T.; COURTNEY, P.; MAJOE, D.; JELEV, N. Quantifying the effects of vibration on medicines in transit caused by fixed-wing and multi-copter drones. **Drones**, v. 5, n. 1, p. 1--22, 2021. ISSN 2504-446X. Available from: https://www.mdpi.com/2504-446X/5/1/22.

PALUNKO, I.; FIERRO, R.; CRUZ, P. Trajectory generation for swing-free maneuvers of a quadrotor with suspended payload: A dynamic programming approach. In: **2012 IEEE International Conference on Robotics and Automation**. Saint Paul, MN, USA: IEEE, 2012. p. 2691--2697.

PHAN, C.; LIU, H. Dynamic mapping of forest fire fronts using multiple unmanned aerial vehicles. In: **AIAA Guidance, Navigation, and Control Conference**. Toronto/Canada: ARC, 2010. p. 8317.

PIZETTA, I. H. B.; BRANDAO, A. S.; SARCINELLI-FILHO, M. Modelling and control of a pvtol quadrotor carrying a suspended load. In: **2015 International Conference on Unmanned Aircraft Systems (ICUAS)**. Colorado, USA: IEEE Robotic and Automation Society, 2015. p. 444--450.

POUNDS, P. E. I.; BERSAK, D. R.; DOLLAR, A. M. Stability of small-scale uav helicopters and quadrotors with added payload mass under pid control. **Autonomous Robots**, Springer, v. 33, n. 1, p. 129--42, 2012.

PURI, A. A survey of unmanned aerial vehicles (uav) for traffic surveillance. **Department of computer science and engineering, University of South Florida**, Citeseer, p. 1--29, 2005.

RADKOWSKI, S.; SZULIM, P. Analysis of vibration of rotors in unmanned aircraft. In: **2014 19th International Conference on Methods and Models in Automation and Robotics (MMAR)**. Miedzyzdroje, Poland: IEEE, 2014. p. 748--753.

REINOSO, M. J.; MINCHALA, L. I.; ORTIZ, P.; ASTUDILLO, D. F.; VERDUGO, D. Trajectory tracking of a quadrotor using sliding mode control. **IEEE Latin America Transactions**, v. 14, n. 5, p. 2157--2166, 2016.

ROYALL, P. G.; COURTNEY, P. Medicine delivery by drone - implications for safety and quality. **European Pharmaceutical Review**, p. 1--4, 2019.

ROYALL, P. G.; COURTNEY, P. Medicine delivery by drone-implications for safety and quality. **European Pharmaceutical Review**, v. 24, n. 5, p. 48--51, 2019.

SANCHEZ, M.; LORANO, R.; CASTILLO, P.; GONZALEZ, O.; BELTRAN, C.; PALOMO, G. Nonlinear control strategies for a uav carrying a load with swing attenuation. **Applied Mathematical Modelling**, v. 91, p. 709--722, 2021. ISSN 0307-904X. Available from: https://www.sciencedirect.com/science/article/pii/S0307904X20305473.

SCALEA, J. R.; RESTAINO, S.; SCASSERO, M.; BLANKENSHIP, G.; BARTLETT, S. T.; WERELEY, N. An initial investigation of unmanned aircraft systems (uas) and real-time organ status measurement for transporting human organs. **IEEE Journal of Translational Engineering in Health and Medicine**, v. 6, p. 1--7, 2018.

SCALEA, J. R.; RESTAINO, S.; SCASSERO, M.; BARTLETT, S. T.; WERELEY, N. The final frontier? exploring organ transportation by drone. **American Journal of Transplantation**, v. 19, n. 3, p. 962--964, 2019.

SCHNEIDER, D. Electronic license plates for drones [spectral lines]. **IEEE Spectrum**, v. 54, n. 5, p. 8--8, 2017.

SHEN, X.; FAN, J.; WANG, H. Design and simulation of eight-rotor unmanned aerial vehicle based on hybrid control system. **International Journal of Aerospace Engineering**, Hindawi, v. 2018, 2018.

SHIANG, W. J.; CANNON, D.; GORMAN, J. Optimal force distribution applied to a robotic crane with flexible cables. In: **Proceedings 2000 ICRA. Millennium Conference. IEEE International Conference on Robotics and Automation. Symposia Proceedings**. San Francisco, CA, USA: IEEE, 2000. v. 2, p. 1948--1954 vol.2.

SIGARI, C.; BIBERTHALER, P. Medical drones: Disruptive technology makes the future happen. **Der Unfallchirurg**, Springer, v. 124, n. 12, p. 974--976, 2021.

SLOTINE, J. J.; LI, W. **Applied Nonlinear control**. United States: Pearson, 1991.

SUBUDHI, C. S.; EZHILARASI, D. Modeling and trajectory tracking with cascaded pd controller for quadrotor. **Procedia Computer Science**, v. 133, p. 952--959, 2018. ISSN 1877-0509. International Conference on Robotics and Smart Manufacturing (RoSMa2018). Available from: https://www.sciencedirect.com/science/article/pii/S1877050918310275.

TERENCIANI, J.; GERONEL, R. S.; BUENO, D. D. Practical aspects behind the rotors forces to control a quadcopter. In: **COBEM, 25th International Congress of Mechanical Engineering**. Uberlandia/MG: ABCM, 2019. p. 1--9.

THIELS, C. A.; AHO, J. M.; ZIETLOW, S. P.; JENKINS, D. H. Use of unmanned aerial vehicles for medical product transport. **Air Medical Journal**, v. 34, n. 2, p. 104--108, 2015. ISSN 1067-991X. Available from: https://www.sciencedirect.com/science/article/pii/S1067991X14003332.

TSIAMIS, N.; EFTHYMIOU, L.; TSAGARAKIS, K. P. A. A comparative analysis of the legislation evolution for drone use in oecd countries. **Drones**, v. 3, n. 4, p. 1--15, 2019. ISSN 2504-446X. Available from: https://www.mdpi.com/2504-446X/3/4/75.

UTKIN, V. I. **Sliding Modes in Control and Optimization**. Berlim, Germany: Springer Science & Business Media, 2013.

VALAVANIS, K. P.; VACHTSEVANOS, G. J. **Handbook of Unmanned Aerial Vehicles**. New York, USA: Springer, 2014.

VERMA, M.; LAFARGA, V.; BARON, M.; COLLETTE, C. Active stabilization of unmanned aerial vehicle imaging platform. **Journal of Vibration and Control**, v. 26, n. 19-20, p. 1791--1803, 2020. Available from: https://doi.org/10.1177/1077546320905494.

VOORDE, P. V.; GAUTAMA, S.; MOMONT, A.; IONESCU, C.; FRA. The drone ambulance [a-uas]: golden bullet or just a blank? **Resuscitation**, v. 116, p. 46--48, 2017. ISSN 0300-9572. Available from: https://www.sciencedirect.com/science/article/pii/S0300957217301995.

WANG, B.; MU, L.; ZHANG, Y. Adaptive robust control of quadrotor helicopter towards payload transportation applications. In: **2017 36th Chinese Control Conference (CCC)**. Dalian, China: IEEE, 2017. p. 4774--4779.

WU, Y.; XIE, Y.; LI, S. Parameter adaptive control for a quadrotor with a suspended unknown payload under external disturbance. **IEEE Access**, v. 9, p. 139958--139967, 2021.

YAKUSHIJI, K.; YAKUSHIJI, F.; YOKOCHI, T.; MURATA, M.; NAKAHARA, M.; HIROI, N.; FUJITA, H. Quality control of red blood cell solutions for transfusion transported via drone flight to a remote island. **Drones**, v. 5, n. 3, p. 1--20, 2021. ISSN 2504-446X. Available from: https://www.mdpi.com/2504-446X/5/3/96.

ZHANG, C.; ZHOU, X.; ZHAO, H.; DAI, A.; ZHOU, H. Three-dimensional fuzzy control of mini quadrotor uav trajectory tracking under impact of wind disturbance. In: **2016 International Conference on Advanced Mechatronic Systems (ICAMechS)**. Melbourne, VIC, Australia: IEEE, 2016. p. 372--377.

ZHENG, E. H.; XIONG, J. J.; LUO, J. L. Second order sliding mode control for a quadrotor uav. **ISA Transactions**, v. 53, n. 4, p. 1350--1356, 2014. ISSN 0019-0578. Disturbance Estimation and Mitigation. Available from: https://www.sciencedirect.com/science/article/pii/S0019057814000512.

ZHOU, X.; LIU, R.; ZHANG, J.; ZHANG, X. Stabilization of a quadrotor with uncertain suspended load using sliding mode control. In: AMERICAN SOCIETY OF MECHANICAL ENGINEERS. **International Design Engineering Technical Conferences and Computers and Information in Engineering Conference**. New York, NY, 2016. v. 50152.